Titre: Title:	Three Dimensional Numerical Predicton of Icing Related Power and Energy Losses on a Wind Turbine
Auteur: Author:	Ece Sagol
Date:	2014
Type:	Mémoire ou thèse / Dissertation or Thesis
Référence: Citation:	Sagol, E. (2014). Three Dimensional Numerical Predicton of Icing Related Power and Energy Losses on a Wind Turbine [Thèse de doctorat, École Polytechnique de Montréal]. PolyPublie. https://publications.polymtl.ca/1476/

URL de PolyPublie: PolyPublie URL:	https://publications.polymtl.ca/1476/
Directeurs de recherche: Advisors:	Marcelo Reggio, & Adrian Ilinca
Programme: Program:	Génie mécanique

UNIVERSITÉ DE MONTRÉAL

THREE DIMENSIONAL NUMERICAL PREDICTION OF ICING RELATED POWER AND ENERGY LOSSES ON A WIND TURBINE

ECE SAGOL

DÉPARTEMENT DE GÉNIE MÉCANIQUE

ÉCOLE POLYTECHNIQUE DE MONTRÉAL

THÈSE PRÉSENTÉE EN VUE DE L'OBTENTION

DU DIPLÔME DE PHILOSOPHIAE DOCTOR

(GÉNIE MÉCANIQUE)

AVRIL 2014

UNIVERSITÉ DE MONTRÉAL

ÉCOLE POLYTECHNIQUE DE MONTRÉAL

Cette thèse intitulée :

THREE DIMENSIONAL NUMERICAL PREDICTION OF ICING RELATED POWER AND
ENERGY LOSSES ON A WIND TURBINE

présentée par : SAGOL Ece

en vue de l'obtention du diplôme de : Philosophiæ Doctor

a été dûment accepté par le jury d'examen constitué de :

M. CAMARERO Ricardo, Ph.D., président

M. REGGIO Marcelo, Ph.D., membre et directeur de recherche

M. ILINCA Adrian, Ph.D., membre et codirecteur de recherche

M. TRÉPANIER Jean-Yves, Ph.D., membre

M. MASSON Christian, Ph.D., membre

DEDICATION

To my family

ACKNOWLEDGEMENTS

RÉSUMÉ

Plusieurs régions du Canada sont soumises à des conditions hivernales difficiles qui persistent pendant plusieurs mois. En conséquence, les éoliennes situées dans ces régions sont exposées aux effets du froid, à l'accumulation de glace et à leurs effets négatifs qui se manifestent de la perte de puissance temporaire jusqu'à l'arrêt complet de la machine. Dans certains sites au Canada, la perte de production annuelle d'une turbine éolienne peut atteindre jusqu'à 16% de sa valeur nominale et l'estimation de ces pertes avant la construction d'un parc éolien devient essentielle pour les développeurs et investisseurs.

La revue de la littérature montre que la plupart des logiciels de prévision de givrage ont été développés pour les avions, et sont, en majorité, la propriété d'entreprises et inaccessibles aux chercheurs œuvrant dans d'autres domaines. En plus, le givrage des avions est différent de celui de l'éolienne. Les éoliennes sont exposées à des conditions de givrage pour des périodes beaucoup plus longues que les avions, peut-être pour plusieurs jours dans un climat rude, alors que la durée maximale de l'exposition d'un avion est d'environ 3-4 heures. En outre, les pales d'éoliennes fonctionnent à des vitesses subsoniques, à des nombres de Reynolds inférieurs à ceux des avions, et leurs caractéristiques physiques sont différentes. Quelques logiciels ont été cependant développés pour le givrage des éoliennes. Toutefois, ils sont soit en 2D et ne considèrent pas les caractéristiques 3D du champ d'écoulement, ou se concentrent sur la simulation de chaque rotation d'une manière dépendante du temps, ce qui n'est pas pratique pour le calcul de longues heures de l'accumulation de glace.

Dans ce contexte, notre objectif dans cette thèse est de développer une méthodologie numérique 3D pour prédire la forme de givre et la perte de puissance d'une éolienne en fonction des conditions météorologiques. En plus, nous calculons la production énergétique annuelle d'une turbine typique pour des conditions normales d'exploitation et en tenant compte des évènements givrants. Les calculs sont effectués en utilisant une éolienne pour laquelle des nombreuses données sont disponibles, l'éolienne NREL Phase VI et les conditions météorologiques d'un parc éolien en Suède pour lequel les évènements de givrage sont enregistrés et publiés.

La méthode proposée est basée sur le calcul et la validation de la performance de l'éolienne propre, le calcul de la forme de givre et de la performance de la pale givré, pour des conditions de givrage typiques. La première étape consiste à calculer la performance du NREL Phase VI en

utilisant un outil CFD commercial, ANSYS-FLUIDES. Afin de réduire le coût de calcul, on utilise un modèle de rotation du domaine de référence de la pale avec un calcul des valeurs temporelles moyennes des propriétés de l'écoulement. Une étude de la sensibilité du maillage a permis de déterminer sa taille optimale du maillage afin de respecter les conditions de convergence et de précision. Parmi les modèles de turbulence existants, nous avons sélectionné *SST k-ω* qui a fourni les meilleurs résultats pour les conditions d'écoulement autour de pales givrées, caractérisées par des larges zones de décrochage. En général, les coefficients de pression et le moment de flexion concordent bien avec les données expérimentales, en particulier pour des vitesses avant le décrochage. Bien que le couple prédit s'écarte des données expérimentales, la tendance de variation par rapport à la vitesse du vent est similaire.

Après que la courbe de puissance de la pale propre est calculée, nous déterminons l'efficacité de collection qui caractérise la masse d'eau surfondue qui frappe la pale et qui est directement proportionnelle au taux de givrage d'une surface. Une analyse multiphasique pour les phases d'air et d'eau (approche eulérienne) est utilisée pour calculer le taux d'accumulation des gouttelettes sur la surface de la pale. Les deux approches permettant de caractériser l'écoulement des gouttelettes d'eau, eulérienne et lagrangienne, ont été étudiées avant de décider laquelle était la plus appropriée pour notre étude. La première méthode (eulérienne) est caractérisée par la résolution des équations de mouvement de toute la phase liquide, tandis que la seconde méthode (lagrangienne) est basée sur le calcul de la trajectoire de chaque gouttelette dans l'air. Nous avons finalement choisi le modèle Eulérien pour notre étude, car il peut être adapté pour traiter les maillages vastes et complexes mieux que le modèle Lagrangien. La validation de cette étape est exécutée sur un profil aérodynamique, NACA 0012, comme des données expérimentales en 3D ne sont pas disponibles.

Ensuite, l'accumulation de glace sur l'éolienne est calculée en utilisant des méthodes « Quasi-3D » et « Fully-3D », basées sur des modèles physiques similaires, mais avec une considération différente des aspects tridimensionnels. Pour la méthode Quasi-3D, toutes les étapes mentionnées sont réalisées en 2D et la puissance totale est calculée en utilisant la méthode "Blade Element Momentum ", alors que le « Fully-3D » effectue toutes les étapes dans un domaine 3D. La méthode « Fully-3D » donne des prévisions de la puissance plus précises pour la pale propre. Pour la pale givrée, la validation a été impossible en raison du manque de données expérimentales et de résultats d'autres modélisations. Cependant, les deux méthodes donnent des

résultats différents pour la forme de la glace et pour la performance de la pale givrée. Une analyse critique des résultats montre que, bien que le coût de calcul de la méthode entièrement 3D est beaucoup plus élevé, la prédiction du givrage en 2D peut manquer de précision, la forme de la glace et la perte de puissance sont surestimées en raison de l'absence des effets 3D de l'écoulement de rotation.

En effectuant les calculs CFD sur la pale givrée, la surface rugueuse du givre est lissée jusqu'à un certain niveau pour éviter l'instabilité numérique et pour garder un nombre raisonnable d'éléments de maillage. Cependant, l'effet de la rugosité ne peut être exclu, car il contribue de façon significative à la diminution de la performance. Pour cette raison, la présence de la rugosité de la glace est prise en compte par une modification dans le code CFD. L'effet de la rugosité sur la performance est analysé aussi sur la pale propre.

Enfin, la production annuelle d'énergie de l'éolienne est calculée pour un parc éolien pour lequel les conditions de givrage sont disponibles dans la littérature. Des analyses paramétriques des valeurs du contenu en eau liquide et la taille des gouttelettes montrent comment ces paramètres affectent la forme de glace et les performances des turbines éoliennes. Par ailleurs, les productions énergétiques annuelles pour les configurations propre et givrée sont comparées.

ABSTRACT

Regions of Canada experience harsh winter conditions that may persist for several months. Consequently, wind turbines located in these regions are exposed to ice accretion and its adverse effects, from loss of power to ceasing to function altogether. Since the weather-related annual energy production loss of a turbine may be as high as 16% of the nominal production for Canada, estimating these losses before the construction of a wind farm is essential for investors.

A literature survey shows that most icing prediction methods and codes are developed for aircraft, and, as this information is mostly considered corporate intellectual property, it is not accessible to researchers in other domains. Moreover, aircraft icing is quite different from wind turbine icing. Wind turbines are exposed to icing conditions for much longer periods than aircraft, perhaps for several days in a harsh climate, whereas the maximum length of exposure of an aircraft is about 3-4 hours. In addition, wind turbine blades operate at subsonic speeds, at lower Reynolds numbers than aircraft, and their physical characteristics are different. A few icing codes have been developed for wind turbine icing nevertheless. However, they are either in 2D, which does not consider the 3D characteristics of the flow field, or they focus on simulating each rotation in a time-dependent manner, which is not practical for computing long hours of ice accretion.

Our objective in this thesis is to develop a 3D numerical methodology to predict rime ice shape and the power loss of a wind turbine as a function of wind farm icing conditions. In addition, we compute the Annual Energy Production of a sample turbine under both clean and icing conditions. The sample turbine we have selected is the NREL Phase VI experimental wind turbine installed on a wind farm in Sweden, the icing events at which have been recorded and published.

The proposed method is based on computing and validating the clean performance of the turbine, and then computing the ice shape and iced blade performance, under icing conditions. The first step is to compute the performance of the NREL Phase VI using the commercial ANSYS-FLUENT computational fluid dynamics (CFD) tool. In order to reduce the computational cost, we use a rotating reference frame model which computes the flow properties as time-averaged quantities. A grid sensitivity study has been performed to eliminate the effect of mesh on the

results. Of the existing models for characterizing turbulence, we have selected the two-equation *SST k-ω* model. In general, the computed pressure coefficients and bending moment have shown good agreement with the experimental data, particularly at pre-stall speeds. Although the torque deviates from the experimental data, the trend with respect to the wind speed is similar.

After the clean power curve has been computed, collection efficiency, which is directly proportional to the rate of icing of a surface, is analyzed. A multiphase analysis, for the air and water phases, is necessary to compute the rate of accumulation of the droplets on the blade surfaces. We study two different approaches that are found in the literature – Eulerian and Lagrangian – and determine the most suitable one for our study case. The former applies the governing equations to the liquid phase, while the latter computes the trajectory of each droplet present in the air. We eventually decided on the Eulerian model for our study, as it can be adapted to handle large and complex meshes better than the Lagrangian model. This step is validated on a NACA 0012 airfoil, as experimental data for 3D flows are not available in the literature.

The ice accretion on the sample wind turbine blades is computed using both a Quasi-3D and a Fully-3D method, which have a similar theoretical background, but a different order of modeling. In the former, all the steps are carried out in 2D and the overall power is computed using the Blade Element Momentum method, while the latter performs all the steps in the 3D domain. The Fully-3D method yields more accurate predictions for a clean blade. For icing conditions, a validation is not possible, owing to the lack of experimental data. However, the two methods produce quite different results for the performance of the ice shape and the iced blade. A critical analysis of the results shows that, although the computational cost of the Fully-3D method is much higher, icing analyses in 2D may lack accuracy, because the ice shape and the related power loss are compromised by not considering the 3D features of rotational flow.

While performing the CFD computations on the iced blade, the rough surface of the ice is smoothed to a degree, in order to prevent numerical instability and to keep the mesh size within a reasonable limit. However, roughness effects cannot be excluded altogether, as they contribute significantly to performance reduction. We consider roughness through a modification in the CFD code, and assess its effect on performance for the clean blade.

Finally, the Annual Energy Production of the wind turbine is computed for a selected wind farm, the icing conditions of which are available in the literature. Parametric analyses of Liquid Water Content and the droplet size reveal how the variation of these parameters affects the ice shape and performance of the turbine. We also compared the energy production of clean and iced blade configurations.

TABLE OF CONTENT

LIST OF TABLES

LIST OF FIGURES

LIST OF ABBREVIATIONS

AEP	Annual Energy Production, MWh
B	ice layer thickness, m
C_D	drag coefficient
C_p	pressure coefficient
c_i , c_w	specific heat of ice and water, J/kgK
D_{mean}	mean diameter, μm
d_p	water droplet diameter, m
E_{clean}, E_{iced}	energy produced by clean and iced blade, kWh
e_1	water vapor pressure at altitude 1
f	drag function
$f(V)$	wind Weibull function
$\vec{g}$	gravity, m/s^2
h	water layer thickness, m
k	wind shape parameter
K	interphase exchange coefficient
L_F	latent heat from fusion, J/kg
LWC	liquid water content, g/m^3
M_{ice}	ice mass on blade, kg
MVD	median volume diameter, μm
N	approximate number of droplets in air
p	pressure, kPa
Re	Reynolds number

Re_d	water droplet Reynolds number
t	time, s
T	ice temperature. K
V_{ice}	volume of ice, m^3
$\boldsymbol{V_a}, \boldsymbol{V_w}$	velocity vector of air and water, m/s
V_∞	freestream velocity, m/s
α_q	volume fraction of phase q
β	collection efficiency
ε	the constant ratio of the molecular weight for water vapor and dry air
κ_i, κ_w	thermal conductivity of ice and water, W/mK
$\bar{\bar{\tau}}_p$	shear stress component
θ	water temperature, K
ρ_i, ρ_w	density of ice and water, kg/m^3

LIST OF APPENDICES

INTRODUCTION

Description of the Problem

The demand for more energy grows year after year, to keep pace with the increasing population of the world. Although fossil fuels are still the most widely used and widely available energy resource, they cannot meet all the energy requirements of the people on this planet, nor are they distributed evenly over the planet. As a result, fossil fuel prices frequently become unstable, as a result of production and supply crises, and countries lacking their own oil supply have been seeking alternative energy resources that are both feasible and sustainable. Another challenge is the threat of increased amounts of harmful greenhouse gases in the atmosphere due to the burning of fossil fuels, which adds to the pressure to use renewable energy resources. The Kyoto Protocol, which is aimed at reducing this greenhouse gas accumulation, has been accepted by many countries, and resulted in national and international agreements to limit the use of fossil fuels. Among the renewable energy resources being considered is wind energy, which has garnered attention because of its global availability and because it is cheap.

A number of countries, like Canada, experience long, cold winters, and wind turbines in these countries are exposed to icing, which has several adverse effects, on both the performance and the life expectancy of the turbine. Therefore, predicting energy losses due to icing is a vital issue for investors to consider.

The severity of these adverse effects will vary, depending on the amount of ice accreted. One of the most serious problems is a heavy ice load, which causes significant energy loss, as it can result in the turbine stopping altogether. Even light icing conditions are reported to cause the aerodynamic profile of the turbine blades to change and surface roughness to increase, which increases drag and decreases the lift coefficient. The article referenced in Chapter 3 provides a thorough review not only of the effects of roughness due to light icing, but also the effects of other types of contamination on wind turbine blades. In harsh winter conditions, the annual loss of power generated is reported to be as high as 16% of the nominal production for Canada (Lacroix 2013). Paradoxically, most of the numerical analyses, experiments, and wind farm measurements show that ice accretion on blades may cause a temporary increase in power generation due to delayed stalling. While this may seem to be an advantage, the wind turbine

blades are, in fact, overloaded with ice, which threatens the integrity of both the generator and the structure itself.

Icing also has an adverse effect on the structure, as it causes the blades to fatigue more quickly, with a corresponding decrease in their life expectancy. Furthermore, a non axisymmetric distribution of these loads produces edgewise vibrations, leading to the possibility of resonance (Hansen, et al. 2006). Finally, the accumulated ice on the blade may shed, propelled by rotational force, which poses a danger to residential areas, public roads, power lines, etc. located around the wind turbines.

In broad terms, icing may refer to ice accretion on structures owing to either atmospheric icing, caused by micro-sized supercooled water droplets that exist in liquid form in sub zero temperatures, or any type of precipitation, like rain or snow, accumulating on the blade in the form of ice. In this study, we refer to ice accretion on wind turbine blades caused by atmospheric icing, which typically forms in harsh winter environments and at higher altitudes.

It is important that we provide a classification of ice types before evaluating the effects of icing on wind turbines. A study by Bragg et al. (2005) classifies the ice formations according to their shapes and their influence on performance, as shown in Figure 0-1. They define the roughness type icing as the initial stages of icing, where the ice particles create small perturbations on the airfoil surface. This type of icing is reviewed in Chapter 3, and its effect on the sample wind turbine is analyzed in Chapter 6. Streamwise ice, or rime icing, follows the contours of the airfoil. Horn ice, or glaze ice, is an ice formation with a horn shape at the leading edge, as the name implies. Finally, ridge ice is made up of relatively large chunks of ice that are located separately on the airfoil. This type of icing is associated with supercooled large droplets (SLD).
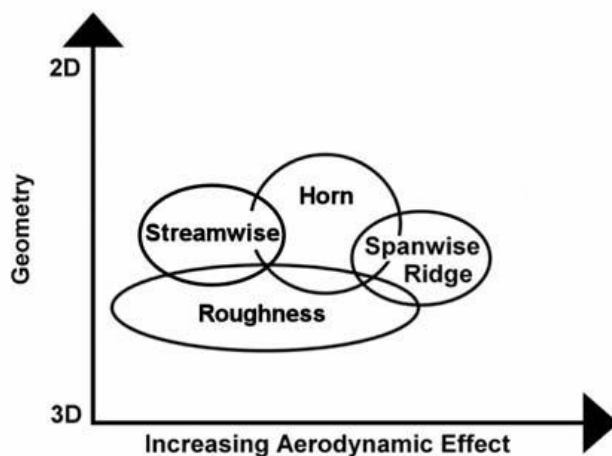
Figure 0-1 Classification of ice types (Bragg, Broeren, & Blumenthal, 2005)

The types of icing that occur most frequently are glaze (horn) and rime (streamwise) icing, and these are illustrated in Figure 0-2.Glaze forms near $0^{o}C$, and a water layer covers the ice layer in this case. For this reason, it is transparent and homogeneous. It has a higher density than rime icing. The horn shape is formed by 'runback' water, which does not freeze at the leading edge, but later on. Glaze ice causes huge performance losses, since the horn-like structure on the upper surface causes flow separation, even at smaller angles of attack. Fortunately, this type of icing is less frequent than rime icing in cold regions.

Rime icing occurs when supercooled water droplets freeze immediately upon contact with a surface. It has a rough, opaque appearance. However, the structure follows the streamlines, and so its effect on aerodynamic flow is less destructive than that of glaze icing.
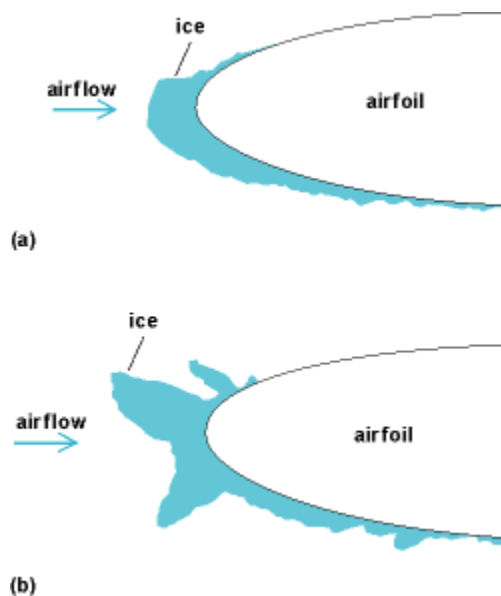
Figure 0-2 (a) rime ice; and (b) glaze ice. (Bragg, Broeren, & Blumenthal, 2005)

During icing events, significant losses in power production are observed in wind farm measurements. The power performance of a 400 kW iced turbine and a clean wind turbine in Italy were compared by Botta et al. (Botta, Cavaliere and Holttinen 1998) –see Figure 0-3.One minute of power measurement shows that the power of the iced turbine is about 30% that of the clean turbine. There are many examples in the literature that demonstrate the overall reduction in both power and energy production of wind turbines. Lacroix (2013) has indicated that the annual energy production losses in the Canadian provinces varies from 3% to 16%. The AEP loss measured in Quebec for the reference year was 7.4%.
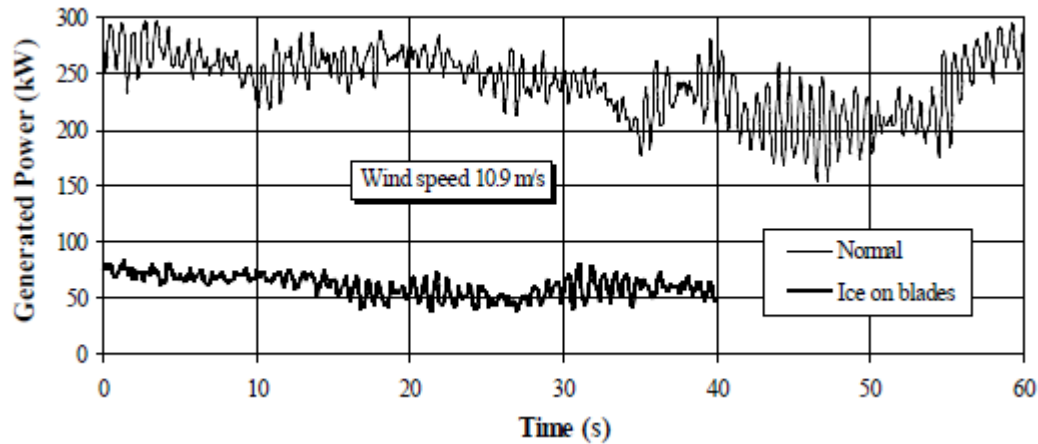
Figure 0-3 In-site power measurement for an iced rotor blade and a clean rotor blade (Botta, Cavaliere, & Holttinten, 1998)

A number of icing codes are available for aircraft and wind turbines. LEWICE, developed by NASA's Glenn Research Center, is an ice growth prediction code for aircraft. LEWICE is made up of four main modules for the computation of flow field, particle trajectory, mass, and energy balance equations, and of the updated ice shape. The flow field is computed using the panel method, which yields accurate results for fixed wing aircraft, but this prediction code has not been applied to wind turbines.

Makkonen et al. (2001) present a 2D icing code, TURBICE, to simulate glaze and rime icing on wind turbines. TURBICE also uses the panel method for flow field prediction. Comparison with experimental data shows that the shape of rime ice is predicted quite well, whereas the shape of glaze ice is not. The authors conclude that non matching ice shape measurements are a result of error in determining whether the ice growth is rime ice or glaze ice.

A comprehensive methodology for the simulation of icing on various machines is presented by Aliaga et al. (2010). FENSAP-ICE-Unsteady has the ability to predict ice shapes on aircraft and jet engines using 3D Unsteady Navier-Stokes equations for the flow field (FENSAP module), and the Eulerian method for the water droplet trajectory analysis. Although FENSAP-ICE-Unsteady is superior in terms of computing unsteady impingement on a surface, it is not cost-effective, since 2100 rotations of the rotor are needed for 1 minute of icing simulation for a helicopter.

There are other codes in the literature; however the methodologies on which they are based are similar. Among these codes is CANICE (Bombardier Aerospace), TAICE (Turkey), CIRAMIL

(Italy), ONERA (France), and ICECREMO and DRA (United Kingdom). All these programs were developed for aerospace applications, i.e. aircraft icing.

To summarize, a survey of the technical literature shows that ice prediction methods are widely available for aircraft icing. However, these are commercial codes, developed specifically for aircraft industry specifications. Moreover, wind turbines are exposed to icing for longer periods than aircraft. The typical maximum icing duration for an aircraft is about 3-4 hours, whereas a wind turbine operating in a harsh winter climate may be exposed to icing for several days. Clearly, a computational method specifically developed for wind turbines is required, if we are to be able to accurately predict icing effects on these machines. A few modeling initiatives have been undertaken for ice accretion on wind turbines. However, these codes – TURBICE, FENSAP-ICE, and CIRAMIL – are either in 2D, which doesn't take in account the 3D characteristics of the flow field, or they are commercial.

Objectives

The main objective of this thesis is to develop a 3D numerical methodology for the computation of the shape of rime ice on turbine blades and the power loss of the machine as a function of wind farm icing conditions. With this information, we can compute the corresponding annual energy loss, which is a critical parameter in wind farm construction. We perform the numerical computations using the current version of ANSYS FLUENT, and develop an in-house code for 3D rime ice prediction on the MATLAB platform.

The issues addressed to develop a 3D numerical energy loss modeling tool for iced wind turbines are as follows:

1- Computation of the flow field, calibration of CFD analysis parameters, like a turbulence model and mesh settings, and validation of the performance of the sample wind turbine blades in 3D.

2- Calculation of collection efficiency using the Eulerian multiphase model, and validation of this parameter for a sample NACA 0012 airfoil, the experimental data for which are available in the literature.

3- Development of an in-house program for predicting the 3D shape of rime ice.

4- Computation of the flow field and performance of an iced wind turbine using the CFD tool.

5- Comparison of a 2D analysis and a 3D analysis with respect to ice shape and the corresponding performance characteristics.

6- Analysis of the wind turbine installed in a sample wind farm and computation of its annual energy loss.

7- Provide a baseline analysis method for 3D ice prediction that can be further developed for glaze icing.

3D numerical computations can predict the shape of the ice that has accumulated on blades, and the related power and energy loss of a wind turbine, as functions of wind farm icing characteristics. Additional computational resources will contribute to better prediction of the effects of icing.

3D numerical modeling has not been used to predict power curves and energy losses as a function of environmental conditions. The proposed method for estimating energy losses and ice shape is essential to the exploitation of wind turbines in cold environments.

Organization of the thesis

Along with the general organization of this thesis, we discuss the consistency of the four submitted-two of them published-papers, on this topic, and their objectives. These four journal articles are each discussed in detail in a separate chapter, and our final results are presented in a chapter following the articles.

Critical review section provides the summary and analyses of the effect of icing on wind turbines and efforts on the numerical modeling of icing. The methodology section provides a step-by-step presentation of the approach we followed to achieve our general objectives. The overall method is divided to five phases, each of which has its own specific objectives. A phase of the method is validated if experimental data are available in the literature.

The first article, "ARTICLE 1: Issues concerning roughness on wind turbine blades," published in Renewable & Sustainable Energy Reviews of Elsevier in 2013, is presented in Chapter 3. In it, the effects on the flow field and on power generation of surface roughness caused by

contamination are reviewed, the aim being to stress that even the early stages of icing must be taken into account in the power loss computations. Although this article is not the first to have been published, we present it first, as it is a literature review.

The second article, " ARTICLE 2: Assessment of Two-Equation Turbulence Models and Validation of the Performance Characteristics of an Experimental Wind Turbine by CFD," was published in ISRN Mechanical Engineering in 2012. This article, which is the subject of Chapter 4, addresses the objectives of computing and validating the power performance of a clean turbine using the CFD method. In it, an appropriate turbulence model is selected by comparing the results obtained with the experimental data using various models.

The third article, "ARTICLE 3: Comparison of the Quasi-3D and Fully 3D methods for modeling wind turbine icing," was submitted to the Journal of Wind Energy of Hindawi in March 2014. This work, Chapter 5, compares two computational approaches to calculating rime ice shape and the corresponding power loss of a wind turbine. In the first method, *Quasi-3D*, the collection efficiency and ice accretion shape are calculated on a number of 2D profiles of the blade, and the power curve is determined using the Blade Element Momentum method. A multiphase analysis is performed using the Eulerian approach, and the aerodynamic coefficients required for the BEM method are derived from single phase CFD simulations on the iced blade sections. In the second method, the Fully-3D method, all the calculations are executed in a 3D domain. The purpose of this comparison is to determine whether or not the additional computer resources required for the simulations in the Fully-3D method are justified by the improvement in the accuracy of the results.

The final paper, "ARTICLE 4: Numerical Evaluation of THE Roughness Effect on Wind Turbine Performance," was submitted to the Journal of Wind Engineering and Industrial Aerodynamics in October 2013. This manuscript, the subject of Chapter 6, covers the application of a roughness model to prove the findings presented in the review article presented in Chapter 3. In this study, turbine performance is computed in the presence of roughness. Various parameters, such as the effect of wind speed, roughness size, and roughness duration, are evaluated. In addition, a simple Annual Energy Loss (AEP) study is performed for a sample wind farm, and various icing duration scenarios are presented to quantify their effect.

In the final results section, the entire methodology is applied to a specific icing case on a wind farm. The experimental data are derived from a study that measures icing duration, air temperature and humidity, and the power loss of the turbine, which is installed on a wind farm in Sweden. The ice accretion is computed from the minimum to the maximum icing duration within a certain time interval. The power loss is compared to the wind farm data for each icing event. The power curves are presented as functions of icing duration and wind speed. The Annual Energy Production is computed for both nominal and icing conditions, and the figures are compared.

Chapter 1   CRITICAL REVIEW

Ice accretion on wind turbine blades is an impediment to efficient operation in a number of ways, such as reduction in power output, risk of ice shedding during operation, and excessive loading of the blades (Dalili, A. & Carriveau, 2009). The magnitude of these problems is proportional to the severity of the ice accretion. For instance, the lightest icing conditions result in a roughened surface, which is sufficient to bring about an early laminar-to-turbulent transition of the boundary layer (Schlichting, 1979) (Busch, 2009) (Turner, Hubbe-Walker & Bayley, 2000) (Kerho & Bragg, 1997) (Bragg, Broeren & Blumenthal, 2005). Moreover, for a fully rough regime, the frictional drag is a function of the roughness, and the pressure distribution over the airfoil is also affected by the boundary layer displacement effect developed by the surface roughness. These phenomena diminish the aerodynamic performance of the blade, i.e. the lift coefficient decreases and the drag coefficient increases (Hochart, Fortin, Perron & Ilinca, 2008) (Khalfallah & Kolub, 2007). Under heavy icing conditions, not only is the energy yield decreased as a consequence of a distorted aerodynamic profile, but mechanical problems, like overloading, unbalancing and vibration, can occur (Illinca, 2011) (Parent & Ilinca, 2011). In cases of severe icing, the turbines usually stop completely. This is why annual energy losses may be as high as 20% of the expected Annual Energy Production (AEP) in regions that experience harsh winter conditions (Botta, Cavaliere & Holttinten, 1998). The effect on the rotor mechanics of excessive ice build-up is also significant. Although it has not been investigated thoroughly, it is assumed that this excessive and persistent ice build-up shortens the life of the blades owing to metal fatigue, and increases the vibration risk owing to its asymmetric distribution. Finally, as ice chunks may be thrown from the blades during rotation, there is a risk to residential areas, public roads, power lines and other installations located near wind turbines that must be addressed.

Ice is formed when supercooled water droplets hit a surface and freeze. The ice formations that occur most frequently on wind turbines are glaze ice and rime ice. Glaze ice has a horn-like shape and consists of a thick ice layer covered by a thinner, water layer. This characteristic shape originates from the runback water that does not freeze on impact, but does so later on, as it moves towards the trailing edge of a blade. Rime ice, or streamwise ice, by contrast, consists of ice layers that have frozen on impact, where the trajectory of the water droplet meets the surface of a blade. Rime ice has a less negative effect on performance, whereas glaze ice, because of its

shape, has a more pronounced negative effect. In this study, only rime ice accretion on a wind turbine blade is considered.

In an attempt to predict the risks associated with ice accretion and to mitigate them, numerical algorithms can be used to simulate energy losses and provide the necessary data for vibration and aeroelastic analyses. In the literature, the power output of a wind turbine is computed using various numerical tools, such as Blade Element Momentum, Vortex Lattice, and Computational Fluid Dynamics (CFD) solvers. The most popular of these is the Blade Element Momentum (BEM) method, which determines the blade power by integrating the forces on 2D blade sections for which the aerodynamic characteristics are known. This method is extensively used in the literature, because of its reasonable accuracy, low computational cost, and easy modeling characteristics (Sorensen, N. N., Michelsen, J. A. & Schreck, S., 2002) (Johansen & Sorensen, 2004) (Hansen, Sorensen, Voutsinas, Sorensen & Madsen, 2006). Although the BEM method provides a good base for the initial design, more sophisticated models are needed to improve accuracy and to capture flow field information. The 3D CFD solver is more accurate and is extensively used, increasingly so as computational costs are steadily diminishing. (Karlsen 2009) CFD solvers have been used in numerous studies on wind turbine blades to address various issues involving performance (power curve), aerodynamics, fluid-structure interaction, acoustics and icing analysis, for example (Sagol, Reggio & Ilinca, 2012) (Ramdenee, Minea & Ilinca, 2011). A comparison of these methods on various applications has shown that they all perform well for pre-stall regimes. In spite of a certain level of error, these solvers predict power yield more accurately for stall and post-stall regimes than the others. (Duque, Johnson, van Dam, Cortes & Yee, 2000) (Laursen, Enevoldsen & Hijort, 2007) In fact, all these studies conclude that CFD provides realistic results, even though it requires more computational resources, and is much cheaper than conducting full-scale or scaled wind turbine experiments.

In the following sections, studies related to icing on wind turbines and numerical ice accretion simulations are explained step-by-step in line with the proposed methodology.

1.1 CFD Analysis of a Wind Turbine Rotor

The first step in the simulation of ice accretion on wind turbine blades is to accurately predict the flow field and the performance of the rotor. Although 2D or quasi-3D methods, like Blade

Element Momentum Analysis, may predict performance up to a certain level, 3D analysis is required to capture all the turbulence features, which are inherently 3D. As computational cost decreases, thanks to technological development, CFD use for wind turbine design and analysis is becoming more widespread and is leading to a better understanding of the aerodynamic phenomena on the rotor flow field.

Studies on wind turbine aerodynamics in the literature focus on various topics, like performance analysis, fluid-structure interaction, acoustics and icing. Investigation into performance analysis is primarily aimed at estimating the aerodynamic loads, or the effect of various parameters on these loads. Duque et al. (2000) investigated the capability of a number of methods to predict wind turbine power and aerodynamic loads. Results showed that all the methods, namely, Blade Element Momentum (BEM), Vortex Lattice and Reynolds Averaged Navier Stokes (RANS) perform well for pre-stall regimes. Although it is not perfect, the RANS code OVERFLOW gave better predictions of the power production for stall and post-stall regime modeling compared to other methods. Another study based on CFD analysis (Sorensen, et al. 2002) showed that the predicted performances and loads of wind turbines are very accurate, except in the stall region. A commercial wind turbine company, Siemens, analyzed their own large scale wind turbine using a commercial CFD code, ANSYS-CFX, with transition and fully turbulent models (Laursen, Enevoldsen and Hijort 2007). The use of transition models improves drag prediction, but overestimates lift compared to fully turbulent models. Benjanirat et al. (2003) used CFD with various turbulence models: Baldwin-Lomax, Spalart-Allmaras and k-ε, with and without wall corrections, on an experimental wind turbine. The k-ε model with wall correction yielded the best results compared with experimental data. A more recent study conducted by Uzol et al. (2006) using a generic CFD code, PUMA2, showed that time accurate inviscid results are also compatible with the experimental data.

Predicting the effects of tower, nacelle and anemometer on the rotor flow field, have also been investigated in several works. Smaili et al. (2004) and Zahle et al. (2010) both concluded that CFD is an effective tool for evaluating the influence of the nacelle, even for different positions and alignments of the wind turbine. All these studies show that it is cheaper to use CFD than to conduct full scale or scaled wind turbine experimental analysis, even though CFD requires more resources for unsteady problems, and provides sufficiently accurate results. By improving its ability to simulate widely separated flows through better turbulence modeling near the wall and

in the flow field, CFD tools are becoming more and more accurate for the aerodynamic and aeroelasticity analysis of wind turbine blades.

1.2 Wind Tunnel & On-Site Experiments on Icing

Physical investigation of the icing on wind turbines is required to understand the icing mechanism, so that the energy losses can be estimated and effective icing mitigation mechanisms developed. Up to now, both wind tunnel and on-site experiments have provided data to develop mathematical models and empirical relations to estimate ice shape and its effect on wind turbine performance. As the wind tunnel experiments are controlled in terms of atmospheric conditions and the effects of several parameters are investigated in various flow conditions, these experiments constitute a valuable contribution to our knowledge of the physics of icing. Moreover, a wind tunnel makes it possible to measure more parameters, like ice thickness, heat transfer, temperature, loads on the blades, etc. In contrast, on-site experiments are more difficult to perform, but they do have advantages. Because the atmospheric conditions in on-site experiments are not idealized as they are in a wind tunnel, they yield more realistic results. Furthermore, full scale 3D rotating experiments may contribute to our understanding of the effect of rotation on icing.

In the study by Jasinski et al. (1997), the rime ice effects on the S809 profile of a 450 kW rotor were estimated. Initially, a clean profile was tested in the UIUC wind tunnel for several angles of attack, and the resultant lift and drag coefficients were compared to the results of other wind tunnel experiments with the S809 profile to validate the results. Ice accretion on this profile was estimated using NASA's LEWICE code for typical droplet diameter and icing duration at -10°C and an LWC of 0.1 g/m^{3}. Once the ice shapes had been obtained, they were manufactured for wind tunnel testing. In addition, aluminum oxide grit was applied to leading edge of the clean model to simulate light icing conditions. Results of comparing the lift, drag and pitching moment coefficients of clean, lightly iced and iced profiles are presented in Figure 1-1. LEGR stands for Leading Edge Grit Roughness, which represents light icing conditions. R2 and R4 represent droplet diameters of 15 μm and 30 μm respectively.
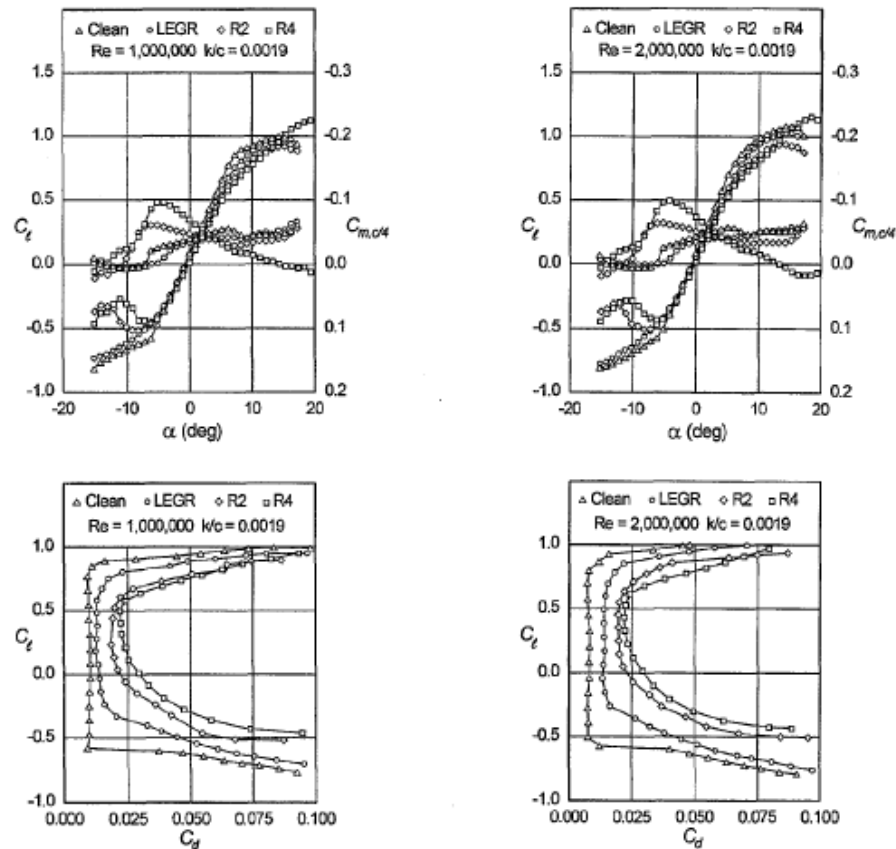
Figure 1-1 S809 performance under clean and iced conditions (Jasinski, et al. 1997)

As seen from the results, the maximum lift coefficient increases for heavy icing conditions, R4; however, at pre-stall angles of attack, the lift coefficient is lower than that for a clean profile. Moreover, the pitching moment coefficient increases as the icing conditions become more extreme. This behavior is related to the large suction peak created at the leading edge, as a result of extreme icing.

In a study by Hochart et al. (2008), different scaled sections of the 1.8 MW Vestas V80 wind turbine were tested in a stationary, multiphase flow wind tunnel. The wind tunnel tests took place at the Anti-Icing Materials International Laboratory (AMIL) at the University of Quebec in Chicoutimi (UQAC). The NACA 63415 airfoil was used for the airfoil of the blade, as the nature of the original airfoil was unknown. Three different radial positions of the V80 rotor were tested at 12, 23.5 and 35 m of a 40 m blade. The relative velocity and angle of attack of each section were calculated for application in the wind tunnel. The icing conditions measured in Murdochville, where the Vestas V80 turbine is located, were applied in the refrigerated wind

tunnel. Two different in-cloud icing conditions were simulated, as follows: -1.4°C with an LWC of 0.218 g/m^3 and a wind speed of 8.8 m/s for 6 hours; and -5.7°C with an LWC of 0.242 g/m^3 and a wind speed of 4.2 m/s for 4.4 hours.

As seen in Figure 1-2, during the first icing event with glaze ice formation (at -1.4°C), drag increases and lift decreases due to icing. This change seems more dramatic towards the tip of the blade, where the amount of ice increases due to higher rotational speed. During the second icing event (at -5.7°C), where rime ice occurs, a less dramatic increase in drag and a reduction in lift are observed, as the weight of the rime ice is less than that of the glaze ice. The decrease in lift is found to be around 40% at the tip of the blade for both types of icing. The drag increases by about 365% and 250% at the tip during glaze and rime icing events respectively.
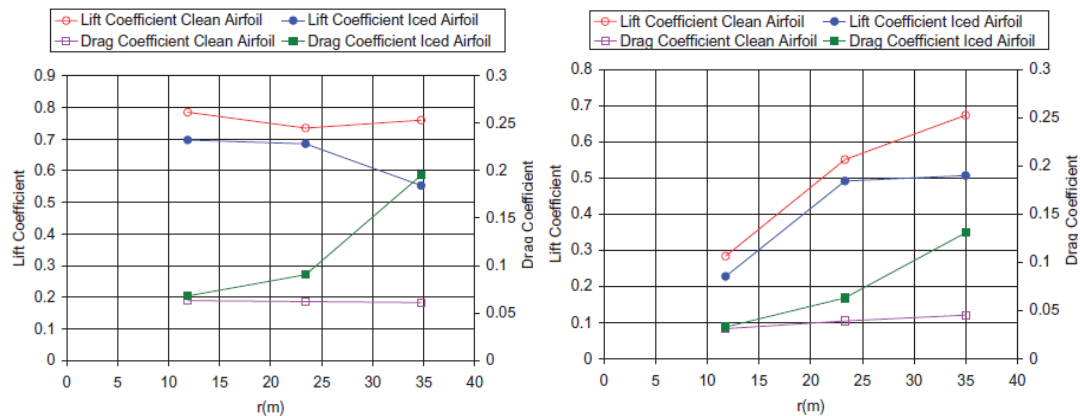
Figure 1-2 Lift and drag coefficient change with glaze and rime icing respectively. Hochart et al. (2008)

1.3 Numerical Investigation of Icing

1.3.1 Collection Efficiency Analysis

A crucial parameter for simulating icing is collection efficiency, which is the rate of accumulation of supercooled droplets on the surface. It is called *catch efficiency* or *collision efficiency* in many studies. A significant number of studies have been carried out on this subject, as the weight of the ice accumulating on a surface is directly related to this parameter. Multiphase analysis of the ice, which is composed of air and water droplets, is needed in order to compute collection efficiency. In the literature, two type of multiphase analysis are performed:

Lagrangian and Eulerian. In Lagrangian analysis, the trajectory of the each water particle present in the airflow is calculated, whereas in Eulerian analysis, the water phase is considered as a continuum, like the air phase.

As the size of the water droplets varies within a range, either all the droplet sizes must be represented, or they must be approximated in a single-sized droplet. Since the second alternative is more practical and more cost-effective, it is the preferred option in many studies. A comparative study by Finstad et al. (1988) showed that the Median Volume Diameter (MVD) approach represents the flow better than the other approaches, namely, Mean Volume Diameter and Mean Diameter. Figure 1-3 shows the collision efficiency for single-size approximation methods and spectral weighted analysis. As we can see, the MVD approach and spectral weighted analysis, in which all the droplet sizes are represented, are well matched.
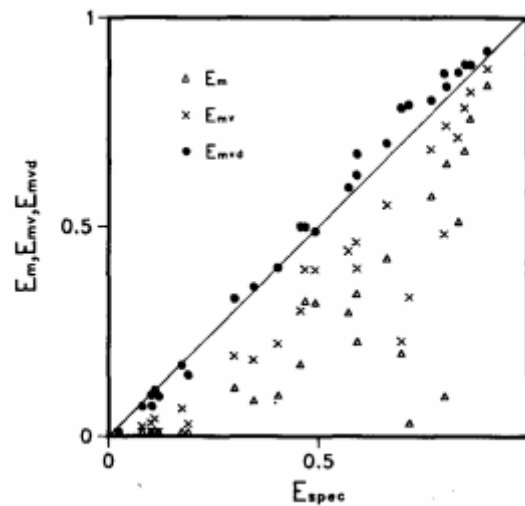
Figure 1-3 Comparison of collision efficiencies for single-size approximation methods and spectral weighted analysis. (Finstad, Lozowski and Makkonen 1988)

The study of Silveria et al. (2003) presents the collection efficiency calculated on various bodies with Lagrangian and Eulerian methods. The authors made a few assumptions for both methods: initially, the water droplets are rigid spheres, which means that the constant drag factor can be used without considering variations in the shape of the droplets; the droplets do not affect airflow, since the water concentration is negligible; finally, gravity is ignored, since the droplets are small. For the Eulerian case, full multiphase simulation was performed using the commercial tool CFX 5.5. In this model, the governing equations for mass, momentum and energy are solved

for both air and water. A phase volume fraction equation is also solved. For the turbulence treatment, the $k - \varepsilon$ model is applied to the main phase, and the zero-equation model is applied to the dispersed phase for improved convergence and numerical stability.

A comparison of multiphase analysis with experimental data for the NACA 0012 airfoil is shown in Figure 1-4.
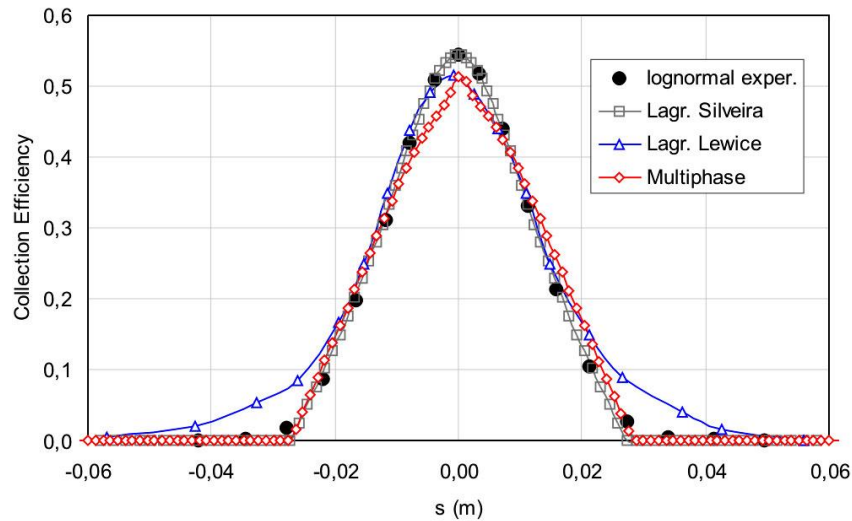
Figure 1-4 Collection efficiency comparison for the NACA 0012 (Silveria, et al. 2003)

The Lagrangian approach gives better results for 2D cases (Silveria et al. 2008). However, for 3D and complex geometries, the use of the Eulerian approach is more appropriate, as it is difficult to make a prediction for the location to inject particles that would hit to wall domains for the Lagrangian method. Moreover, trajectory calculation for each droplet is not cost-effective for a 3D domain.

1.3.2 Ice Shape Computation

Once the accretion rate has been calculated, the ice shape can be determined from a thermodynamic analysis. The Messinger model (Myers 2001), which appears in many icing codes, such as LEWICE and DRA, consists of an energy balance based on equating the heat lost to the air from ice and water accretion and the production of latent heat due to ice growth. The heat loss mechanism includes convective heat transfer at the water surface, evaporative heat loss

and cooling by incoming droplets. In contrast, the gain mechanism includes the kinetic energy of incoming droplets, the release of latent heat and aerodynamic heating.

However, while Messinger's model is the solution for 1D energy balance equations for an insulated and unheated surface exposed to icing, it has some limitations. The transitional behavior cannot be captured, since the temperature is set in an equilibrium state. Moreover, no conduction between the ice and water layers and the surface of the substrate is modeled. This assumption may cause the model to predict less ice accretion on that surface.

A more developed version of Messinger's model has been proposed by Myers (2001), which is known as the Extended Messinger method. The system consists of four equations: heat transfer equations for ice and water, a mass balance equation and a phase change equation, known as the Stefan equation. For this model, ice is assumed to have a perfect thermal contact with the surface, so that the ice temperature at the surface is equal to the surface temperature. Moreover, temperature is continuous at the phase change boundary, and is equal to the freezing temperature. Rime ice thickness is calculated by setting the water thickness to zero, so that only the mass balance equation is solved to calculate ice thickness and temperature. In contrast, the glaze ice is a fraction of the water mass flux on the surface transformed into ice. Another fraction remains as a water layer.

An overview of the ice shape prediction codes and some applications are given below.

<u>LEWICE 3.0</u>

LEWICE (Wright 2005), developed by NASA's Glenn Research Center, is an ice growth prediction code for aircraft. It is updated periodically, in response to advances made in the theoretical background of icing physics. LEWICE is made up of four main modules for the computation of flow field: particle trajectory, mass and energy balance equations, and updated ice shape. The mass and energy balance equations are based on the Messinger model, which accounts for the convection, latent heat transfer, aerodynamic heating and enthalpy change of the water. Heat transfer coefficients are calculated via the Integral Boundary Layer method. For the ice shape calculation, a multilayer approach is used, which enables computation of the step-by-step growth of ice throughout total ice exposure interval.

The latest version of the model, LEWICE 3.0 [24], is capable of 3D icing simulation using either the Navier-Stokes equations or potential flow equations with various droplet mechanisms, like splashing and SLDs.

TURBICE

Makkonen et al. (2001) presented an icing code, TURBICE, to simulate glaze and rime icing on wind turbines. TURBICE uses a panel method for flow field prediction, in which the number of panels is optimized considering the accuracy of the computed local collision efficiency distribution. Potential flow and droplet trajectory analysis are repeated for each layer. Local collision efficiency is a ratio of the space between the droplets away from blade to the space between the droplets near the blade. For multiple size droplets, the Median Volume Diameter approach, which is the best single size parameter approximation method, was used. Ice density is calculated using an empirical correlation called the Macklin parameter, which depends on MVD, free stream wind speed and surface temperature. The heat transfer model is based on mass and energy balance equations. The freezing fraction and surface temperature are calculated by solving these equations at each finite element section on the blade surface. When the freezing fraction is between 0 and 1, the wet growth, runback water is taken into account.

Ice accretion on a NACA 64618, representing a 5 MW pitch controlled blade, has been simulated numerically to investigate the effect of temperature and droplet size on ice accretion by Homola et al. (2010). The commercial CFD code, ANSYS FLUENT, is used to simulate the iced blade, owing to its ability to model complex flows. A structured grid is used with a boundary layer resolution that ensures that y^+ is less than 10. The k-ε turbulence model is used with a log-law function to resolve the thin boundary layer. The authors numerically tested various icing conditions at -2.5^{o}C, -5°C and -7.5^{o}C, and with an MVD of 12, 17 and 30 μm. Results are shown for 17 μm for the investigation of effect of temperature on icing. At -2.5^{o}C, the ice shape shows a horn-like structure, whereas at -5°C and -7.5^{o}C, the ice shape follows the contours of the airfoil, as shown in Figure 1-5. This is because the first shape consists of glaze icing and the others consist of rime icing, as explained above.
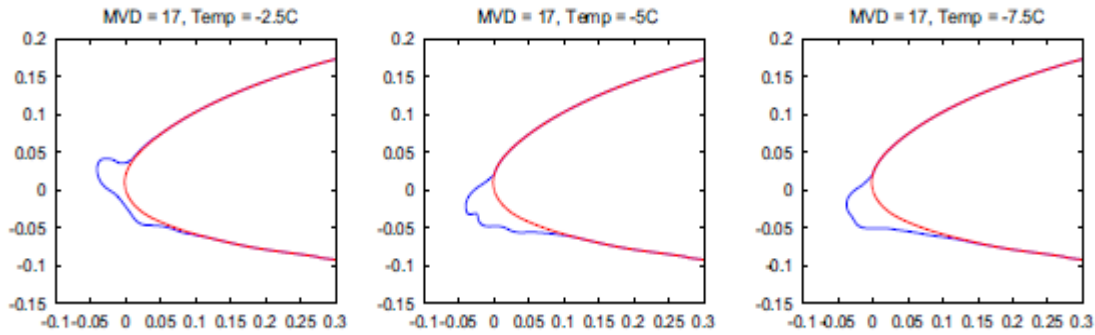
Figure 1-5 Effect of temperature on ice shape calculation (Homola, et al. 2010)

CFD analysis of these profiles shows that, compared to a clean blade, the flow over all the iced blades separates at lower angles of attack. However, the separation is the most dramatic for the glaze iced blade, owing to its horn-like shape. Also, comparison of the aerodynamic coefficients shows that the lift coefficient decreases and the drag coefficient increases as the horn characteristics become more pronounced. The effect of droplet size was tested at -2.5^{o}C. The resulting ice shapes are shown in Figure 1-6. As we can see, the icing area grows with increasing droplet size. This is because the larger droplets have more inertia and are less affected by air drag. The horn structure, which is a characteristic of glaze icing, is not observed for the smallest droplet size of MVD 12 μm. The results of the CFD analysis on iced blades show that, as the MDV increases, the size of the recirculation and separation zone also increases. Moreover, the lift coefficient decreases and the drag coefficient increases with increasing droplet size.
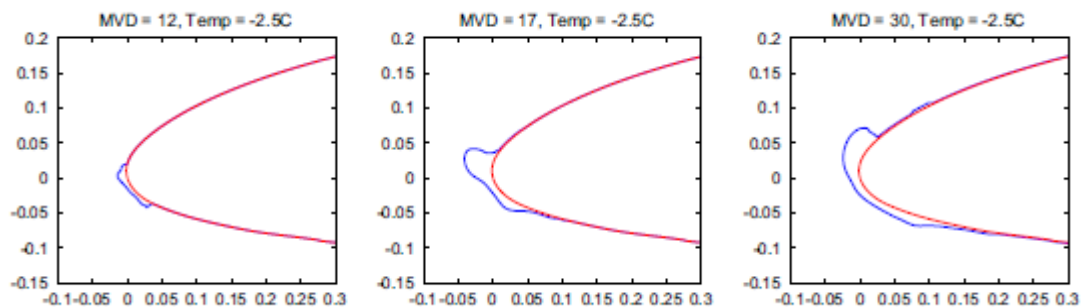
Figure 1-6 Effect of droplet size on ice shape computation (Homola, et al. 2010)

<u>FENSAP-ICE-Unsteady</u>

A methodology for the simulation of icing on various machines is presented by Aliaga et al. (2010). FENSAP-ICE-Unsteady has the ability to predict ice shape on Aircraft, Rotorcraft and jet engines using the 3D Unsteady Navier-Stokes equations for flow field analysis (FENSAP module) and the Eulerian method for water droplet trajectory analysis (DROP 3D module). Although FENSAP-ICE-Unsteady is very profitable in terms of computing unsteady impingement on a surface, it is not cost-effective, since 2,100 rotor rotations are needed for 1 minute of icing simulation of a helicopter blade.

<u>OTHER CODES</u>

Although there are a variety of codes in the literature, the methodology on which they are based is similar. The most popular codes are Bombardier's CANICE, Italy's CIRAMIL, France's ONERA, and the UK's ICECREMO and DRA.

1.4 Iced Airfoil & Blade Aerodynamics

Lee et al. (2000) presented a review on the effects of several parameters on iced airfoil aerodynamic characteristics, such as the lift, drag and pitching moment coefficients. Results are derived from a series of wind tunnel analyses investigating the effects of the ice shape, its size and location on the airfoil, the flight Reynolds number and the airfoil geometry.

As stated above, as the ice thickness increases, the performance of the airfoil decreases as a consequence of the reduction in lift and the increase in drag. However, the leading edge of the airfoil is an exception, as its performance does not deteriorate beyond a critical ice height. Moreover, experiments on ice shape show that, as the ice shape becomes blunter, that is, free of sharp edges, the maximum lift coefficient decreases less. The presence of roughness elements of different heights and of glaze ice have also been studied and it has been shown that the performance of an iced airfoil becomes insensitive to increases in Reynolds number beyond a certain value of that number.

A study by Bragg et al. (2005) classifies ice formations according to their shape and evaluates their influence on airfoil aerodynamics. The roughness type of the ice formation is defined in that work at the initial stages of icing, where the icing particles create small perturbations on the airfoil surface. Streamwise ice follows the contour of the airfoil, which is typical for rime icing. Horn-type ice has a horn shape at the leading edge, as its name implies. Finally, ridge-type ice refers to the relatively large pieces of ice that are located separately on the airfoil. The latter type of icing is associated with SLDs. Experiments show that the roughness type of ice formation causes early transition of the flow at low Reynolds numbers. As the Reynolds number increases further, the transition area over the airfoil grows relative to that of a clean airfoil. Moreover, the increase in the area covered by the roughness ice results in a larger transition area on the airfoil.

For horn-type ice, separation is observed just downstream of the horn. As the angle of attack increases, the separation area increases further, as seen in Figure 1-7. An increase in the bubble area causes the drag coefficient to grow, which ultimately results in a stall at a critical angle of attack.
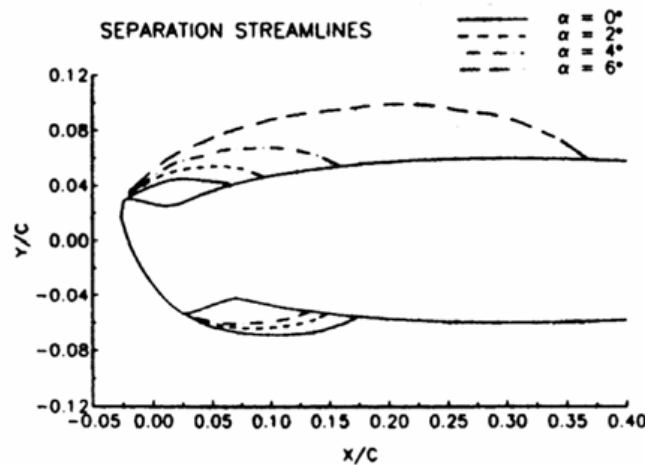
Figure 1-7 Flow separation over horn ice for the NACA 0012. (Bragg, Broeren and Blumenthal 2005)

Comparison of horn-iced airfoils with a clean airfoil show that iced airfoils stall at smaller angles of attack, as seen in Figure 1-8. Moreover, iced airfoils with a different horn tip radius show almost the same lift coefficient curves, which means that the horn tip radius has no effect on the lift coefficient.
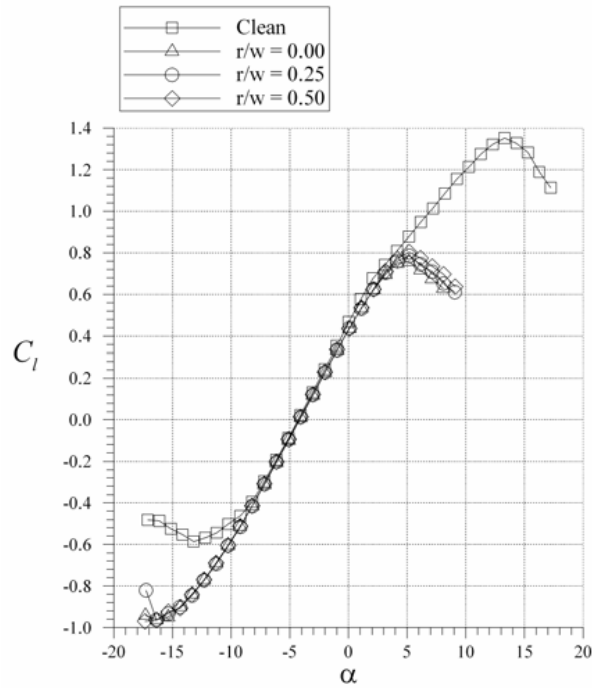
Figure 1-8 Lift Coefficient for clean and horn-iced airfoils (Bragg, Broeren and Blumenthal 2005).

Unlike horn-type icing, streamwise icing reduces the lift coefficient more gently, as seen inFigure 1-9. The effects of streamwise ice become clear at higher angles of attack, and it lowers the lift coefficient much less than horn ice.
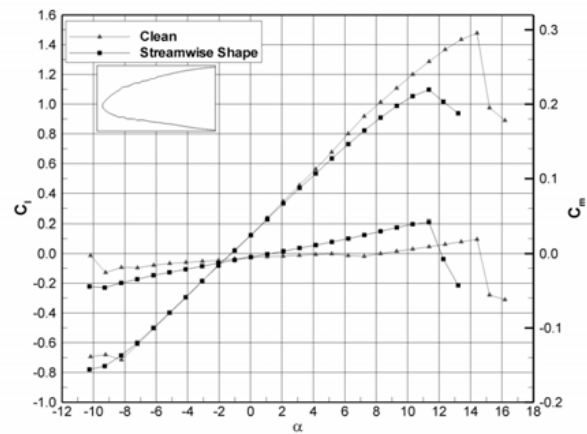
Figure 1-9 Lift and pitching moment coefficients for clean and streamwise iced airfoils (Bragg, Broeren and Blumenthal 2005)

Chapter 2   **METHODOLOGY**

This section briefly describes the approach we take to address the research questions. The methodology is divided into five phases: clean rotor analysis, collection efficiency analysis, ice accretion computation, iced rotor analysis, and power and energy loss modeling. Each of these phases is explained below.

2.1 **Phase I – Clean Rotor Analysis**

The objective in this phase is to perform numerical computations to obtain the power output of a wind turbine as a function wind speed, as well as to validate the numerical models. The power output of the clean machine is required, in order to compute the nominal energy production of the clean rotor, and the flow field obtained from the clean rotor analyses is required as an initial condition for the multiphase analysis performed in the next step. In this phase, the CFD results are validated with the available experimental data. We provide the details of this phase, and present the results in Chapter 4.

The sample wind turbine that we selected for our analyses is the NREL Phase VI experimental wind turbine. Extensive experimental data are available for this turbine, which is the preferred choice researchers, thanks to the reliability of the institution. The features of the wind turbine and the experimental set-up are provided in the paper.

2.2 **Phase II – Collection Efficiency Analysis**

A critical parameter for an icing simulation is collection efficiency, which is the ability of the blade surface to catch the supercooled water droplets. Many studies have been conducted on collection efficiency, as the rate of ice accumulation on the surface is directly proportional to this parameter. In a CFD simulation, it is assessed by analyzing a multiphase flow, which is composed of air and water droplets.

To perform a multiphase flow analysis using CFD, the Liquid Water Content (LWC) of the air and the size of the droplets in the water phase are required as inputs. A complex measurement

system, called a Rotating Multi-Cylinder (Drage and Hauge 2008), can measure these parameters based on ice accreted on a rotating cylinder with the known variations of air temperature, pressure, and wind speed. However, in the absence of this measurement system, which is the case most of the time, LWC and droplet size can be computed using some empirical correlations based on air temperature, pressure, and humidity.

The size of the water droplet is very important in a multiphase flow analysis, as it varies over a range of sizes, which must all be either simulated or approximated to a single size. Since approximation is the more practical and cost-effective option, it has been selected in many studies. The comparative study of Finstad et al. (1988) shows that the Median Volume Diameter (MVD) approach represents the droplet size better than the other approaches. MVD is computed using a mean diameter D_{mean}, as shown in Equation 2-1.

$$MVD = 1.49 D_{mean} + 0.56 \ [\mu m]$$

2-1

where the mean diameter is calculated as follows:

$$D_{mean} = \left(\frac{6}{\pi} \frac{LWC}{\rho_w N} \right)^{1/3} \ [\mu m]$$

2-2

N is the approximate number of droplets present in the air, and ρ_w is the liquid water density. The LWC can be computed, as in Equation 2-3, as a function of the air and water vapor pressure at two different altitudes: a lower altitude with known unsaturated conditions, and a higher altitude with unknown LWC (Drage and Hauge 2008).

$$LWC = \varepsilon \rho_{d2} \left(\frac{e_1}{p_1} - \frac{e_2}{p_2} \right) \ [{}^g/_{m^3}]$$

2-3

Here, ε is the constant ratio of the molecular weight for water vapor and dry air; ρ_{d2} is the density of the dry air at altitude 2; e_1 and e_2 are water vapor pressures; and p_1 and p_2 are air

pressures at altitudes 1 and 2 respectively. The saturation water vapor pressure, e_2, is a function of temperature (T) and computed using Equation 2-4.

$$e_2 = 6.112 \, exp\left(\frac{17.67 \, T}{T+243.5}\right) [mb]$$

2-4

The LWC is defined for icing simulations, and the volume fraction (VOF) of the water phase is provided for numerical simulations. A dimensionless VOF parameter for the water, based on the LWC is computed as follows:

$$VOF_{water} = \frac{LWC \, (g/m^3)}{\rho_{water} \, (g/m^3)}$$

2-5

The sum of the volume fraction of the air phase and the volume fraction of the water phase in a cell will be 1.

In the literature, two types of multiphase flow analysis methods are available: Lagrangian and Eulerian. The former calculates the trajectory of the each water particle present in the airflow, while the latter assumes the water phase as a continuum, like the air phase. The details of these two methods are reviewed in Chapter 5.

Comparisons with experimental data (Silveria, et al. 2003) (Wirogo and Srirambhatla 2002) (Bourgault, et al. 1999) show that the Lagrangian model yields accurate solutions for 2D flows and simple structures, whereas the Eulerian model performs better for 3D and complex problems. Moreover, as the Lagrangian model computes the trajectory of every particle in a flow, the computational time increases drastically for 3D problems, which drives up the cost substantially. For these reasons, we chose the Eulerian model for our analyses here, and we made the following assumptions to facilitate the analysis:

- The droplets are spherical without any deformation or breakage (which we can assume since the droplets are small);
- The droplets are not subject to collision, splashing, or break-up;
- There is no heat or mass exchange between the air and the droplets;
- The turbulence effect on the droplets can be neglected;
- The lift force on the droplets is not simulated, since the Faxen forces are negligible for the droplet-to-chord ratio in the study.

- The only force acting on the droplets is drag, since buoyancy and gravity are neglected.

The phase modeling equations in the Eulerian model for two phases, p and q, which are mass and momentum conservation equations, are as follows:

$$\frac{\partial \alpha_q \rho_q}{\partial t} + \nabla.\left(\alpha_q \rho_q V_q\right) = 0$$

2-6

$$\frac{\partial (\alpha_q \rho_q V_q)}{\partial t} + \nabla.\left(\alpha_q \rho_q V_q V_q\right) = -\alpha_q \nabla p + \nabla \bar{\bar{\tau}}_q + K\left(V_p - V_q\right)$$

2-7

The subscripts p and q represent two different phases in a flow. α_p and α_q denote the volume fraction; V_p and V_q represent the velocity vectors; and $\bar{\bar{\tau}}_p$ and $\bar{\bar{\tau}}_q$ are the shear stress components for the p and q phases respectively. In our study, p and q may denote either the air or the water phase. The interphase exchange coefficient K, which represents the aerodynamic drag on the water particles, is defined in Equation 2-8. When equations are solved for the air phase, the effect of the water particles on the air is neglected, owing to their very small concentration in the water phase.

$$K = \alpha_a \alpha_w f \frac{18\mu_a}{d_w^2}$$

2-8

This exchange coefficient is only written for water phase. μ_a denotes the viscosity of the air, and d_w denotes the water particle diameter. Drag is modeled using the Schiller-Naumann model, which computes the drag coefficient on a sphere with a defined diameter. Although this drag model is used for solid particles, it is also applicable to micron-sized liquid particles, assuming that they retain their spherical shape. The drag function f is defined using the Schiller-Neumann coefficient, as in Equation 2-9.

$$f = \frac{C_D Re_d}{24}$$

2-9

where;

$$c_d = \frac{24}{Re_d}(1 + 0.15Re_d^{0.687}) \text{ for } Re_d \leq 1000$$

$$c_d = 0.4 \text{ for } Re_d > 1000$$

The relative Reynolds number, Re_d, is defined as in Equation 2-10;

$$Re_d = \frac{|\boldsymbol{V_w} - \boldsymbol{V_a}|d_p}{\nu_a} \qquad \text{2-10}$$

Here, V_w is the water velocity and V_a is the air velocity in a cell. As the particles are not tracked (the water fraction in each cell is computed instead), the collection efficiency, β, is computed using the volume fraction of the water on the surface, as shown in Equation 2-11:

$$\beta = \frac{\alpha(\boldsymbol{V_w} \cdot \boldsymbol{n})}{V_\infty} \qquad \text{2-11}$$

where $\boldsymbol{n}$ is the unit normal vector of the surface element; α is volume fraction of the water on the surface; and V_∞ is the free stream speed.

The following parameters are exported from ANSYS FLUENT to in-house code to compute the corresponding ice shape:

- o X,Y,Z coordinates of the cell center
- o X,Y,Z coordinates of nodes
- o Unit normal vector components
- o Cell area
- o Cell connectivity
- o Local volume fraction

o   Local water velocity components

Validation of the collection efficiency computation is presented for a 2D airfoil, as there are no experimental data available for a 3D analysis in the open literature. In a validation case on the NACA 0012 airfoil, a 0.9144 m chord is used (Silveria et al. 2003). The following conditions are given: an inflow speed of 44.7 m/s, a liquid water content (LWC) of 0.78 g/m^3 and a median volume diameter of 20 μm.

ANSYS FLUENT is used to model a multiphase flow consisting of air and water droplets, and the Eulerian methodology is used for the analyses. The *k–ω SST* model is used for the main phase of the turbulence modeling; however, no turbulence model is used for the dispersed phase for better stability of the simulations. Comparisons of the numerical results with experimental data (Silveria et al. 2003) are shown in Figure 2-1.
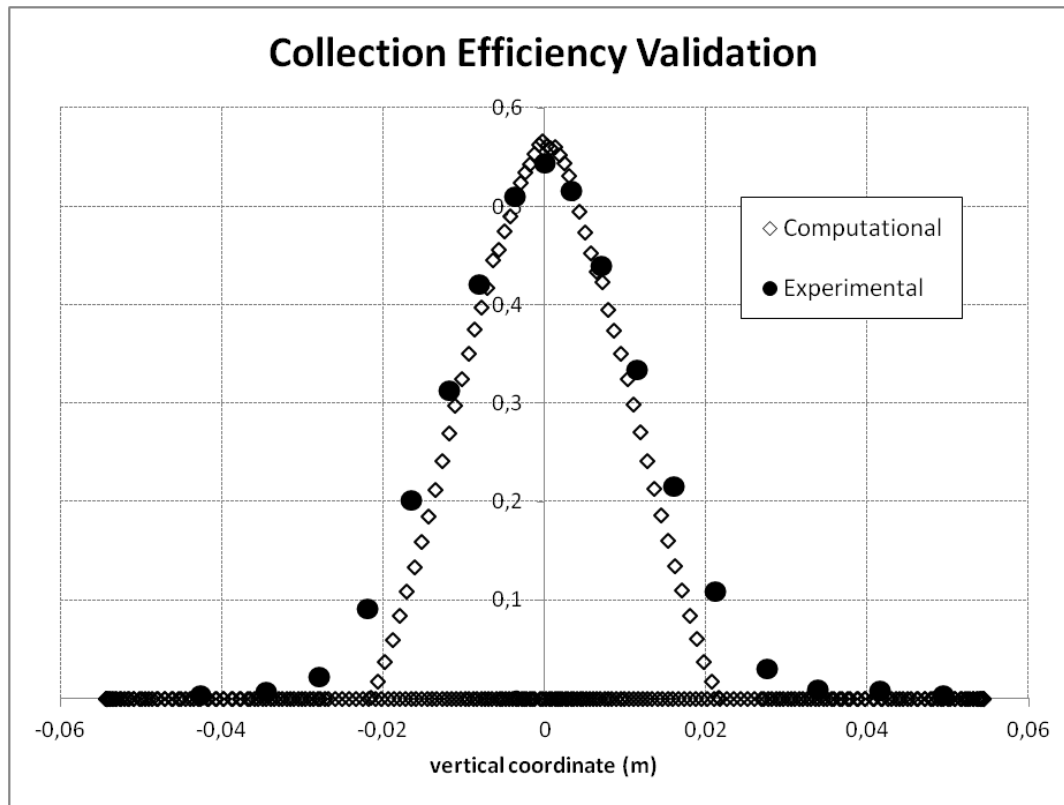
Figure 2-1 Comparison of collection efficiency with experimental data

As we have seen, the peak value of the collection efficiency at the stagnation point is slightly over predicted. Moreover, the numerical algorithm predicts that the water particles will strike the

surface in a narrower range. This is because only one particle size is represented in the simulation. As larger particles tend to hit the surface instead of being carried by the air stream, the collection efficiency near the impingement limits would be higher if a droplet distribution had been used. This feature is not available in ANSYS FLUENT; however, a range of droplet sizes can be simulated separately and mass weighted average collection efficiency can be computed.

The effect of droplet size on collection efficiency is shown in Figure 2-2. As we have seen, as the droplet size increases, the collection efficiency of the body of the blade also increases, as larger droplets cover more space on the surface and their inertia is greater.
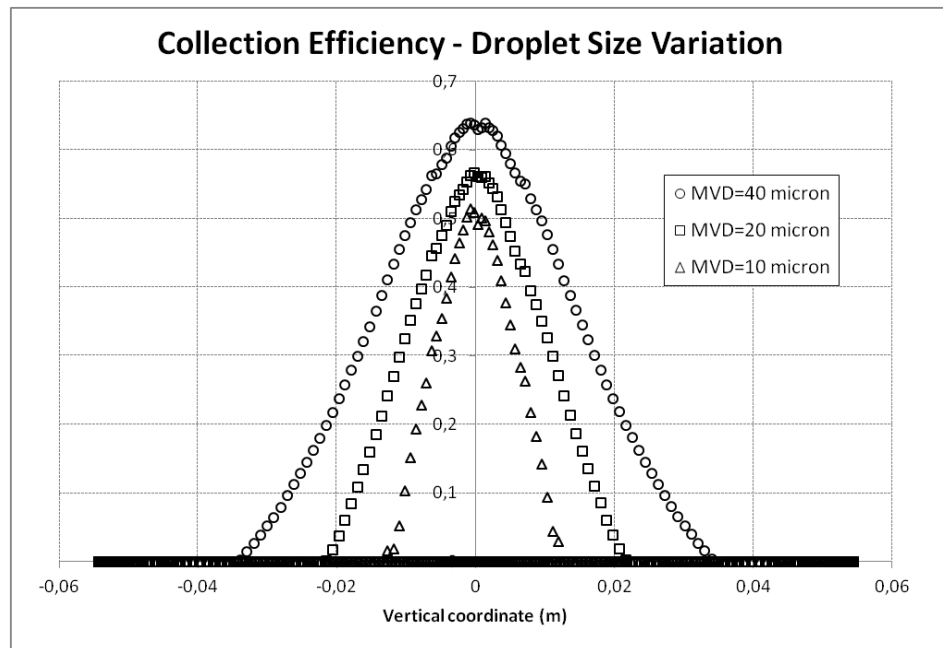
Figure 2-2 Collection efficiency variation with droplet size

2.3 **Phase III – Ice Accretion Computation**

In this phase, we computed the shape of the ice accreted on the wind turbine blades. A numerical heat transfer model is required for ice shape modeling, and for this we chose the extended Messinger model, as proposed by Myers (2001), as a base. We calculated the ice accreted on each computational element using collection efficiency, icing duration, and the mesh coordinates from previous analyses.

The Extended Messinger model is formed by four equations: heat equations for ice and water, a mass balance equation, and a phase change equation known as the Stefan equation. The ice is assumed to be in perfect thermal contact with the surface, so that the ice temperature on the surface is equal to the surface temperature. The governing equations in the Extended Messinger model for heat transfer analysis are the following:

$$\frac{\partial T}{\partial t} = \frac{\kappa_i}{\rho_i c_i} \frac{\partial^2 T}{\partial z^2} \qquad\qquad 2\text{-}12$$

$$\frac{\partial \theta}{\partial t} = \frac{\kappa_w}{\rho_w c_w} \frac{\partial^2 \theta}{\partial z^2} \qquad\qquad 2\text{-}13$$

$$\rho_i \frac{\partial B}{\partial t} + \rho_w \frac{\partial h}{\partial t} = \beta V_\infty (LWC) \qquad\qquad 2\text{-}14$$

$$\rho_i L_F \frac{\partial B}{\partial t} = \kappa_i \frac{\partial T}{\partial z} - \kappa_w \frac{\partial \theta}{\partial z} \qquad\qquad 2\text{-}15$$

where T and θ are the ice and water temperature respectively; B denotes the ice layer thickness and h denotes the water layer thickness; κ_i and κ_w are the thermal conductivity of ice and water respectively; c_i and c_w denote specific heats; and L_F is the latent heat of the solidification of water. As the focus of this study is rime ice formation, the water thickness, h, is set to 0, as super cooled droplets freeze as soon as they hit the surface. One dimensional ice thickness can be obtained using Myers' third equation, which is as follows:

$$B = \left(\frac{\beta V_\infty (LWC)}{\rho_r}\right) t$$

2-16

We can see from the above equation that the heat transfer problem turns out to be a mass conservation issue in the rime ice computation, as we assume a zero thickness for the water film layer. For 3D elements, the mass flow rate $\dot{m}_i$ at the center of each surface element and the corresponding ice thickness h_i are computed using the parameters exported from the multiphase analysis with the following formula:

$$\dot{m}_i = \beta_i LWC_i V_\infty \ (kg/s)$$

2-17

$$h_i = \frac{\dot{m}_i t}{\rho_i A_i} \ (m)$$

2-18

Every node will have a neighbouring cell with a different ice thickness, as depicted in Figure 2-3. Once the ice thickness is computed for each surface element, the average thickness of the ice on the node is computed using Equation 2-19. Since cells in the vicinity will affect the direction of growth of the ice, a new unit normal vector is computed for the node using the area-weighted average of the unit vector components – Equations 2-20 to 2-22. Eventually, this nodal ice thickness will generate a point cloud to represent an ice shape at the end of the ice computation iteration.
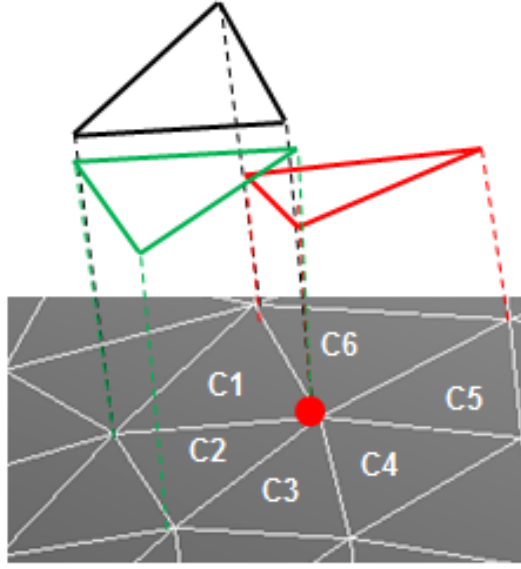
Figure 2-3 Representative node and ice growth in neighbour cells

$$h_j = \frac{h_1 A_1 + h_2 A_2 + \cdots + h_6 A_6}{A_1 + A_2 + \cdots + A_6} \ (m)$$

2-19

$$n_{j,x} = \frac{n_{1,x} A_1 + n_{2,x} A_2 + \cdots + n_{6,x} A_6}{A_1 + A_2 + \cdots + A_6}$$

2-20

$$n_{j,y} = \frac{n_{1,y} A_1 + n_{2,y} A_2 + \cdots + n_{6,y} A_6}{A_1 + A_2 + \cdots + A_6}$$

2-21

$$n_{j,z} = \frac{n_{1,z} A_1 + n_{2,z} A_2 + \cdots + n_{6,z} A_6}{A_1 + A_2 + \cdots + A_6}$$

2-22

The ice thickness can be predicted either by the single-layer approach, in which case the ice thickness is calculated in each cell in one go, or by the multilayer approach, in which case the ice thickness is calculated by dividing the total time of exposure to icing into a number of time intervals. The latter approach leads to better ice shape prediction for longer periods of exposure, since the collection efficiency is recalculated by multiphase flow analysis in increments of ice layer formation, i.e. in each time interval. The reason for updating the collection efficiency is that any change in aerodynamic profile modifies the flow field. Therefore, the velocity field of the droplets and the air flow are both affected, especially at the leading edge.

To perform multiphase analysis on each layer, the mesh around the airfoil or blade needs to be updated according to the ice shape. As the numerical convergence of multiphase simulations is very sensitive to roughness elements, and as these also lead to meshing problems, a surface smoothing is applied on the ice shape to be predicted prior to meshing. However, so as not to miss the roughness effect, the computed roughness size is implemented in the numerical algorithm. The details of this step are given in Chapter 6.

2.4 Phase IV – Iced Blade Analysis

The objective in this phase is to compute the power of an iced rotor. The same procedure as in Phase I will be applied in this phase. However, the relatively complex structure of the ice calls for a denser grid on the surface, and entails a correspondingly higher computational cost. Moreover, because the presence of leading edge ice disturbs flow, numerical convergence becomes more difficult than it is for the clean blade configuration.

Before simulating the iced blade, a grid sensitivity study is performed based on the ice shape created during the worst icing conditions. There are almost three times as many nodes on the iced blade as there would be on a clean blade to catch the surface deviations. For this study, a mesh size in the 4-6 million node number range is tested. Although the number of blade surface elements may change, the prism layer characteristics and the growth rate of the tetrahedral elements are kept the same. The sensitivity of the pressure distribution on various sections and the resultant moment characteristics are tracked. As a result, grid insensitivity is ensured with a 5.5 M grid.

The iced blade is generated using the NURBS function, and the Rhinoceros (2014) software provides the average deviation for the surface. This average deviation is assigned as surface roughness in the iced blade analysis to simulate the effect of these icing elements.

2.5 Phase V – Power and Energy Loss Modeling

The objective in this phase is to quantify power and energy loss for a sample wind turbine and for a sample wind farm. To achieve this, the maximum, minimum, and average values of the icing conditions, namely MVD, icing duration, and wind speed, are gathered from the measurements performed on a wind farm in Sweden. Using these data, the Annual Energy Production is computed for both nominal and iced configurations.

The Annual Energy Production (AEP) is the total energy generated by a single wind turbine at a particular location in one year. To compute the AEP, wind speed frequency data for the location are required (in general, a Weibull distribution), as well as a power curve for the machine. Although the AEP depends on many parameters, such as the availability of the machine and array losses, only contamination losses are considered in our computation. The AEP is computed using Equation 2-23.

$$AEP = T \int_{V_{cut-in}}^{V_{cut-off}} P(V) f(V) dV$$

2-23

where V_{cut-in} and $V_{cut-off}$ are the cut-in and cut-off wind speeds between which the wind turbine can safely operate; $P(V)$ is the power curve of the machine; and $f(V)$ is the Weibull wind frequency distribution of the wind at the site. This distribution is computed (in Equation 2-24) by a function that depends on a scale parameter, c, which is proportional to the average wind speed and a shape parameter, k, The parameters, k and c, are unique for a wind farm.

$$f(V) = \left(\frac{k}{c}\right)\left(\frac{V}{c}\right)^{k-1} e^{\left[-\left(\frac{V}{c}\right)^k\right]}$$

2-24

To compute the energy production of the iced blade, the nominal and iced blade energy production figures are computed for the time interval defined by each icing event. In an icing event of 45 hours – shown in Figure 2-4 – only a 15-hour period of ice accretion period was recorded. The remaining 30-hour period is the time during which ice remains on the blade without shedding or melting. In the power production graph, the power level decreases for 15 hours and it remains constant after this point. The area below the power curves represents the energy produced by the iced wind turbine and the nominal energy production.

Power production for an icing event
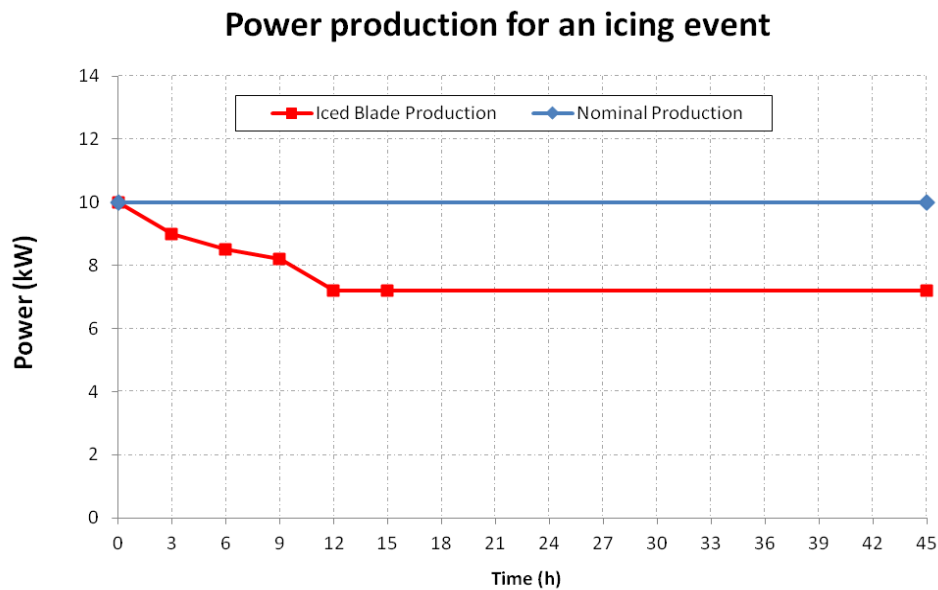
Figure 2-4 Power production during an icing event and nominal production

All the icing events occurring during the reference year are compared in the table below. The total energy produced by clean and iced blades during the reference year were computed separately. Finally, actual AEP produced by iced blade was computed using Equation 2-25.

Table 2-1 Icing events for a wind farm and corresponding energy production.

Icing Event	Nominal Energy	Iced Energy
1	En(1)	Ei(1)
2	En(2)	Ei(2)
3	En(3)	Ei(3)
…	…	…
…	…	…
Total	Nominal Energy prod.	Iced Energy production

$$AEP_{actual} = AEP_{nominal} - E_{t\_nom} + E_{t\_iced}$$

2-25

Chapter 3   ARTICLE 1: ISSUES CONCERNING ROUGHNESS ON WIND TURBINE BLADES

Ece Sagol[a], Marcelo Reggio[a], Adrian Ilinca[b]

[a] Polytechnique Montréal, 2500 Chemin de Polytechnique, Montréal, QC, Canada H3T 1J4

[b] Université du Québec a Rimouski (UQAR), 300, allée des Ursulines, Rimouski, QC, Canada G5L 3A1

3.1 Abstract

This paper reviews the effects of surface roughness, accreted on wind turbine blades, on the flow field and power generation. Contamination agents, like dust, dirt, ice, and even insects accumulate on the blades and generate roughness to varying degrees. These roughness elements, depending on their size, location, and density, may disturb the flow field and reduce the power produced by the machine. A review of papers addressing similar flow patterns is provided, along with an analysis of the ability of numerical algorithms to correctly predict the power performance and the flow characteristics in the presence of surface irregularities. Finally, solutions are given to mitigate the effects of roughness on power production.

3.2 Introduction

The world's demand for energy is increasing due to rapidly growing population and industrial production. Although fossil fuels are still the primary and the most widely used energy source, problems related to their contribution to global warming and finding new supplies are prompting us to seek cleaner and more sustainable alternatives, i.e. renewable energy. Prominent among those alternatives is wind energy, which is widely available at a competitive cost. Wind turbines can be exposed to dramatically different operational conditions, from icy, arctic-type environments to deserts with sand storms, and there are contaminants in all of them, like dust,

dirt, ice, and even insects, that affect the surfaces of a wind turbine blade. These contaminants generate irregularities on this once smooth surface, perturbing the flow field around the blade. The affected wind turbines produce less energy than expected, which leads to an economic problem beyond the initial engineering challenge. This paper is structured in several parts to explain the issues related to the effects of surface roughness on wind turbine blade aerodynamics. In the first part (Section 3.3), the circumstances leading to surface contamination are described, with a brief description of the physical characteristics of roughness. In the second part (Sections 3.4 and 3.5), the effect of surface roughness on blade aerodynamics and turbine performance is analyzed, emphasizing the experimental results available in the literature. Then, numerical algorithms that simulate the presence of roughness are examined, with special attention given to turbulence modeling (Section 3.6). Finally, solutions to reduce the impact of roughness are reviewed, and the design of airfoils that are 'impervious' to roughness is considered (Section 3.7).

3.3 Surface Roughness and Its Sources

Wind turbines are unavoidably exposed to the environmental conditions that prevail in the location where they are erected. The environment may be harsh, or it may contain particles, and even insects, that erode or contaminate the blade surfaces. Of these contaminants, dust, ice, and insects are the agents known to increase the roughness of the blade the most (Weiss; KellyAerospace; BladeSmart). Figure 3-1 shows examples of contamination by these agents and of the effects of erosion.

3.3.1 Dust accumulation

Small particles of dust, dirt, and sand can be transported by the wind to the height of the wind turbine rotor. As these particles hit the rotor blade, the smoothness of the surface is perturbed, especially at the leading edge, near the stagnation point. While dust contamination has not been extensively examined, a few studies have resulted in some key findings which explain the effects of dust roughness on wind turbine blades, and the relationship between power output, the duration of dust exposure, and grain size.

In the study by Khalfallah and Koliub (2007), the effects of dust accumulation on a 300 kW pitch regulated wind turbine, over various operational periods, are examined. As expected, the dust

accumulation pattern follows the blade profile, with the highest concentration of particles on the leading edge and the tip of the blade.

3.3.2 Insect contamination

Although there is no doubt about the possibility of insect contamination on wind turbine blades, the presence of insects was not considered a source of a significant power loss until recently. At wind farms in California (Corten & Veldkamp, 2001), different power levels were detected in several wind turbines. In other words, the turbines showed multiple power curves for the same wind speed. To find the source of this phenomenon, Corten and Veldkamp (2001) developed several hypotheses, all of which have been examined experimentally. They validate the possibility of insect accretion, concluding that wind turbine blades are contaminated only at low speed winds in which insects can fly. At these speeds, power production is not significantly influenced by roughness. However, at high wind speeds, there is a remarkable decrease in power output due to surface roughness generated by insects. Moreover, according to this hypothesis, the contamination level also depends on the atmospheric conditions in which insects fly: above 10° C, and when it is not raining. Very low temperature and low humidity also contribute to an insect-free environment (Lachmann, 1960). In addition to atmospheric conditions, insect presence also depends on altitude, with a rapidly decreasing density from ground level to 500 ft (Petrone, de Nicola, Quaglierella, Witteveen, & Iaccarino, 2011). The conditions for insect contamination are schematized in Figure 3-2. The increase shown in the power curve is the result of the blades having been cleaned by rain.

To validate the hypothesis, two juxtaposed wind turbines were investigated experimentally at the same wind farm. The first turbine, a clean one, was subjected to natural contamination by insects, and an artificial surface roughness was applied to the second one. The power outputs of these turbines were periodically recorded during the experiment. Initially, the first one generated more power than the second. As the contamination level increased over time, the power level of first turbine decreased, and approached the power production of the second turbine. In other words, natural contamination generated a level of surface roughness equivalent to that of the second turbine. These results validate the hypothesis that insect accumulation, by increasing the roughness of the blade surface, leads to power reduction (Corten & Veldkamp, 2001).

3.3.3 Ice Accumulation

The influence of accreted ice has been extensively studied, both for airplanes and wind turbines, as the consequences and risks are considerable for the operation of these machines. Ice accumulates as super cooled water droplets present in clouds strike the solid surfaces and freeze on contact. The ice shapes that form on these machines and their effect on performance are schematized for different types of ice accretion in Figure 3-3 (Bragg, Broeren, & Blumenthal, 2005). The ice build-up on these structures is classified as glaze (horn) ice, rime (streamwise) ice, ridge ice, and ice roughness. Glaze ice is horn-shaped, and forms where a thin water layer covers a thicker ice layer. This horn shape originates from the runback water that does not freeze on impact, but after moving towards the trailing edge. Rime, or streamwise ice, contains ice layers that form at the intersection of water droplet streamlines and solid surfaces. As indicated in Figure 3-3, rime ice has a less negative effect on the flow field, whereas glaze ice, because of its shape, has more. These two ice formations, because they occur the most frequently, are the types most often studied in the literature. Ridge ice forms as a single large obstacle on the suction side of the turbine, and causes a huge separation bubble, deforming the flow field more significantly than the other types of ice. Finally, ice roughness refers to any type of icing at early stage in its formation, where water droplets are not able to form an ice layer, but can perturb the profile of the blade. Although ice roughness exists at the initial stage of any type of icing process, it can influence performance substantially, the extent of its effect depending on its height, concentration, and location. Ice roughness modifies the thickness of the boundary layer and the extent of its transitional characteristics, which depend on its height, location, and Reynolds number. Consequently, the corresponding aerodynamic characteristics, like lift and drag coefficients, are influenced as well. These phenomena are addressed in detail in the next sections.

3.3.4 Other Roughness Sources

In addition to contamination induced rough ness, surface finishing and surface degradation due to erosion also contribute to roughness effects on wind turbine blades. As well, poor surface finishing may cause power loss during operation. As a protective layer and to reduce the level of roughness, paint is applied to the blade surface. Pechlivanoglou (2010) has published the resulting surface roughness for various painting processes—see Table 3-1 . The technique of spraying generates minimal roughness on the surface; however, special care must be taken to

prevent any particles from sticking to the surface during the process, as these would raise the surface roughness level.

3.3.5 Characterization of Roughness

Whatever the source, dust, ice, or insects, roughness on a surface is characterized by its height, concentration, and location. Roughness height refers to the size of a single roughness element, or an average of multiple roughness elements, on a surface. Roughness size can be defined by its height from the surface for randomly shaped elements, and by its diameter for spherical elements. However, to compare several cases accurately, the roughness height, k, is non-dimensionalized by the chord length, c, and represented as k/c. Consequently, for applications with similar Reynolds numbers, the aerodynamic characteristics can be compared based on the k/c value. Roughness density refers to how densely the roughness elements are distributed on the surface. The effects of various roughness configurations, namely densely and sparsely distributed elements, have been investigated in many studies. Finally, roughness location refers to the area where the roughness elements are present. As the contamination particles follow the streamwise flow, they tend to build up near the stagnation point, which is usually at the leading edge. The dependency of turbine performance on these parameters is explained in following sections.

3.4 Effects of roughness on flow field

From the fluid dynamics point of view, roughness can be defined as a surface extension of a body that penetrates into the viscous layer. These elements increase the interaction surface between fluid and solid, causing irregularities and disturbing flow field within the boundary layer. Consequently, momentum and energy transfer between the surface and the flow will increase, which will affect the aerodynamic performance of the airfoil. According to the stability theory explained by Schlichting (1979) , there are small fluctuations in the flow quantities, which are velocity, pressure, density, and temperature. If these fluctuations are substantial enough to affect the mean flow quantities, a transitional period will occur, during which the flow will change its regime from laminar to turbulent. This transition is illustrated in Figure 3-4.

As we can see from the figure, while the flow is laminar at the upstream point 1, it reaches a critical Reynolds number and the transition process starts. During the transition, from point 2 to point 6, various complex flow structures are formed. Depending on the characteristics of the flow and the surface, some of these stages could be bypassed or extended. Several studies (Schlichting, 1979) (Busch, 2009) (Turner, Hubbe-Walker, & Bayley, 2000)have shown that there are two important effects of surface roughness on the boundary layer transition: the transition point moves upstream on the wall, which implies an early transition and a prolonged period of transition. To validate these effects, Turner et al. (2000) performed flow visualizations of boundary layers for both clean and rough surfaces. Although this study was intended to investigate roughness elements for turbomachine blades, it is also useful in helping to explain the flow behavior for rough and curved surfaces for Reynolds numbers of around $5*10^6$. As we can see in Figure 3-5(a) transition of the flow from laminar to turbulent was observed for the clean configuration, whereas only a turbulent boundary layer was observed for the rough configuration (Figure 3-5(b)). It is clear that leading edge roughness provokes early transition of the boundary layer. Moreover, Laser Doppler Anemometer (LDA) measurements on the viscous layer of the clean and the rough configurations (graph in Figure 3-5) shows that the turbulence intensity for the rough configuration is significantly higher near the wall, and, although not illustrated here, the streamwise velocity gradient is less stable. This is to be expected, as the area of the turbulent boundary layer of the rough surface is larger in this case. Kerho and Bragg (1997) also examined the transition on a NACA 0012 airfoil for various Reynolds numbers, roughness locations (s), and roughness sizes. Results show that roughness elements cause a slower transition of the boundary layer, depending on roughness size and location, as well as Reynolds number. In Figure 3-6, the lower Reynolds number flow does not seem to be significantly affected by the size of the roughness elements. Various studies (Bragg, Broeren, & Blumenthal, 2005) (Pechlivanoglou, 2010) (Schlichting, 1979) (Busch, 2009) (Turner, Hubbe-Walker, & Bayley, 2000) (Kerho & Bragg, 1997) (Ferrer & Munduate, 2009) how that there is a critical Reynolds number under which flow field and performance are not affected by the presence of roughness elements. At higher Reynolds numbers, the effect of roughness becomes very significant, regardless of its size and location. The transitional area also increases relative to that of a clean configuration. The change in the size of the transitional area has direct effect on the aerodynamic coefficients (lift and drag), and is discussed in the following section.

Roughness elements also modify the level of turbulence intensity on the surface. Bragg et al. (2005) presented an example of turbulence intensity increase for clean and rough NACA 0012 configurations for a Reynolds number of $1.25*10^6$. As shown in Figure 3-7, roughness elements not only provoke early transition, but also contribute to higher turbulence intensity levels during the transition.

3.5 Effects of Roughness on Performance

As mentioned, roughness on a blade surface degrades wind turbine performance by decreasing the maximum lift coefficient and increasing the drag coefficient. To quantify the performance loss due to roughness, several researchers (Ferrer & Munduate, 2009) (Freudenreich, Kalser, Schaffarczyk, Winkler, & Stalh, 2007) (Timmer, 2009) (Li, Li, Yang, & Wang, 2010) (Gregory & O'Reilly, 1973) have performed wind tunnel experiments and numerical simulations on wind turbine blades and airfoils. For the S814 airfoil, a molded insect pattern with a roughness size of **k/c** = 0.0019 was applied to the model surface in a wind tunnel by Ferrer and Munduate (2009). Figure 3-8 shows lift and drag coefficient curves for various angles of attack and Reynolds numbers. The lift coefficient decreases, especially for higher angles of attack, for both positive and negative values. The viscous drag increases with roughness, whereas the pressure drag is affected at higher angles of attack where separation takes place.

Although applying a molded pattern for the simulation of a rough surface may represent the real cases quite well, it is not practical in terms of cost and application time. For this reason, roughness on a surface is usually simulated using various contamination agents or strips, or other roughness elements. For example, Busch (2009) proved that a roughness can be simulated by applying grit to the surface. Results of the simulations on a NACA 23-012 airfoil in a refrigerated wind tunnel are shown below in Figure 3-9 (a) and (b). As seen, modeling with a 3D casting model and with grit roughness generally yield similar lift and drag coefficients. It can be concluded that, although there is a bias in the drag coefficient at low angles of attack, applying grit can replace 3D casting to simulate roughness on a surface, and it is cheaper and more practical.

In the paper by Freudenreich et al. (2007) , clean and rough configurations of a thick, state-of-the-art wind turbine blade are investigated experimentally and numerically. Three different roughness configurations are examined. A tripping wire 1 mm in diameter was applied to the suction side at 0.3c; 0.4 mm and 0.6 mm zigzag tapes were applied to the suction side at 0.05c and 0.1c, respectively; and, finally, 60 grain carborundum (Carborundum 60) was applied to the leading edge of the model, up to 0.07c of both the suction and pressure sides. The latter configuration has greater roughness density and a more realistic roughness distribution. The tripping wire caused an increase in both the lift and drag coefficients, which is more noticeable in the latter parameter. However, the overall lift-to-drag ratio decreased relative to that of the clean configuration. For the zigzag tape configurations, both the maximum lift coefficient and the lift-to drag ratio decreased. A reduction in these quantities is associated with a reduction in the power production of the wind turbines. The configuration treated with Carborundum 60 represents the most realistic roughness model, as it is applied to the entire leading edge, whereas in the other configurations, it is applied to a section only. Results for this configuration show that the boundary layer goes into early transition at the leading edge. Moreover, as the boundary layer thickens due to the roughness elements, drag increases and early stall is induced. For this configuration, the Reynolds number serves as a stabilizing factor on stall, as the boundary layer thickness decreases with an increasing Reynolds number. An overall comparison of these configurations in terms of lift-to-drag ratio is presented in Figure 3-10, which shows that the maximum lift-to-drag ratio is yielded by Carborundum 60, which is around 40% of that of the clean configuration.

Results of another study (Timmer, 2009) that measured the lift and drag coefficients for clean and rough configurations of a NACA63-x18 airfoil are shown in Figure 3-11 (a) and (b) . NACA standard roughness was applied on the leading edge, up to 8% of the chord on the upper and lower surfaces. Comparing these configurations, it is clear that the maximum lift coefficient decreases by approximately 20%, whereas the drag coefficient almost doubles.

 Li et al. (2010) examined the effect of roughness size and density numerically on a DU 95-W-180 airfoil. Roughness heights ranging from 0.03 mm to 2 mm were applied to the numerical model. As we can see in Figure 3-12, lift and drag coefficients are greatly influenced by roughness height. However, there is a point where these coefficients become insensitive to

roughness height, which is called the critical roughness size in the literature. For this airfoil, the critical roughness height seems to be between 0.5 mm and 1 mm.

Similarly, Bragg et al. (2005) discuss the effect of roughness location and height on the lift coefficient based on data they collected from various studies. Figure 3-13, taken from this study, clearly shows that the maximum lift coefficient loss increases as the roughness size increases. However, the amount of the loss is highly dependent on the roughness location, which we discuss in the next section.

The location of roughness elements on the blade surface is also an important parameter that modifies machine performance. Gregory and O'Reilly (1973) examine the effect of the roughness location on a NACA 0012 airfoil. A typical ice layer of 0.3 mm roughness height is investigated for both sparsely and densely populated roughness elements at Reynolds number $2.88*10^6$.

These experiments show that, when the roughness elements are applied to the trailing edge up to arc length 0.5c of the airfoil, an increase in the drag coefficient and only a slight decrease in the lift coefficient are observed. Moreover, the maximum lift coefficient remains constant. Consequently, it can be concluded that trailing edge roughness has very little effect on airfoil performance. As the roughness distribution approaches the leading edge, the change in performance becomes significant: the maximum lift coefficient gradually decreases from 1.5 to 1.1, the lift coefficient decreases by about 40%, and the drag coefficient doubles at the leading edge. This study also examines the effect of roughness density on airfoil performance. The authors state that more densely populated roughness elements result in worse performance, compared to sparsely populated roughness elements in the same conditions. For airfoils with leading edge roughness and for those that are rough over their entire surface area, the maximum lift coefficient decreases and the drag coefficient increases significantly for all the operational angles of attack.

Ren and Ou (2009) also analyze the effect of roughness location on a NACA 63-430 airfoil using numerical simulation. As seen in Figure 3-14, they conclude that the first half of the upper surface, i.e. the leading edge section, is much more sensitive to roughness than the trailing edge section.

Timmer et al. (2009) demonstrate the effect of "wrap around" roughness, where roughness elements are distributed over the entire surface area of a 64-4xx wind turbine airfoil. Tests were

performed with wrap around roughness and leading edge roughness with NACA standard roughness elements. Results show that wrap around roughness decreases the maximum lift coefficient by about 20%, and increases the drag coefficient by 50%, while leading edge roughness decreases the maximum lift coefficient by about 5% and increases the drag coefficient by about 20%.

Although the roughness period is not a direct characteristic of roughness elements, it is an important parameter for quantifying the effect of roughness on wind turbine performance. The longer the roughness period, the more contamination develops on a surface. This is why we can expect the multiple effects of increasing both roughness size and roughness density during longer roughness periods. Corten and Veldkamp (2001) measured the power curve of an operational wind turbine over time after a cleaning process was carried out. Figure 3-15 shows that an increase in the operation time between surface cleanings decreases the power production of the turbine. However, at low wind speeds, power production is identical for both clean and contaminated wind turbine blades.

Another numerical simulation was performed by Ren and Ou (2009) for continuous operational periods. The roughness height and the roughness area on a surface were estimated using empirical correlation, as proposed by Khalfallah (2007). Predicted lift and drag coefficients are presented in Figure 3-16. Although the drag gradually increases, the lift coefficient shows a sudden reduction before the critical roughness height and the critical roughness area are reached.

3.6 **Numerical efforts for modeling roughness**

As the size of wind turbines grows, it is becoming more difficult and more expensive to perform full-scale experiments. Consequently, computational tools are preferred for the design and analysis of wind turbines. Several efforts (Ferrer & Munduate, 2009) (Ren & Ou, 2009) (Patel & Yoon, 1995) (Durbin, Medic, Seo, Eaton, & Song, 2001) (Knopp, Eisfeld, & Calvo, 2009) have been made to model roughness by modifying wall function terms in turbulence models. Turbulence modeling is an issue that has not yet been completely solved in flow field analysis, and different engineering applications may require different treatments of turbulence modeling for near wall flow. Consequently, modeling roughness where disturbances are created in that flow requires special attention. In the literature, there are some studies in which various turbulence

models have been modified. Although not a recent one, a study by Patel and Yoon (1995) gives a good review of the turbulence models available that are applied to rough surfaces. These authors concluded at the time that the best model was the k–ω model with Wilcox roughness modification.

Later, Durbin et al. (2001) developed a prediction method for the k–ε turbulence model based on inserting a hydrodynamic roughness length into the model transport equations and modifying the boundary conditions of the turbulent kinetic energy equation. These roughness formulations have been validated against experimental data available in the literature. The comparison shows that rough wall boundary layer characteristics can be modeled accurately, except at the beginning of the separation, where there is an adverse pressure gradient. Nevertheless, prediction of this situation is difficult, even for smooth walls.

A more recent study has been conducted by Knopp et al. (2009), who apply a roughness correction to the famous k–ω SST turbulence model. To quantify the characteristics of roughness, they also apply equivalent sand grain roughness to the model. This paper addresses two major shortcomings of the Wilcox roughness correction mentioned above. These are the requirement for a very fine grid resolution near the wall, which increases the computational cost significantly, and poor prediction of the skin friction coefficient. Moreover, the Wilcox roughness modification cannot be applied directly to the k–ω SST model, which is frequently used in aeronautical applications. As it is outside the scope of this paper, details on the turbulence model modification are not addressed here. Comparisons of the lift coefficient over the NACA 65-215 airfoil are presented for the roughness modified Spalart–Allmaras model and the k–ω SST model. As we can see in Figure 3-17, the proposed new method predicts the lift coefficient quite well, compared to Spalart–Allmaras, which overshoots this coefficient at higher angles of attack, for both clean and rough configurations. This advancement is important, since numerical prediction of the maximum lift coefficient is still a problem.

Ferrer and Munduate (2009) have performed numerical simulations on an S814 airfoil using the commercial CFD code ANSYS FLUENT 12.0.3 and panel code XFOIL 6.9. Transition is modeled using Menter–Langtry correlation, and fully turbulent flow is modeled using the k–ω SST turbulence model. For the rough configurations, flow is assumed to be fully turbulent. Comparisons of numerical simulations against experimental data show that the commercial code

predicts lift coefficients well for both clean and rough surfaces, as shown in Figure 3-18. However, for the rough case, the flow is assumed to be fully turbulent, and simulations at higher angles of attack have not yet yielded converging results. So, while current numerical schemes are capable of modeling roughness, they cannot do so at higher angles of attack.

In another study (Ren & Ou, 2009) a NACA 63430 airfoil that is used extensively in wind turbine applications is simulated for both smooth and rough configurations. Numerical simulations are performed assuming fully turbulent flow, in which the $k–\omega$ *SST* turbulence model is applied. Figure 3-19 proves that roughness causes a significant reduction in the lift coefficient and a slight increase in the drag coefficient. As expected, beyond a critical roughness height, the lift and drag coefficients become insensitive to this parameter. A study by Villalpando et al. (2012) has also proved the ability of the $k–\omega$ *SST* model on an iced NACA 63-415 airfoil for various Reynolds numbers and angles of attack.

3.7 Solutions to the roughness problem

Solutions to eliminate the effects of roughness can be categorized as either design solutions or external solutions. Design solutions include the use of airfoils that are specifically designed and optimized for both clean and rough configurations. External solutions, by contrast, include various applications that lessen the effect of roughness on wind turbine performance, like special coatings that decrease the number of water droplets that stick to the blade, deicing equipment, and manual cleaning of the blades.

3.7.1 Specially designed airfoils

The National Renewable Energy Laboratory (NREL), formerly the Solar Energy Research Institute, originated the design of airfoils specifically for wind turbines, as aircraft airfoils generate excessive power at high wind speeds, which results in generator burn-out, and they are very sensitive to surface roughness (Tangler, Smith, & Jager, 1992). So, a variety of airfoils have been designed based on the differing design requirements of spanwise sections and blade sizes. These airfoil families have the following advantages:

- Lower maximum lift coefficient at the tip of the blade to control peak power and prevent generator burn-out;

- Higher maximum lift coefficient at the root location to improve start-up at low wind speeds;

- Less sensitivity to roughness effects by forcing laminar to turbulent transition on both the upper and lower surfaces as maximum lift coefficient is reached.

In Figure 3-20, the power production of SERI blades, which are specially designed airfoils, and AEROSTAR blades, which are aircraft airfoils for clean and contaminated configurations, are compared. The maximum power production of a SERI blade is limited to 65 kW to prevent generator burn-out. The power production of a dirty SERI blade is markedly better than that of the AEROSTAR blade. The corresponding Annual Energy Production (AEP) is also much improved, with a 10% improvement for the clean blade and a 30% improvement for the contaminated blade.

Bak et al. (2008) (2004) also conducted a study to search for a wind turbine airfoil family that is insensitive to roughness and turbulence intensity. In this case, the airfoil geometry was optimized for both the clean and rough configurations by means of a generic quasi 3D multidisciplinary optimization tool, while at the same time maintaining high aerodynamic efficiency and stiffness. The design variable for this optimization is the airfoil shape, and the design objective is the maximum lift-to-drag ratio. The design optimization strategy is schematized in Figure 3-21. The optimization is performed at two locations on the rotor, and the thickness of rest of the blade is obtained through interpolation.

The wind tunnel test results of these airfoils show that the maximum lift coefficient decreases only slightly when roughness is introduced. However, the difference between the clean and rough configurations is more noticeable in the lift/drag ratio comparison. This difference is due to the fact that the behavior of the drag coefficient, unlike that of the lift coefficient, is rather sensitive.

Rooij and Timmer (2003) review the performance of 25–30% thick wind turbine airfoils with an emphasis on roughness sensitivity. Wind tunnel data were derived from the literature, and rotational effects were introduced using the RFOIL code, which predicts aerodynamic performance, including rotational effects. The wind tunnel results for clean and rough configurations are compared in Figure 3-22(a) and (b), respectively, for the DU 91-W2-250, S814, and NACA 63-425 airfoils. As we can see, while the maximum lift coefficient of the NACA airfoil decreases significantly, the lift reduction for the other airfoils is more acceptable.

These results are expected, however, as the NACA airfoil was not specifically designed for wind turbine applications. The lift-to-drag ratio decreases for all airfoils, as the drag remains sensitive to the roughness elements. However, this reduction is even more remarkable for the NACA airfoil.

3.7.2 External Solutions

Vortex generators, surface finishes or coatings, and cleaning are the best known and most widely used solutions for moderating the effects of roughness. Vortex generators located on blades improve flow quality and airfoil performance by preventing separation and increasing lift. Van Rooij and Timmer (2003) review the wind turbine airfoils equipped with vortex generators, and their results are presented in Table 3-2. The application of vortex generators reduces roughness sensitivity, further increasing the maximum lift coefficient of the airfoil.

Surface finishing paints are designed to improve surface quality and extend the lifetime of blades by preventing cracks; however, a painted surface still has some roughness, depending on the type of finish applied. As indicated in Table 3-1, spray painting results in better quality in the absence of any roughness elements in the application environment. Moreover, as Parent and Ilinca (2011) show in their review, nonstick coating applications are being developed for wind turbines. For an icy environment, this application may prevent the build-up of ice particles, and consequently prevent surface roughness. There are other coatings available commercially that ensure minimum dirt build-up (BladeSkyn).

Besides these applications, Lachmann (1960) proposes covering the surface with plastic films, scrapers, or similar materials, applying continuous liquid flow that will remove the contamination on the surface, and implementing boundary layer control to remove the turbulent boundary layer behind the roughened area.

If none of these solutions is applied, there is one ultimate, and basic, solution that is always available, which is manual cleaning of the blades. There are commercial companies that optimize the time required for blade cleaning, as a function of the wind turbine and wind farm characteristics (Blade Cleaning Limpieza de Palas) (Blade access cleaning system for wind turbines).

3.8 **Concluding Remarks**

- Contamination agents like dust, ice, and insects decrease the performance of wind turbines.

- The presence of roughness elements provokes early transition and increases the extent of transitional flow, as well as increasing turbulence intensity near the wall.

- For numerical modeling and wind tunnel experiments, contamination patterns can be replaced by an equivalent sand grain roughness. This eliminates the need for 3D molds in wind tunnel experiments.

- Roughness size, density, and location are the most important parameters influencing wind turbine performance, which tends to decrease with increasing roughness size and density. However, there is a level of roughness height after which the performance remains stable, which is called the critical roughness size. In terms of roughness distribution, the leading edge is the location that is the most sensitive to roughness elements, while trailing edge roughness has almost no effect on performance.

- There is a limit to the Reynolds number under which the performance is not affected.

- Although numerical models are capable of predicting clean wind turbine performance, the accurate simulation of rough configurations is still under development. Currently, k–ω *SST* seems to be the most accurate turbulence model among the two-equation models.

- To lessen or even eliminate the effects of roughness on performance, specially designed airfoils are found to be the best and most widely used solution. When roughness sensitivity is regarded as a design parameter, the resulting airfoils are significantly less influenced by roughness.

Figure 3-1 Rough surfaces of wind turbine blades caused by insects, ice, and erosion, respectively. (KellyAerospace) (Weiss) (BladeSmart)
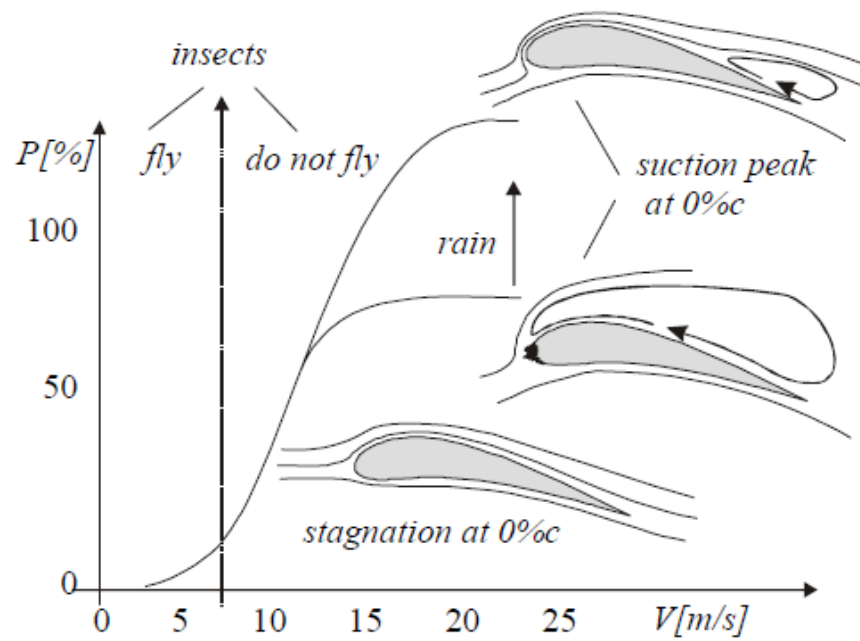
Figure 3-2 Conditions for insect contamination (Corten & Veldkamp, 2001)
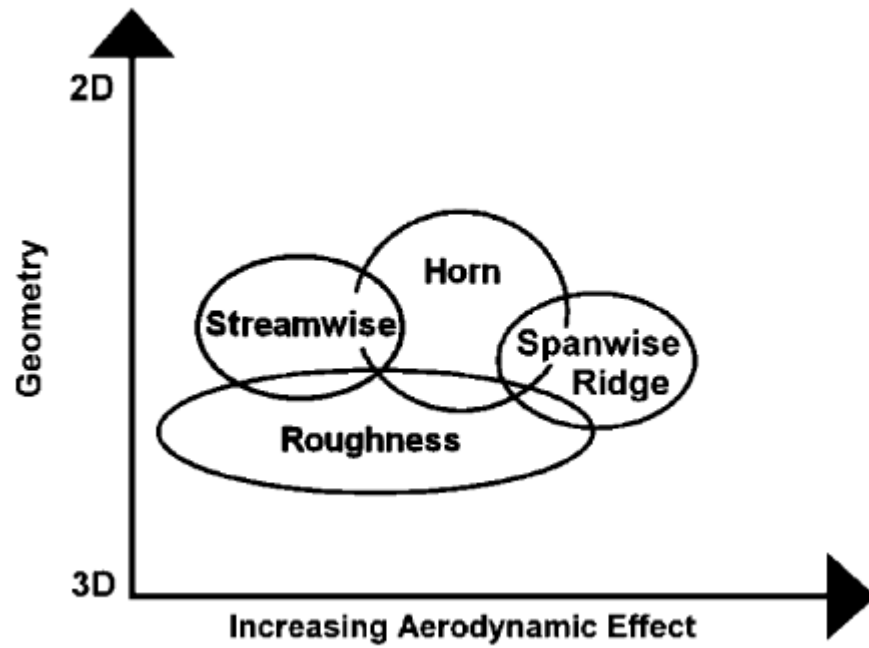
Figure 3-3 Classification of ice accumulation types (Bragg, Broeren, & Blumenthal, 2005)
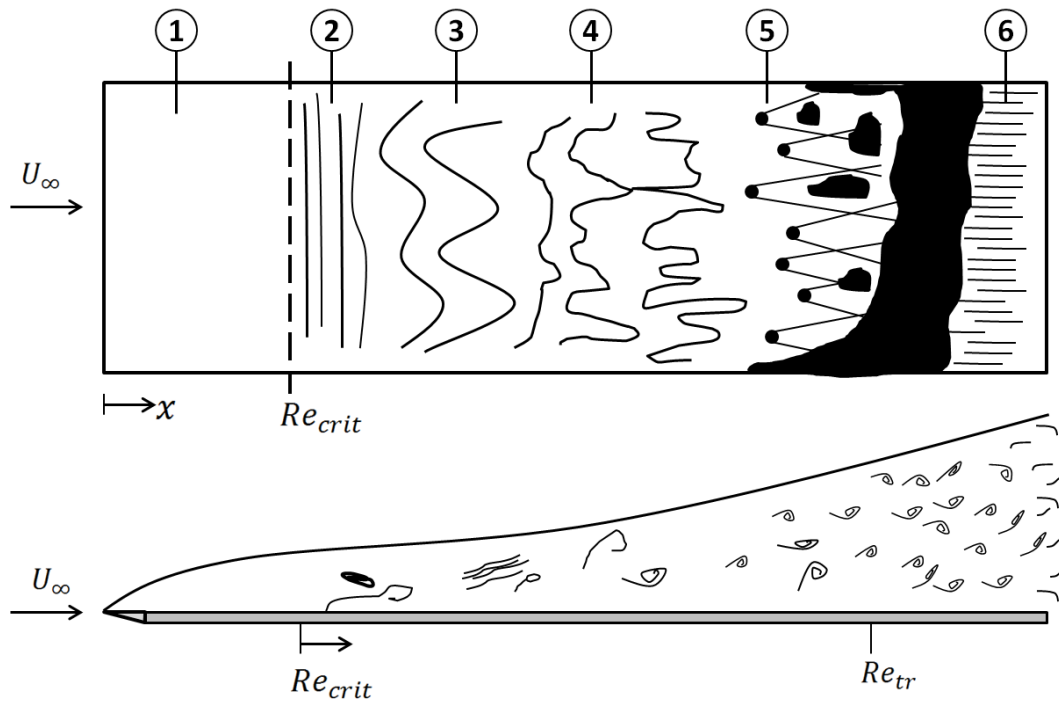
Figure 3-4 Transition from laminar to turbulent flow. Reproduced from (Schlichting, 1979)
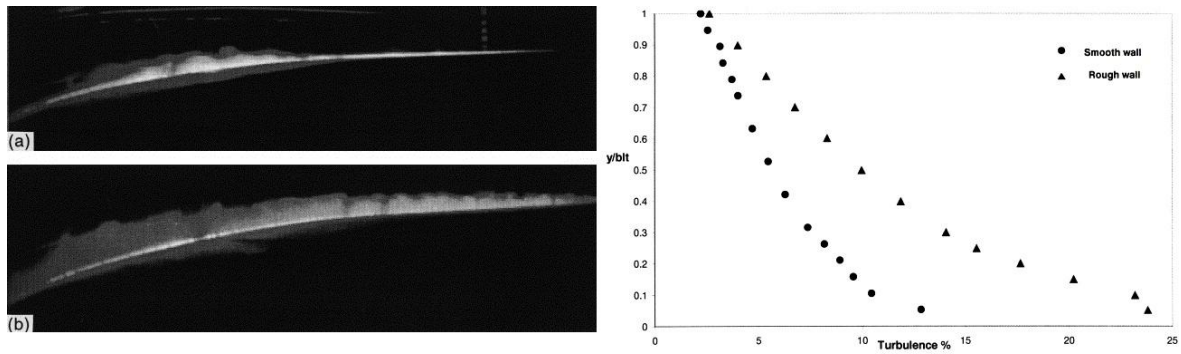
Figure 3-5Boundary layer transition and turbulence intensity: (a) on a smooth surface; and (b) on a rough surface. (Turner, Hubbe-Walker, & Bayley, 2000)
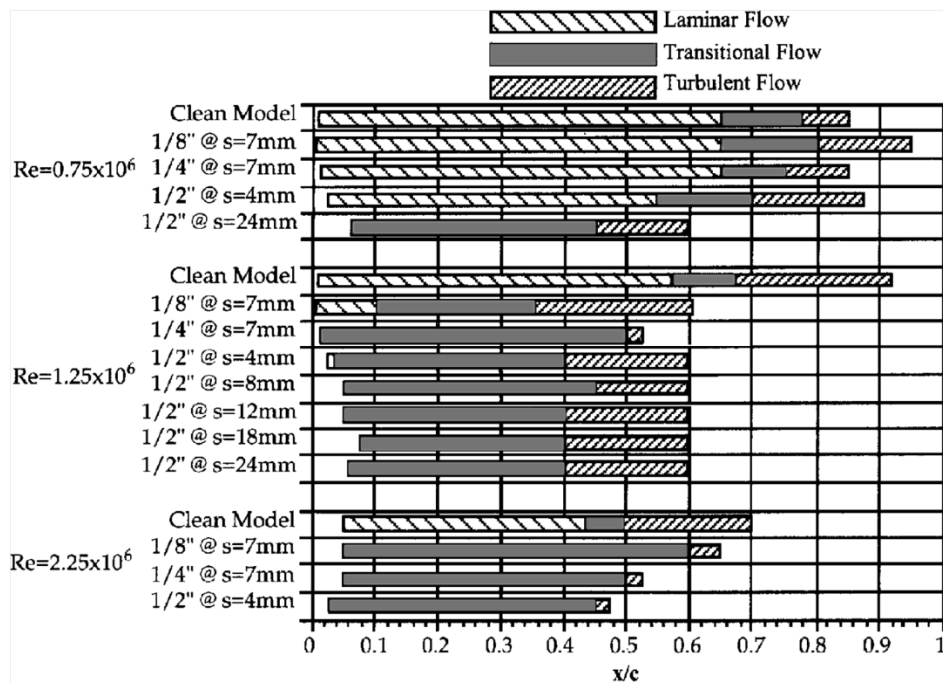
Figure 3-6 Transition over the surface of a NACA 0012 for various Reynolds numbers. (Kerho & Bragg, 1997)
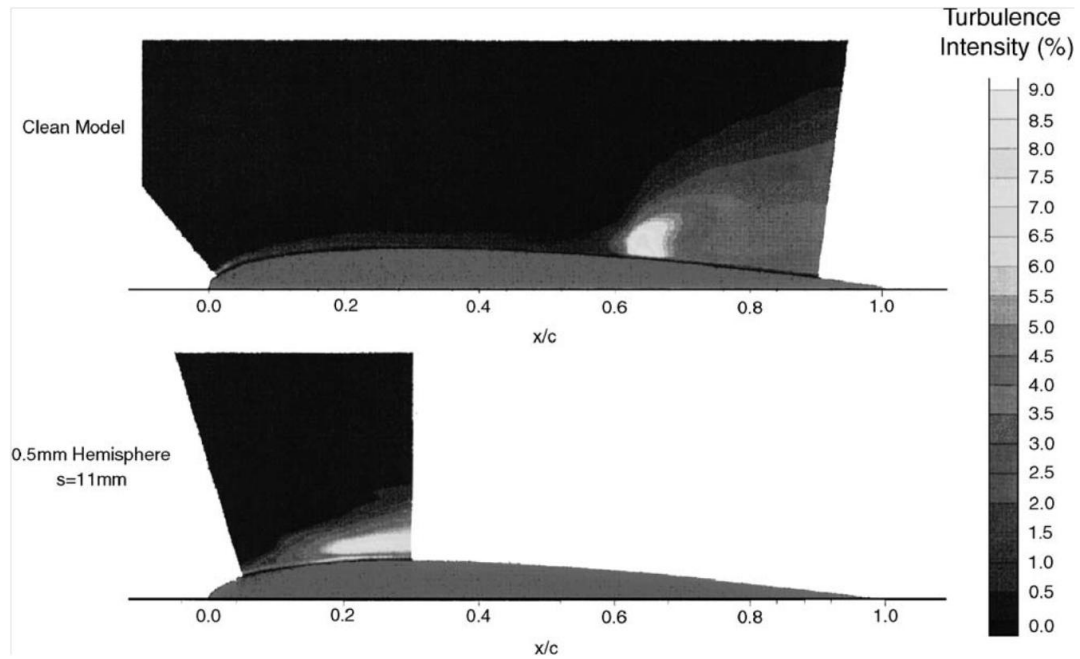
Figure 3-7 Turbulence intensity level for a clean and a rough NACA 0012. (Bragg, Broeren, & Blumenthal, 2005)
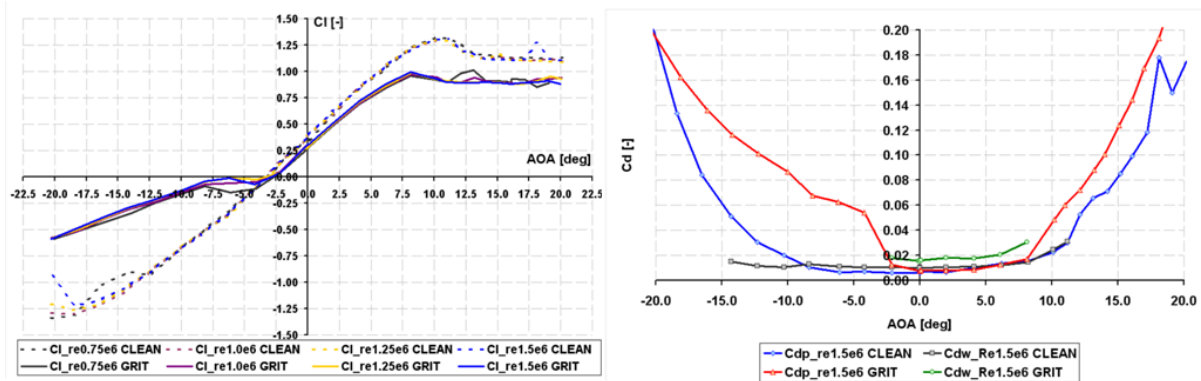
Figure 3-8 Lift and drag coefficient curves for clean and rough configurations. (Ferrer & Munduate, 2009)
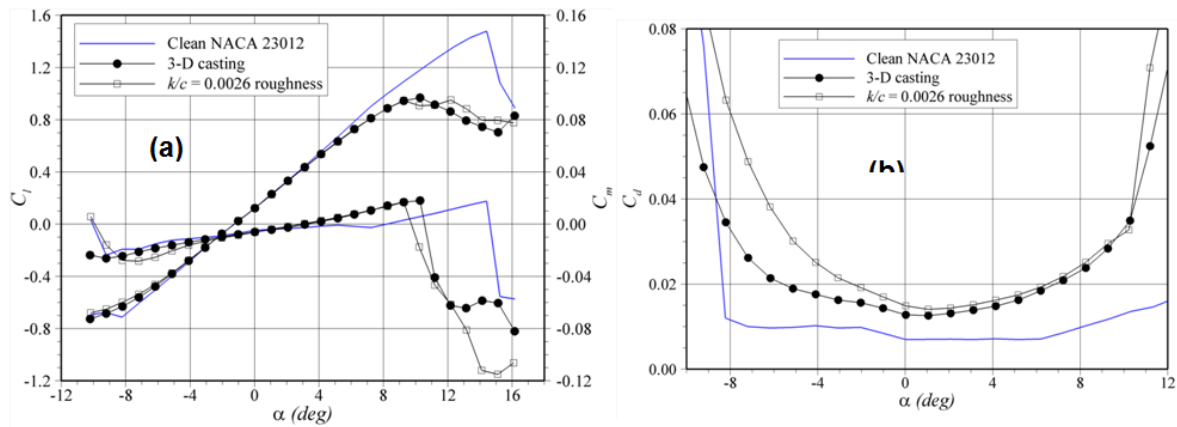
Figure 3-9 (a) Lift; and (b) drag coefficient curves for clean surfaces and surfaces with roughness applied. (Busch, 2009)
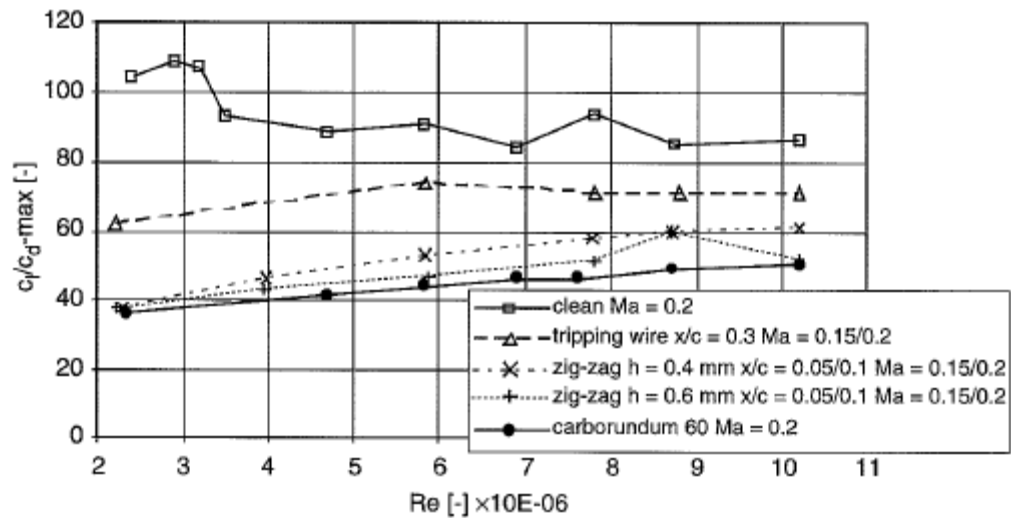
Figure 3-10 Effect of various roughness configurations on a wind turbine blade. (Freudenreich, Kalser, Schaffarczyk, Winkler, & Stalh, 2007)
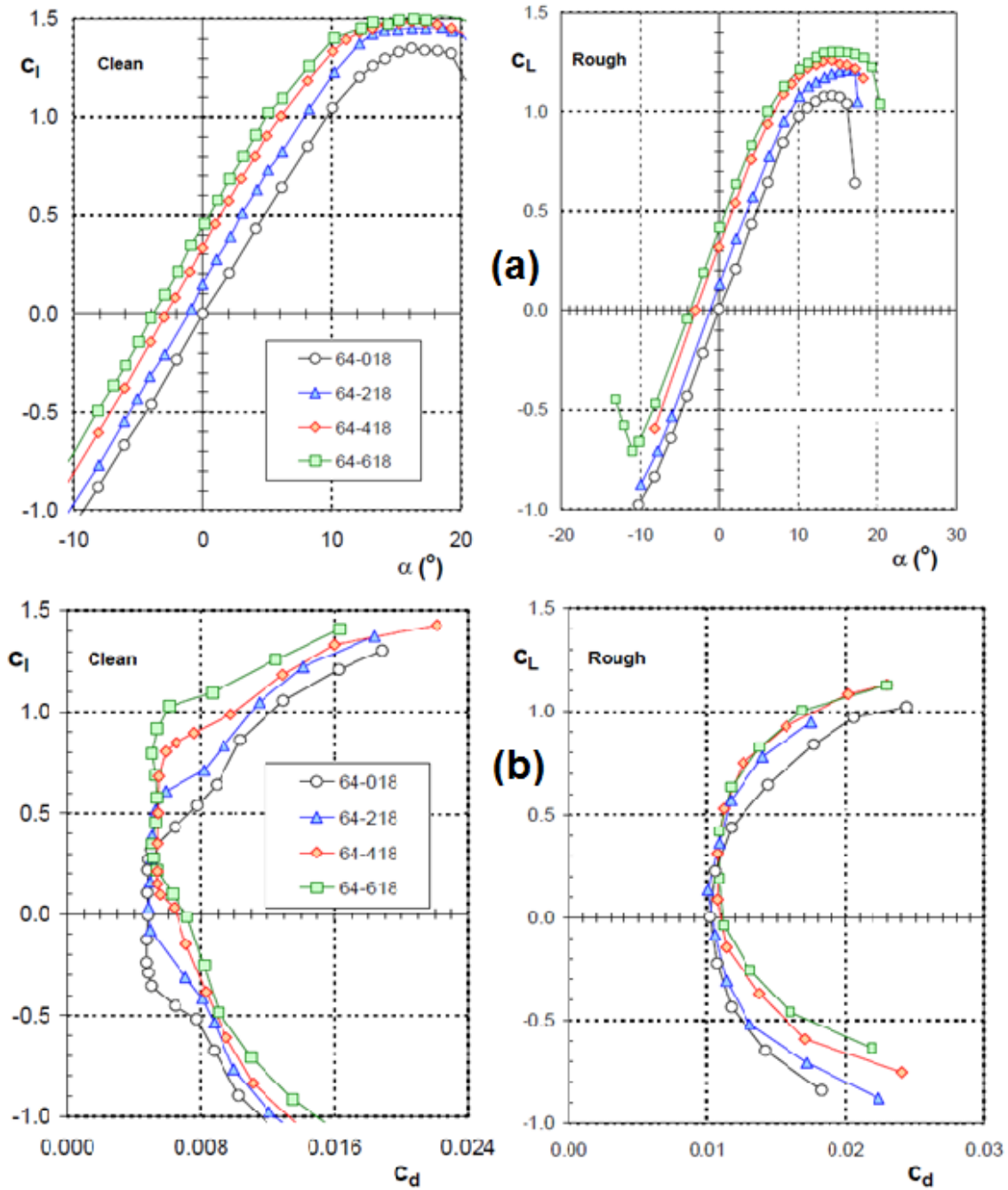
Figure 3-11(a) Lift coefficients of clean and rough members of the NACA 64-x18 airfoil family; and (b) drag vs. lift coefficients of clean and rough members of the NACA. (Timmer, 2009)
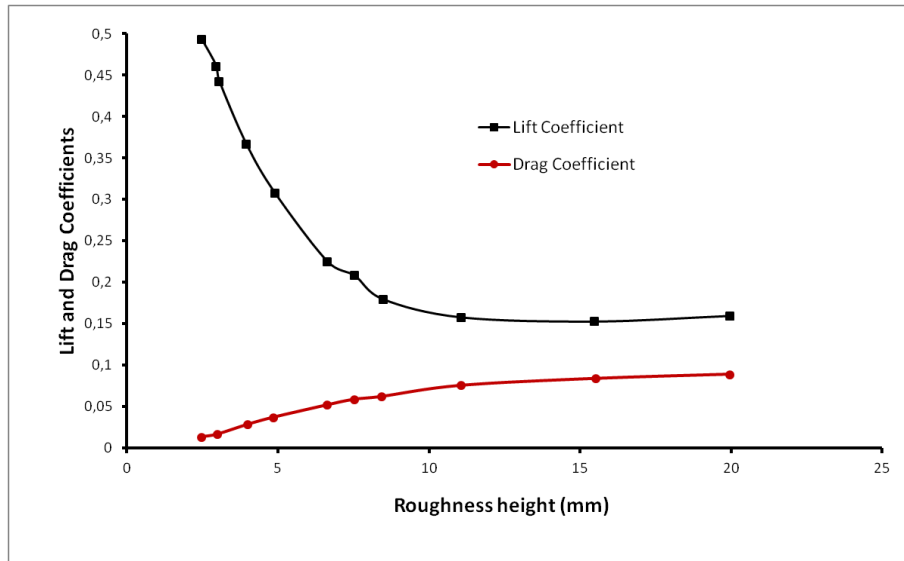
Figure 3-12 Effect of roughness height on the lift and drag coefficients. Reproduced from (Li, Li, Yang, & Wang, 2010)
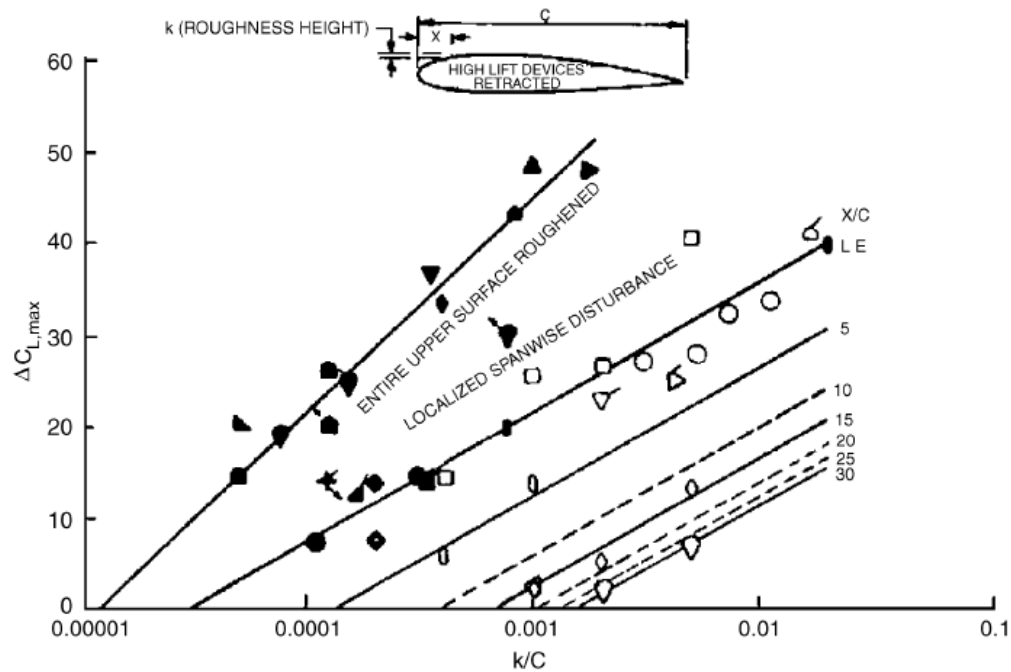
Figure 3-13 Effect of roughness size and location on the lift coefficient. (Bragg, Broeren, & Blumenthal, 2005)
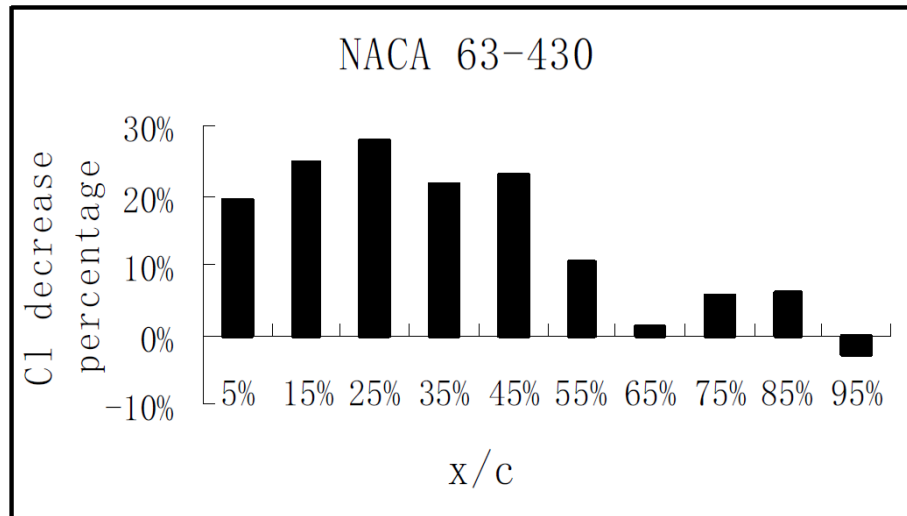
Figure 3-14 Percentage of lift coefficient decrease for different roughness. Reproduced from (Ren & Ou, 2009)
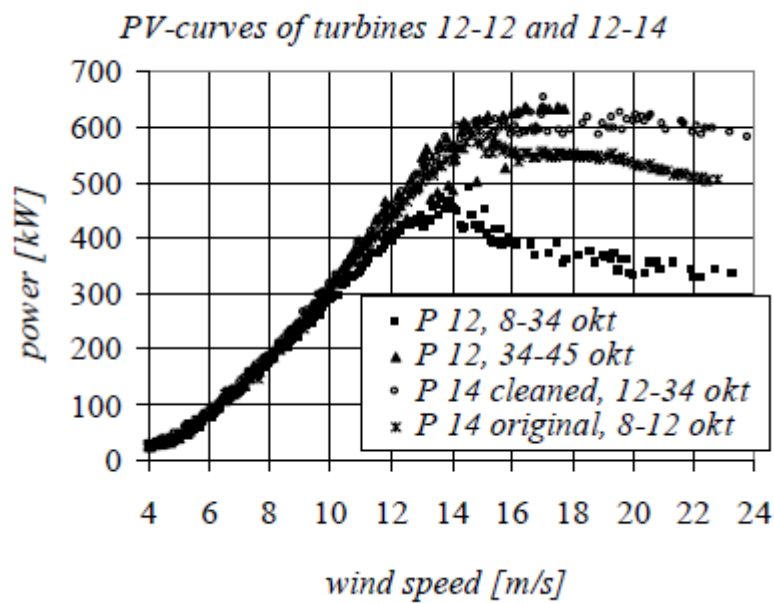
Figure 3-15 Power production over varying operational times. (Corten & Veldkamp, 2001)
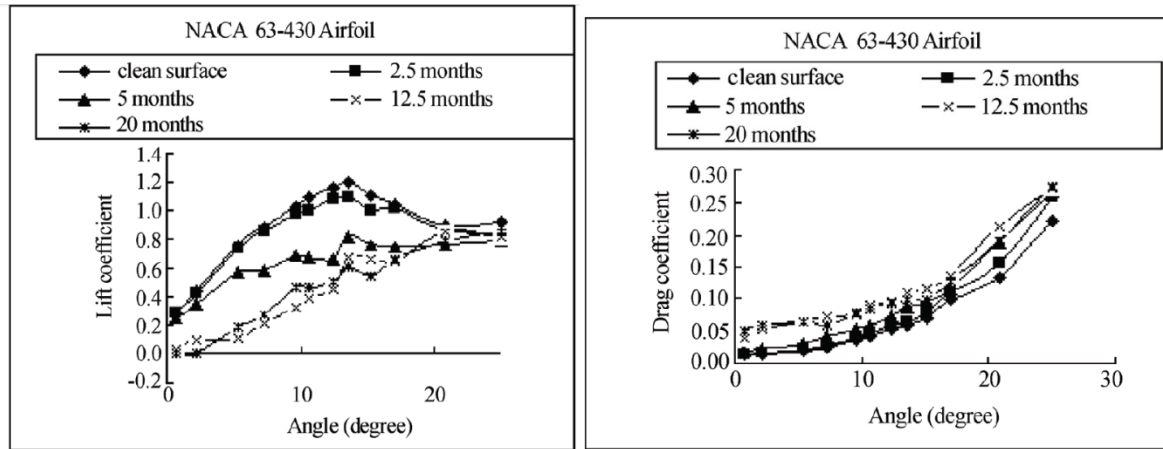
Figure 3-16 Lift and drag curve estimation over varying operational periods. (Ren & Ou, 2009)
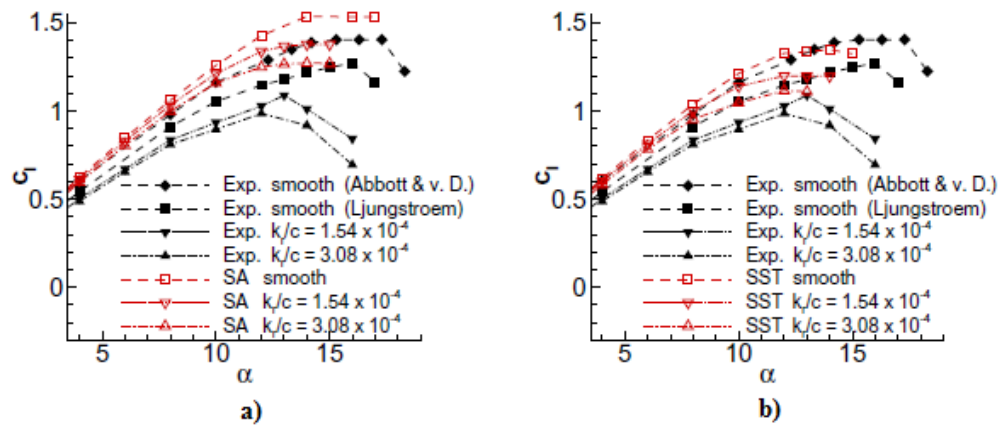
Figure 3-17 Lift coefficient curve comparison: (a) Spalart–Allmaras model; and (b) k–o SST model. (Knopp, Eisfeld, & Calvo, 2009)
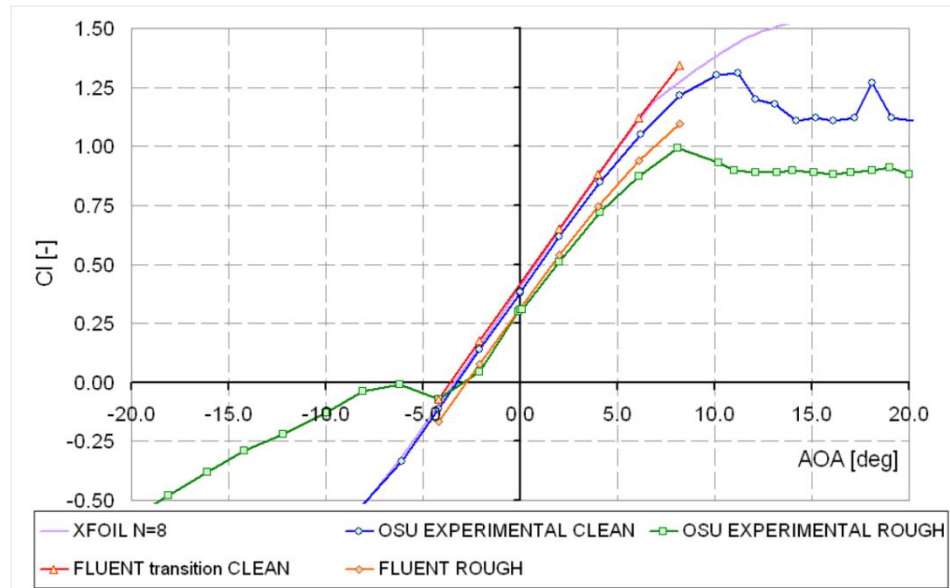
Figure 3-18 Lift coefficient curve of an S814 airfoil from various analyses. (Ferrer & Munduate, 2009)
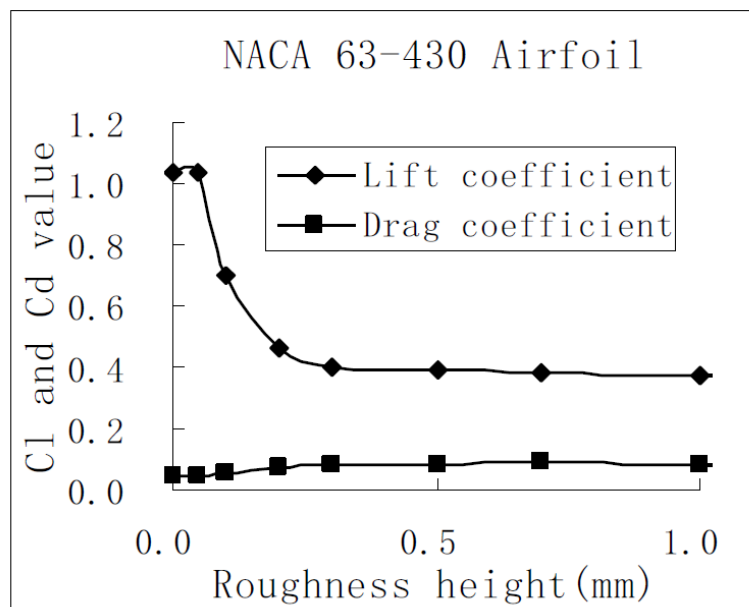
Figure 3-19 Lift and drag coefficients for various roughness heights. (Ren & Ou, 2009)
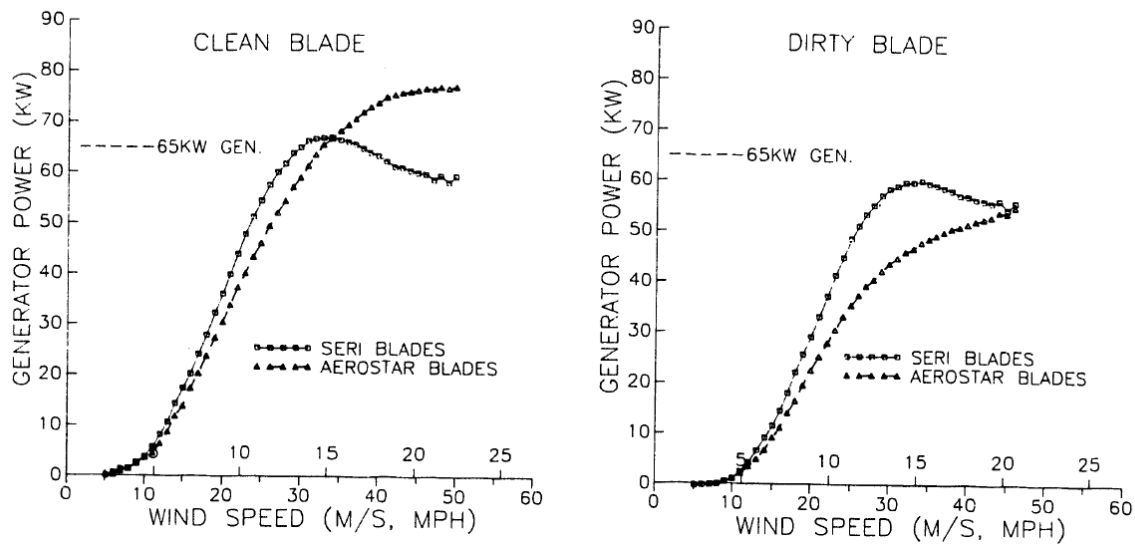
Figure 3-20 Comparison of wind turbine airfoils for clean and dirty configurations. (Tangler, Smith, & Jager, 1992)
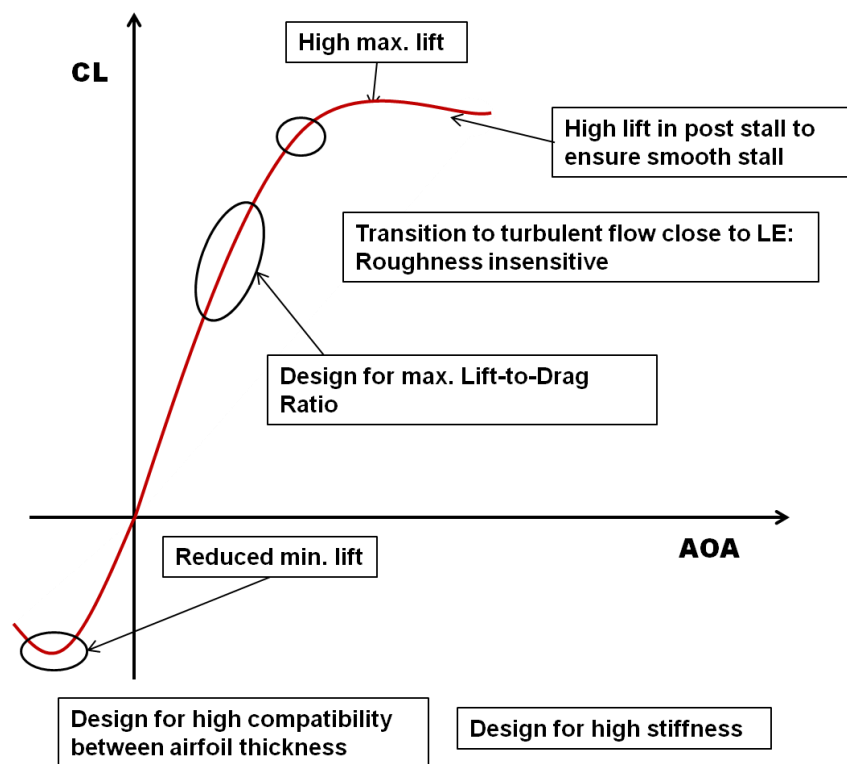
Figure 3-21 Design requirements and objectives for design optimization on the lift. Reproduced from (Fuglsang, Bak, Gaunaa, & Antoniou, 2004)
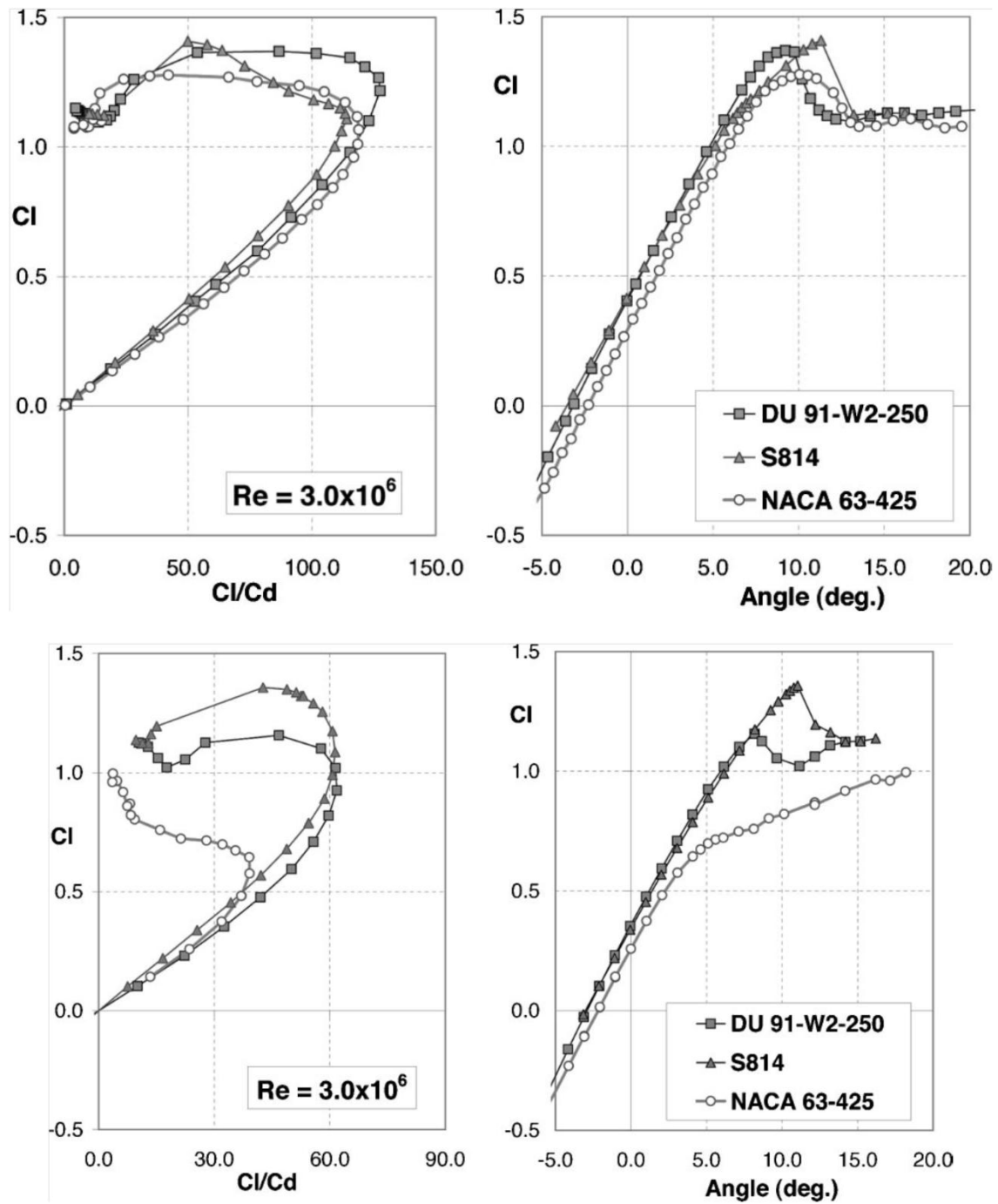
Figure 3-22 Lift coefficient and lift-to-drag ratio for: (a) clean; and (b) rough configurations. (van Rooij & Timmer, 2003)

Table 3-1Roughness values of surface finish applications. Reproduced from (Pechlivanoglou, 2010)

Application Process	Resulting Surface Roughness
Roller	55-80 μm
Roller + Sanding	35-55 μm
Spraying	10-23 μm

Table 3-2 Comparison of wind turbine airfoils with vortex generators. (van Rooij & Timmer, 2003)

Configuration		Clean		Rough	
airfoil	Position VG (x/c)	L/D-max	cl-max	L/D-max	cl-max
DU 91-W2-250	20 %	66.4	1.9		
”	30 %	73.9	1.89		
DU 97-W-300	20 %	63.2	1.97	53.2	1.93
	30 %	69.1	1.88		
RISO-A1-24	20 %	47.1	1.805	41.9	1.77
FFA-W3-241	20 %	45.6	1.543	44.4	1.38
”	30 %	59.1	1.54	51.6	1.43
FFA-W3-301	20 %	38.7	1.636		
”	30 %	39.2	1.36	32.2	1.02
NACA 63-430	20 %	31.9	1.3		
”	30 %	45.6	1.37	36.5	1.13

Chapter 4   **ARTICLE 2: ASSESSMENT OF TWO-EQUATION TURBULENCE MODELS AND VALIDATION OF THE PERFORMANCE CHARACTERISTICS OF AN EXPERIMENTAL WIND TURBINE BY CFD**

Ece Sagol[a], Marcelo Reggio[a], Adrian Ilinca[b]

[a] Polytechnique Montréal, 2500 Chemin de Polytechnique, Montréal, QC, Canada H3T 1J4

[b] Université du Québec a Rimouski (UQAR), 300, allée des Ursulines, Rimouski, QC, Canada G5L 3A1

4.1 **Abstract**

The very first step in the simulation of ice accretion on a wind turbine blade is the accurate prediction of the flow field around it and the performance of the turbine rotor. The paper addresses this prediction using RANS equations with a proper turbulence model. The numerical computation is performed using a commercial CFD code, and the results are validated using experimental data for the 3D flow field around the NREL Phase VI HAWT rotor. For the flow simulation, a rotating reference frame method, which calculates the flow properties as time-averaged quantities, has been used to reduce the time spent on the analysis. A basic grid convergence study is carried out to select the adequate mesh size. The two-equation turbulence models available in ANSYS FLUENT are compared for a 7 m/s wind speed, and the one that best represents the flow features is then used to determine moments on the turbine rotor at five wind speeds (7m/s, 10m/s, 15m/s, 20m/s, and 25 m/s). The results are validated against experimental data, in terms of shaft torque, bending moment, and pressure coefficients at certain spanwise locations. Streamlines over the cross-sectional airfoils have also been provided for the stall speed to illustrate the separation locations. In general, results have shown good agreement with the experimental data for pre-stall speeds.

4.2 **Introduction**

Prediction of the aerodynamic loads on a horizontal axis wind turbine (HAWT) is both an important and a complex process that takes place during the design stage. It is important because it is directly related to crucial characteristics of the wind turbine, such as its power curve, structural loads, and noise generation. The power curve determines the energy output of the wind turbine, and therefore its cost effectiveness, structural loads determine the size of the various wind turbine components and materials to be used, and noise generation is a consideration for the location of a wind turbine and should be kept to a reasonable level. The complexity of a flow simulation around a wind turbine blade to determine aerodynamic loads comes from large angles of attack, a variety of Reynolds numbers resulting from very long blades, and rotational effects. Further complicating the issue is the atmospheric boundary layer, variable wind speeds along the blade, and interaction of the rotor with the nacelle and the tower.

Although 2D and quasi-3D methods like blade element momentum analysis may predict aerodynamic loads up to a certain level, 3D analysis is required to capture all the turbulence features that are inherently three dimensional. As computational cost drops thanks to technological development, the use of computational fluid dynamics (CFD) for wind turbine design and analysis is becoming increasingly widespread and results in a better understanding of the aerodynamic phenomena on the rotor flow field.

Studies on wind turbine aerodynamics in the literature focus on different aspects of the science, like performance analysis, fluid-structure interaction, acoustics, and icing. Investigation into performance analysis is primarily aimed at estimating aerodynamic loads, and the effect of various parameters on these loads. Duque et al. (2000) explored the ability of various methods to predict wind turbine power and aerodynamic loads. Results showed that all the methods, namely blade element momentum (BEM), vortex lattice, and Reynolds averaged Navier Stokes (RANS), perform well for prestall regimes. They found that the RANS code OVERFLOW, although not perfect, gives better predictions of power production for stall and post-stall regime modeling than other methods. Another study, based on CFD analysis (Sorensen, N. N.; Michelsen, J. A.; Schreck, S., 2002), showed that performance and wind turbine load predictions are very accurate, except in the stall region. A commercial wind turbine company, Siemens, analyzed their own large-scale wind turbine using a commercial CFD code, ANSYS-CFX, with transition and fully

turbulent models (Laursen, Enevoldsen, & Hijort, 2007). Transition models improve drag prediction but overestimate the lift compared to fully turbulent models. Benjanirat et al. (2003) used CFD with various turbulence models (Boldwin-Lomax, Spalart-Allmaras, and k-ε), with and without wall corrections, on an experimental wind turbine. The k-ε model with wall correction yielded the best results when compared with experimental data. A more recent study, conducted by Sezer-Uzol and Long (2006) using a generic CFD code, PUMA2, have shown that time accurate inviscid results are also compatible with the experimental data.

Predicting the effects of tower, nacelle, and anemometer on the rotor flow field have also been investigated in several works. Smaili and Masson (Smaili & Masson, 2004) and Zahle and Sorensen (2010) both concluded that CFD is an effective tool for evaluating the influence of the nacelle, even for different positions and alignments of the wind turbine blade. A successful study of the interaction between rotor and tower (Zahle, Sorensen, & Johansen, 2009) emphasizes the importance of CFD in solving complex flow phenomena.

All these studies show that, even though CFD requires more resources for unsteady problems, it is cheaper than conducting full-scale or scaled wind turbine experimental analysis but yet provides sufficiently accurate results. By improving its capability to simulate widely separated flows through better turbulence modeling near the wall and in the flow field, CFD tools are becoming more and more accurate for the aerodynamic and aeroelasticity analysis of wind turbine blades.

Even though the final objective of the current study is to perform icing simulation on wind turbine blades, the characteristics of the flow field and the integrated loads of the clean blade are nevertheless required. To obtain these data, a grid study is performed to represent the flow field accurately with a minimum grid size. Three different grids, with 1.6M, 1.9 M, and 2.2M cells, are tested using the commercial CFD code at a pre-stall speed of 7m/s and the results compared with experimental data. Once the grid convergence analysis has been conducted, various two-equation turbulence models are tested to find the one that best fits the experimental data of NREL Phase VI blade. Thus, for each turbulence model, *standard k-ε*, *RNG k-ε*, *realizable k-ε*, and *SST k-ω* simulations are performed at a wind speed of 7 m/s, characterized by a reduced stall region on the rotor blade, to obtain pressure distributions and integrated aerodynamic loads on the blade. Results are compared with experimental data to find the most suitable turbulence model. Once

that model has been selected, new simulations are performed throughout the operational wind speed range of the wind turbine.

4.3 Methodology

4.3.1 Experimental Data

For this study, we selected one of the unsteady aerodynamics experiments (UAEs), the NREL Phase VI wind turbine, conducted by the National Renewable Energy Laboratory (NREL) in the NASA-Ames wind tunnel at Moffett Field, California, in 2000 (Simms, Schreck, Hand, & Fingersh, NREL). The NREL organized the data used in this paper. (Hand, Simms, & Fingersh, 2001) The advantage of using a wind tunnel of such gigantic proportions (24.4m by 36.6m, or 80 ft by 120 ft) to perform a full scale 10m diameter wind turbine test is that the blockage effect is not significant.

The general characteristics of the NREL Phase VI wind turbine are given in Table 4-1. The S809 airfoil is used for the entire blade. Linear chord and nonlinear twist distributions are shown in Figure 4-1. The blade root is completely circular up to 0.883 m, and, from this point up to 1.2573 m, the shape smoothly transforms from a circle into an airfoil configuration. The 3D CAD model of the blade was generated using the commercial software Rhinoceros 4.0. Figure 4-2shows the geometry.

From the experimental data, the upwind, 3° pitch, and non-yaw configurations were selected as validation data. The experimental parameters to be validated are the pressure coefficients at pressure tap locations (30%, 46.6%, 63.3%, 80%, and 95% span), the low-speed shaft torque, and the bending moment on the blade throughout the operational wind speed range. The experimental data are provided for a 30 second time period, and time-averaged data are used for the comparison.

For the selected data, the wind turbine rotation direction is counter-clockwise when viewed from upwind. The cone angle is 0◦. The rotor speed is 72 rpm, and the pitch angle is 3◦. The pitch angle is defined at 75% of the span, 0.75R, and the pitch axis is given as 30% of the chord, 0.3c.

4.3.2 Numerical Set-Up

Today, CFD tools, whether commercial or developed in-house, are routinely used for investigating the aerodynamics and fluid-structure interactions around numerous configurations. Of the commercial tools available, ANSYS FLUENT 12.0.16 is used in the current study. The package is a finite volume-based solver, which allows both structured and unstructured grids to discretize the computational domain. The software allows transient calculations as well as steady-state computations to be performed. Parallel computation capabilities are also offered to handle large meshes and to reach solutions in a reasonable time.

For this study, an incompressible, steady, Reynolds averaged Navier-Stokes (RANS) model is applied to solve the problem on a "rotating reference frame." The basic idea behind the rotating reference frame is the assumption that it is the flow field that rotates, and not the rotor, which means that an unsteady flow field turns into a steady flow with respect to the rotating reference frame. This approach simplifies the problem in terms of boundary conditions (no sliding mesh is required), computational cost, and post-processing results.

To reduce the complexity of the problem and the time spent on computational analysis, we made a number of hypotheses prior to numerical analysis. Initially, effects of the tower and the nacelle are ignored to reduce mesh size and the complexity of the problem. Although they may affect the performance and flow field of the rotor, they are neglected in many studies when they are not the focus of the research. Moreover, on the assumption that the flow field is 180° axisymmetric, one blade is modeled instead of two, and a "rotational periodic" boundary condition is applied, in order to reduce the computational cost. As explained above, since the blockage effect of the wind tunnel is minimal, the wind tunnel walls are not taken into account in the numerical domain. Finally, although the experimental data are time dependent, numerical analysis is conducted at steady state with the rotating reference frame model, which predicts time-averaged quantities. As a result, the time-averaged quantities of the experimental data and the numerical results can be compared.

Two-equation turbulence models have been widely used to simulate the flow field in engineering applications. As the name implies, these models have two independent transport equations, one for turbulent kinetic energy, and the other for turbulent dissipation or specific dissipation rate. Two equation models are complete, which means that no additional equations are needed to

model the turbulence, and that they both depend on the Boussinesq assumption (Wilcox, 1994). Details of turbulence models that are applied in this study are briefly explained below.

Standard k-ε Turbulence Model

The transport equations of the *k-ε* models are based on the turbulent kinetic energy, *k*, and the dissipation rate, *ε*. The simplest, the *standard k-ε* model, proposed by Launder and Spalding (1972), is based on the assumption that flow is fully turbulent. This model gives better results for fully turbulent flows. The transport equations for the *standard k-ε* model are as in Equations 4-1 and 4-2 :

$$\frac{\partial}{\partial x_i}(\rho k u_i) = \frac{\partial}{\partial x_j}\left[\left(\mu + \frac{\mu_t}{\sigma_k}\right)\frac{\partial k}{\partial x_j}\right] - \rho\overline{u_i' u_j'}\frac{\partial u_j}{\partial x_i} - \rho\varepsilon + S_k \qquad 4\text{-}1$$

$$\frac{\partial}{\partial x_i}(\rho \varepsilon u_i) = \frac{\partial}{\partial x_j}\left[\left(\mu + \frac{\mu_t}{\sigma_\varepsilon}\right)\frac{\partial \varepsilon}{\partial x_j}\right] - C_{1\varepsilon}\frac{\varepsilon}{k}\rho\overline{u_i' u_j'}\frac{\partial u_j}{\partial x_{ji}} - C_{2\varepsilon}\rho\frac{\varepsilon^2}{k} + S_\varepsilon \qquad 4\text{-}2$$

The turbulent viscosity is calculated using *k* and *ε* as in 4-3:

$$\mu_t = \rho C_\mu \frac{k^2}{\varepsilon} \qquad 4\text{-}3$$

The model coefficients, which are empirically determined, are given as in (Launder & Spalding, 1972):

$$C_{1\varepsilon} = 1.44 \qquad C_{2\varepsilon} = 1.92 \qquad C_\mu = 0.09 \quad \sigma_k = 1.0 \quad \sigma_\varepsilon = 1.3$$

RNG k-ε TurbulenceModel.

A more developed *k-ε* turbulence model, RNG *k-ε*, which is based on renormalization group theory (Yakhot & Orszag, 1986), has correction terms for swirling flow, low Reynolds number flow, and flow with high velocity gradients. The transport equations of the RNG *k-ε*

model are very similar to those of the standard k-ε model, except as shown in Equations 4-4 and 4-5:

$$\frac{\partial}{\partial x_i}(\rho k u_i) = \frac{\partial}{\partial x_j}\left[\alpha_k \mu_{eff} \frac{\partial k}{\partial x_j}\right] - \rho \overline{u_i' u_l'} \frac{\partial u_j}{\partial x_j} - \rho \varepsilon + S_k \tag{4-4}$$

$$\frac{\partial}{\partial x_i}(\rho \varepsilon u_i) = \frac{\partial}{\partial x_j}\left[\alpha_k \mu_{eff} \frac{\partial \varepsilon}{\partial x_j}\right] - C_{1\varepsilon}\frac{\varepsilon}{k}\rho \overline{u_i' u_l'} \frac{\partial u_j}{\partial x_j} - C_{2\varepsilon}^* \rho \frac{\varepsilon^2}{k} + S_\varepsilon \tag{4-5}$$

where;

$$C_{2\varepsilon}^* = C_{2\varepsilon} + \frac{C_\mu \eta^3 (1 - \frac{\eta}{\eta_0})}{1 + \beta \eta^3} \qquad \eta = S\frac{k}{\varepsilon} \quad \eta_0 = 4.38 \quad \beta = 0.012 \tag{4-6}$$

The model coefficients, which are derived analytically by RNG, are given as in (Yakhot & Orszag, 1986):

$$C_{1\varepsilon} = 1.42 \qquad C_{2\varepsilon} = 1.68$$

As can be seen from Equation 4-6, the coefficient of dissipation term $C_{2\varepsilon}^*$ is modified to provide better adaptability of the model to rapid strained flows. Moreover, the effective viscosity term μ_{eff} in both transport equations improves the model for low Reynolds numbers and near wall regions. For swirled flows, the *RNG k- ε* model of ANSYS FLUENT has an optional correction model that calculates turbulent viscosity as a function of swirl strength. For this study, the swirl correction is enabled as the flow field rotates.

Realizable k- ε turbulence model

The *realizable k- ε* model, proposed by Shis et al. (Shih, Liou, Shabbir, Yang, & Zhu, 1995),is a new turbulent viscosity model that accounts for rotation and strain in the flow. The transport equations of the model are in Equations 4-7 and 4-8:

$$\frac{\partial}{\partial x_i}(\rho k u_i) = \frac{\partial}{\partial x_j}\left[\left(\mu + \frac{\mu_t}{\sigma_k}\right)\frac{\partial k}{\partial x_j}\right] - \rho\overline{u_i'u_l'}\frac{\partial u_j}{\partial x_j} - \rho\varepsilon + S_k \qquad \text{4-7}$$

$$\frac{\partial}{\partial x_i}(\rho\varepsilon u_i) = \frac{\partial}{\partial x_j}\left[\left(\mu + \frac{\mu_t}{\sigma_k}\right)\frac{\varepsilon}{\partial x_j}\right] + \rho C_1 S_\varepsilon - \rho C_2 \frac{\varepsilon^2}{k+\sqrt{v\varepsilon}} - C_{1\varepsilon}\frac{\varepsilon}{k}\rho\overline{u_i'u_l'}\frac{\partial u_j}{\partial x_j} + S_\varepsilon \qquad \text{4-8}$$

where

$$C_1 = max\left[0.43, \frac{\eta}{\eta+5}\right] \quad \eta = S\frac{k}{\varepsilon} \quad S = \sqrt{2S_{ij}S_{ij}}$$

The *realizable k- ε* model is significantly different from other *k- ε* models, in that the turbulent viscosity coefficient C_μ depends on mean strain and rotation rates, turbulent kinetic energy, and energy dissipation, the use of which ANSYS FLUENT recommends for better prediction of the turbulent viscosity. The model coefficients of the *realizable k- ε* model are given as in (ANSYS, 2010):

$$C_{1\varepsilon} = 1.44 \quad C_2 = 1.9 \quad \sigma_k = 1.0 \quad \sigma_\varepsilon = 1.2$$

SST k- ω turbulence model

This model, which was presented by Menter (1994), is a combination of the *standard k-ω* model and the transformed *k-ε* model. It benefits from the advantages of both these turbulence models in different flow regions, activating the *standard k-ω* model near the wall and the *k-ε* model away from the surface. The *SST k- ω* model has been found to be more accurate than other turbulence models. The model transport equations are provided in Equations 4-94-10.

$$\frac{\partial}{\partial x_i}(\rho k u_i) = \frac{\partial}{\partial x_j}\left[\Gamma_k\frac{\partial k}{\partial x_j}\right] + \widetilde{G_k} - \rho\beta^*k\omega + S_k \qquad \text{4-9}$$

$$\frac{\partial}{\partial x_i}(\rho\omega u_i) = \frac{\partial}{\partial x_j}\left[\Gamma_\omega\frac{\partial\omega}{\partial x_j}\right] + \frac{\alpha}{v_t}\widetilde{G_k} - \rho\beta\omega^2 + 2(1-F_1)\rho\sigma_{\omega,2}\frac{1}{\omega}\frac{\partial k}{\partial x_j}\frac{\partial\omega}{\partial x_j} + S_\omega \qquad \text{4-10}$$

where the term $\widetilde{G_k}$ is

$$\widetilde{G_k} = \min\left(-\rho\overline{u_i'u_j'}\frac{\partial u_j}{\partial x_i}, 10\rho\beta^*k\omega\right)$$

The model coefficients are given as in (ANSYS, 2010):

$$\sigma_k = 1.176 \quad \sigma_\omega = 2.0$$

Computational Domain :

The geometries of the wind turbine and the domain for the numerical analysis are generated using RHINOCEROS (2014). Fig. 3 illustrates the computational domain. The inlet and outlet boundaries are placed at 3 times and 5 times the diameter from the wind turbine, respectively. Since an axisymmetric flow field is required for using the rotating reference frame and the rotational periodic boundary condition, a semi-cylindrical domain has been generated. To improve accuracy, a second small semi-cylindrical domain around the blade has also been generated, in order to refine the mesh in this region, as illustrated in Figure 4-3.

An unstructured mesh was chosen for the domain discretization. The surface mesh was generated using GAMBIT, formerly the companion software of FLUENT. For the surface mesh, the size functions of GAMBIT that enable the user to control the grid distribution over the surface were used. The number of nodes was maximized near the leading edge, where the large pressure gradients exist. "Meshed" size functions provided smooth transactions of mesh size from edges to face, whereas "curvature" size functions provided better representation of curved surfaces by keeping the mesh size to a minimum, as seen in Figure 4-4(a). To resolve the boundary layer, 20 prism layers normal-to-surface elements on the blade were generated. The initial height selected was 10^{-5} m, which guarantees $y_+ < 10$ on the blade surface. Three different grids with mesh sizes of 1.6 M, 1.9M, and 2.2M were used. The surface mesh and prism layer are shown in Figure 4-4(a) and (b), respectively.

Boundary Conditions

For the inlet boundary condition, the velocity normal to the inlet boundary and the turbulence intensity, which are provided by experimental data, were imposed. The outer

cylindrical domain is also treated as an inlet, and the same boundary conditions are applied. For the outflow boundary, the pressure outlet boundary condition is enforced by applying atmospheric pressure, as the flow is far from the wind turbine. For the inner surfaces, as explained above, rotational periodic boundary conditions are applied. Finally, the blade surface was treated as a no-slip wall boundary condition; that is, a zero velocity is imposed.

4.4 **Results**

In this section, results of the comparison of 3D numerical studies and the UAE data (Simms, Schreck, Hand, & Fingersh, NREL) are presented, starting with the results of the grid optimization study. To find the most convenient turbulence model, various two-equation turbulence models available in ANSYS FLUENT were applied, and the pressure coefficients were compared with the UAE data. The models that are available in the software are *standard k-ε*, *RNG k-ε*, *realizable k-ε*, *standard k-ω*, and *SST k-ω*. Initially, the results of these comparisons are presented for a 7 m/s wind speed and preselected spanwise locations, as explained in the Section 2. As will be shown below, the *k-ω SST* turbulence model fits the UAE data better, and so this model was selected for the rest of simulations at higher wind speeds. To further verify the numerical study, moments on the wind turbine blade, that is, low speed shaft torque and root flap moment, were compared. Finally, the numerical tool's ability to predict separated flow was shown by comparing pre-stall and stall velocity simulations.

4.4.1 Grid Convergence

To ensure the accuracy of the results and to keep the computational cost to a minimum, a basic grid convergence study was performed by generating three different grids: a coarse grid with 1.6M elements, a medium grid with 1.9M elements, and a fine grid with 2.2M elements. One noticeable difference between the grids is in the number of elements on the leading edge of the blade, as can be seen in Figure 4-5.

The computed results are compared against experimental data at three different spanwise locations: root, mid-span, and blade tip, as illustrated in Figure 4-6(a), (b), and (c), respectively. As shown, the coarse grid solution, represented by the cross-symbol, overpredicts the pressure coefficient for all spanwise locations, whereas medium and fine grids provide solutions that agree

well with the experimental data. After mid-chord, where the pressure gradients are relatively low, the coarse grid leads to a reasonable prediction of the pressure coefficient on the blade. In spite of the improved behavior in this region, it is clear that, globally, the coarse grid does not yield satisfactory results. In terms of the solutions obtained using medium and fine meshes, it can be seen that the pressure coefficient calculated with the fine mesh is only slightly better than that computed with the medium-sized grid. Because of this minor difference, we conclude that the medium-sized grid can be selected for the rest of the calculations while still keeping the computational cost relatively low.

4.4.2 Comparison of Turbulence Models.

The results obtained with the above-referenced turbulence models and medium sized grids are compared at 7m/s, which is the pre-stall, and therefore stable, region over the operational range. The pressure coefficient distribution over the chord is presented for three spanwise locations as root $0.3R$, mid-span $0.63R$, and tip $0.95R$. The pressure coefficient is obtained as in Equation 4-11, where W represents the wind speed, $r\Omega$ is the local rotational speed at that spanwise location, and c indicates the local chord. Comparison of the calculations obtained with the various turbulence models against experimental data are shown in Figure 4-7 (a)–(c).

$$C_p = \frac{P_\infty - P_0}{\frac{1}{2}\rho(W^2 + (r\Omega)^2)}$$

4-11

At first glance, with the exception of the *standard k-ε* model, all the turbulence models seem to predict the pressure coefficient well at the pressure side and at the suction side. The *standard k-ε* model overestimates the pressure at the leading edge.

At the root of the blade (a), where the rotational speed is relatively very low, the compatibility of all the turbulence models seems good. However, if the results are evaluated in detail at the leading edge and tip of the section, differences among the models become clearer. As seen in detail, the pressure coefficient predicted with the *SST k- ω* model is the best when compared with the experimental data, and the computed pressure coefficient is the worst when using the *standard k-ε* model.

At the mid-span location, the calculations with the *standard k-ε* model further deviate from the experimental data at the leading edge of the blade. The detailed comparisons of the pressure coefficients are shown at both the suction and pressure surfaces of the leading edge. The results of the other models are close at this location.

The ability of a turbulence model to accurately simulate flow becomes evident at the tip of the blade, where the rotational speed is the highest. As seen the predictions provided by the *SST k-ω* model are closer to the experimental data, and those obtained with the *standard k-ε* model deviates the most. Moreover, it is worth noting that the differences between the computations performed with the *realizable k-ε* and *RNG k-ε* models are very small, and these solutions appear to be the same. Although there is no separation at all at this location at 7 m/s, the prediction capability of all the turbulence models decreases visibly compared to that at the root and mid-span locations.

As a result, among the turbulence models, the best overall compatibility with experimental data is shown by the *SST k-ω* model for all spanwise locations. Similar conclusions have been drawn by Villalpando et al. (2012) (2011) who analyzed the flow over an NACA 63415 airfoil and showed that although all the turbulence models predict the lift, drag, and pressure coefficients well, the *k-ω SST* model provides a better estimate of the vortex shedding patterns of the flow.

4.4.3   Comparison of Moments on the Blade.

Using a medium sized grid and the *SST k- ω* model, a number of simulations were performed to predict the integrated loads on the rotor through the operational wind speed interval of the wind turbine at 7m/s, 10m/s, 15m/s, 20m/s, and 25 m/s. Moments on the blade, namely, low speed shaft torque (LSST) and root flap bending moment (RFBM), are compared against UAE data over the operational wind speeds, as shown in Figure 4-8(a) and (b). Figure 4-8(a) reveals that the numerical study underpredicts the LSST by up to 20% compared with the UAE data, except at the 10 m/s stall speed, where the LSST is underpredicted by about 40%. In spite of the large deviation, numerical torque exhibits the same trend as the UAE data. The rather poor compatibility of the LSST data is attributed to the drag, that is, the dominant contribution to the LSST, especially at low wind speeds and for low CFD prediction capability for widely separated

flows, as mentioned in Section 1. In contrast to LSST, RFBM comparison shows fairly good compatibility with the UAE data, as shown in Figure 4-8(b).

Streamlines over the blade and the velocity field at spanwise locations 0.3R, 0.466R, 0.633R, 0.8R, and 0.95R are given for 10m/s in Figure 4-9, which shows that the flow is widely separated at mid-board locations. Separation over the blade affects the accuracy of the prediction of forces adversely, as mentioned above. Comparison of the pressure coefficients against experimental data at 10m/s is shown in Figure 4-10(a)–(e). It can be seen that the pressure coefficients are not as well predicted as in the 7m/s test case. The effect of separation can be clearly seen at the suction surfaces 0.466R, 0.633R, and 0.8R, where there are separation bubbles. In fact, at each spanwise location, prediction of the pressure coefficient at the suction side is less accurate than that obtained on the pressure side.

4.5   Concluding Remarks

Performance of the NREL Phase VI experimental wind turbine rotor has been simulated using the commercial CFD tool ANSYS FLUENT. The simulation conditions selected were an upwind turbine configuration with 0° yaw and 3° pitch alignment. For the simulations, a rotating reference frame model is used. A grid with 1.9 million elements was selected through a grid optimization study. For handling turbulence, the two-equation models available in ANSYS FLUENT were used for 7 m/s, and the *k-ω SST* model was found to be the most appropriate.

The resultant moments obtained through the operational wind speed range (7m/s, 10m/s, 15m/s, 20m/s, and 25m/s) were compared against experimental data. The comparison of moments shows good agreement, especially for the RFBM. Although the LSST results deviate from the experimental data in the 20% range, the trend similar to that of the experimental data. Comparisons of pressure coefficients for stall speed (10m/s) were presented for five different spanwise locations. The adverse effects of separation on prediction capability have been shown. However, as mentioned above, the capability of the CFD method to simulate highly separated flows remains poor. Moreover, the major deviation from the experimental data for the leading edge, caused by the large pressure gradients, is a problem that can be addressed by increasing the grid density in this region.

Although the current results can only be seen as preliminary, the flow field data and the velocity and pressure distributions obtained will serve as initial data for the multiphase analysis of air and water that is required for icing simulation. In a subsequent work, calculations at various wind speeds will be conducted on an iced wind turbine blade, and the performance of the blade will be compared with that of the clean blade presented in this study.

4.6 **Acknowledgment**
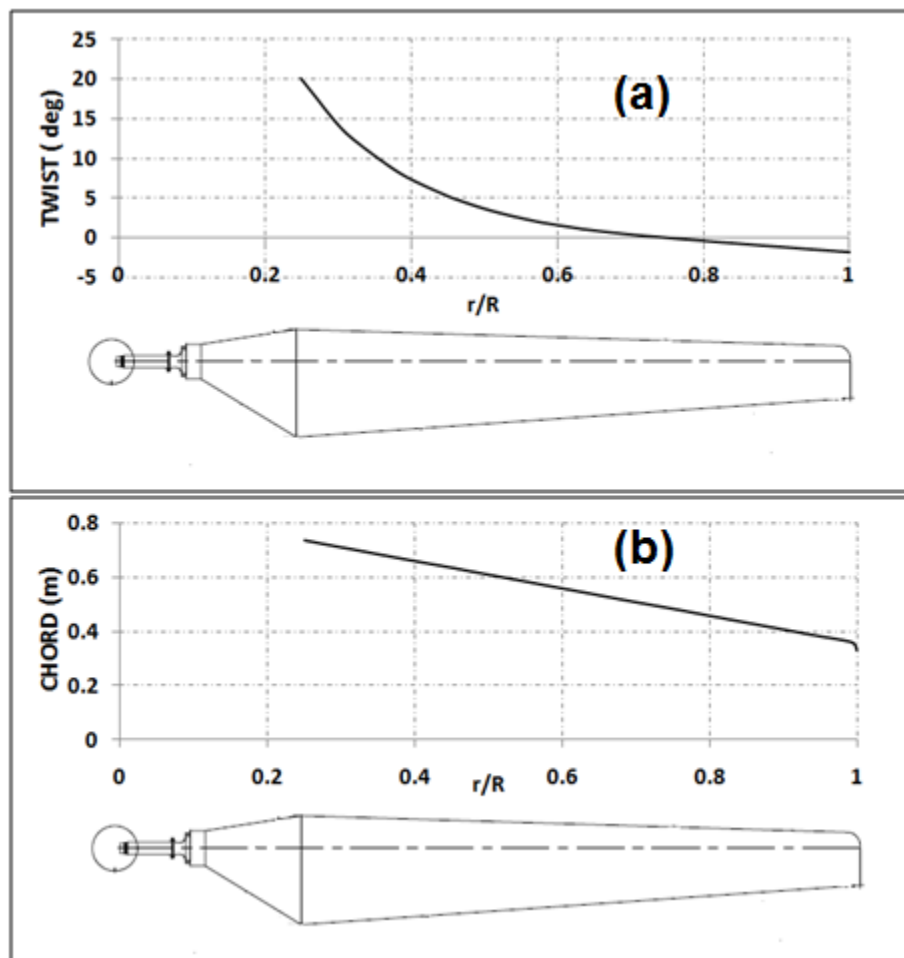
Figure 4-1(a) Twist distribution; (b) chord distribution of NREL Phase VI blade.
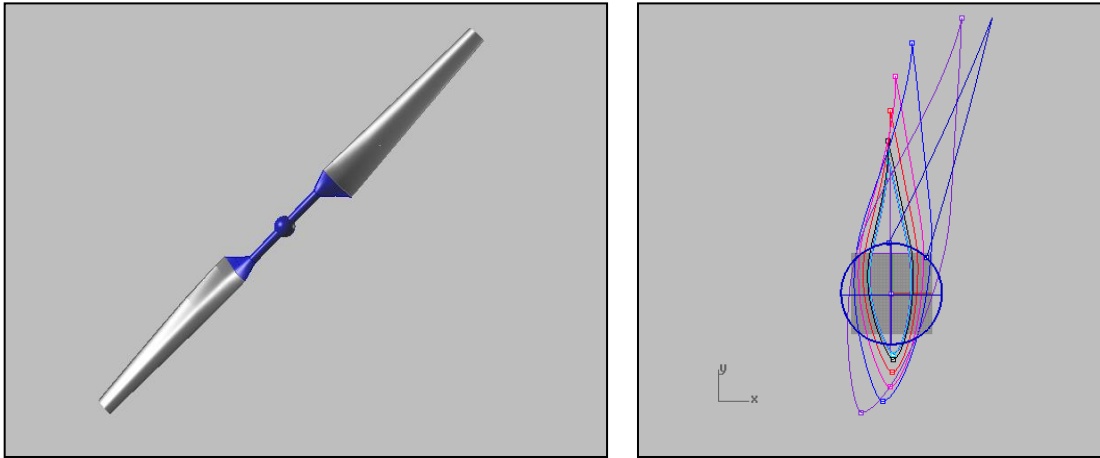
Figure 4-2 3D CAD model of the NREL phase VI wind turbine.
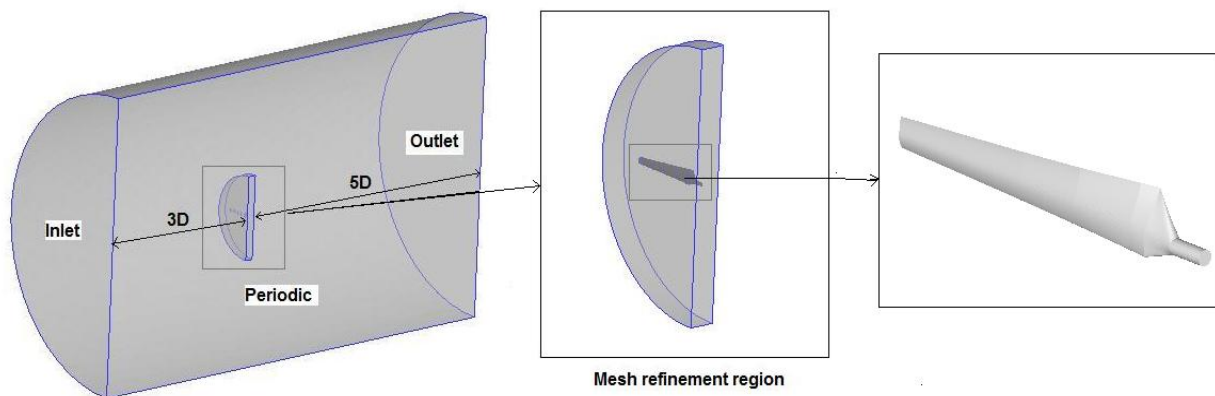
Figure 4-3 Computational domain for the NREL Phase VI rotor
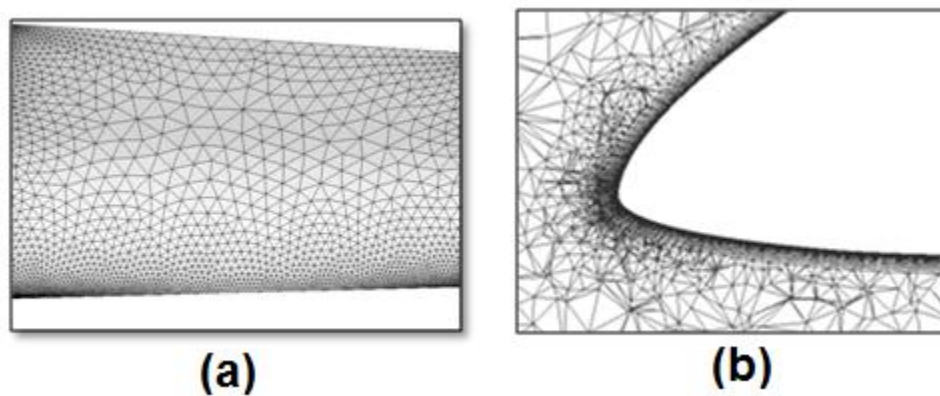
Figure 4-4 (a) Surface triangular mesh, (b) domain tetrahedral and prism mesh.
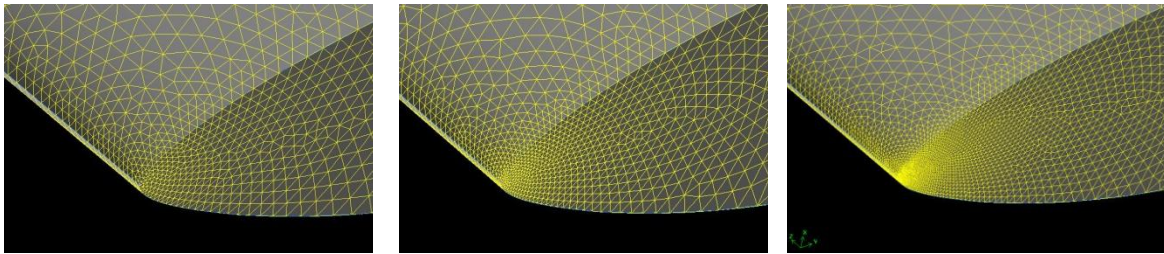
Figure 4-5 Surface mesh on the tip of the blade for a coarse, amedium, and a fine grid.
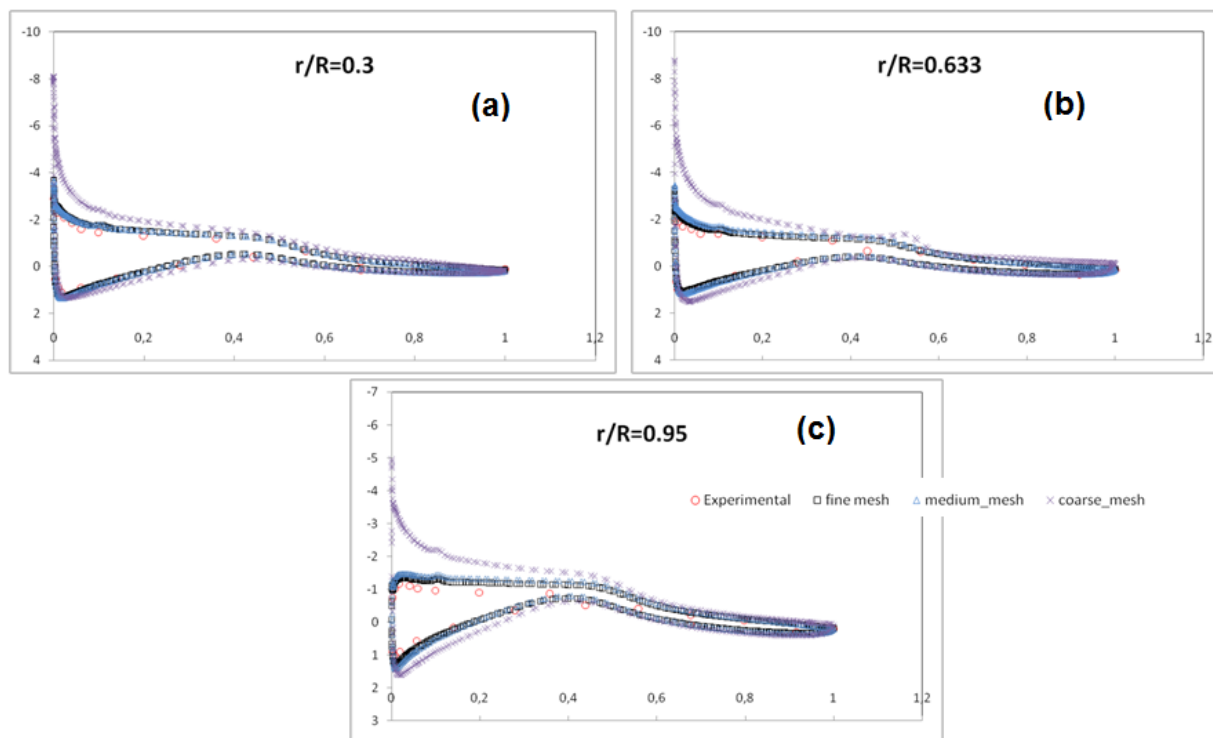
Figure 4-6 Pressure coefficient comparison for various grid sizes for: a) root; b) mid-span; and c) blade tip.
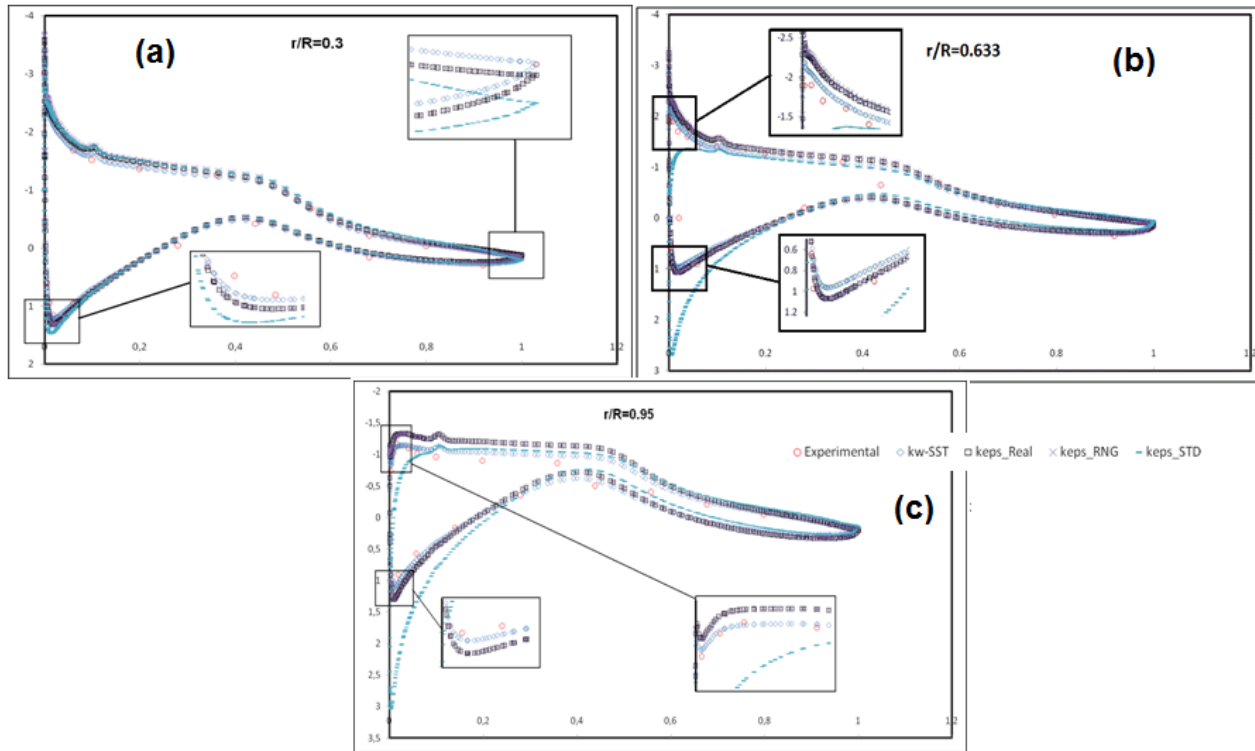
Figure 4-7 Comparison of pressure coefficients for various turbulence models against experimental data for: a) root; b) mid-span; and c) blade tip
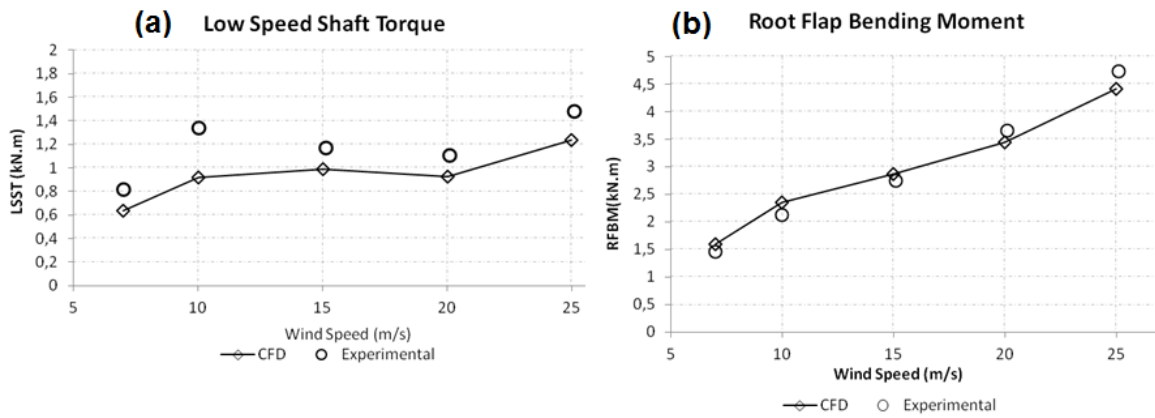
Figure 4-8 Comparison of experimental data and CFD results for (a) low-speed shaft torque; (b) root flap bending moment.
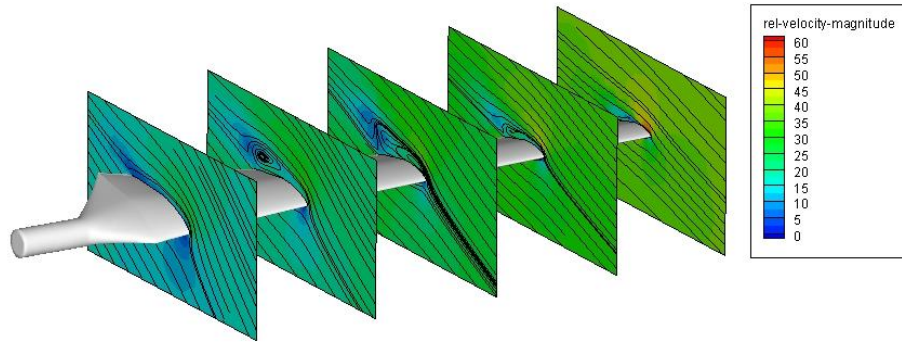
Figure 4-9 Streamlines over the blade and relative velocity distribution at 0.3R, 0.466R, 0.633R, 0.8R, and 0.95R.
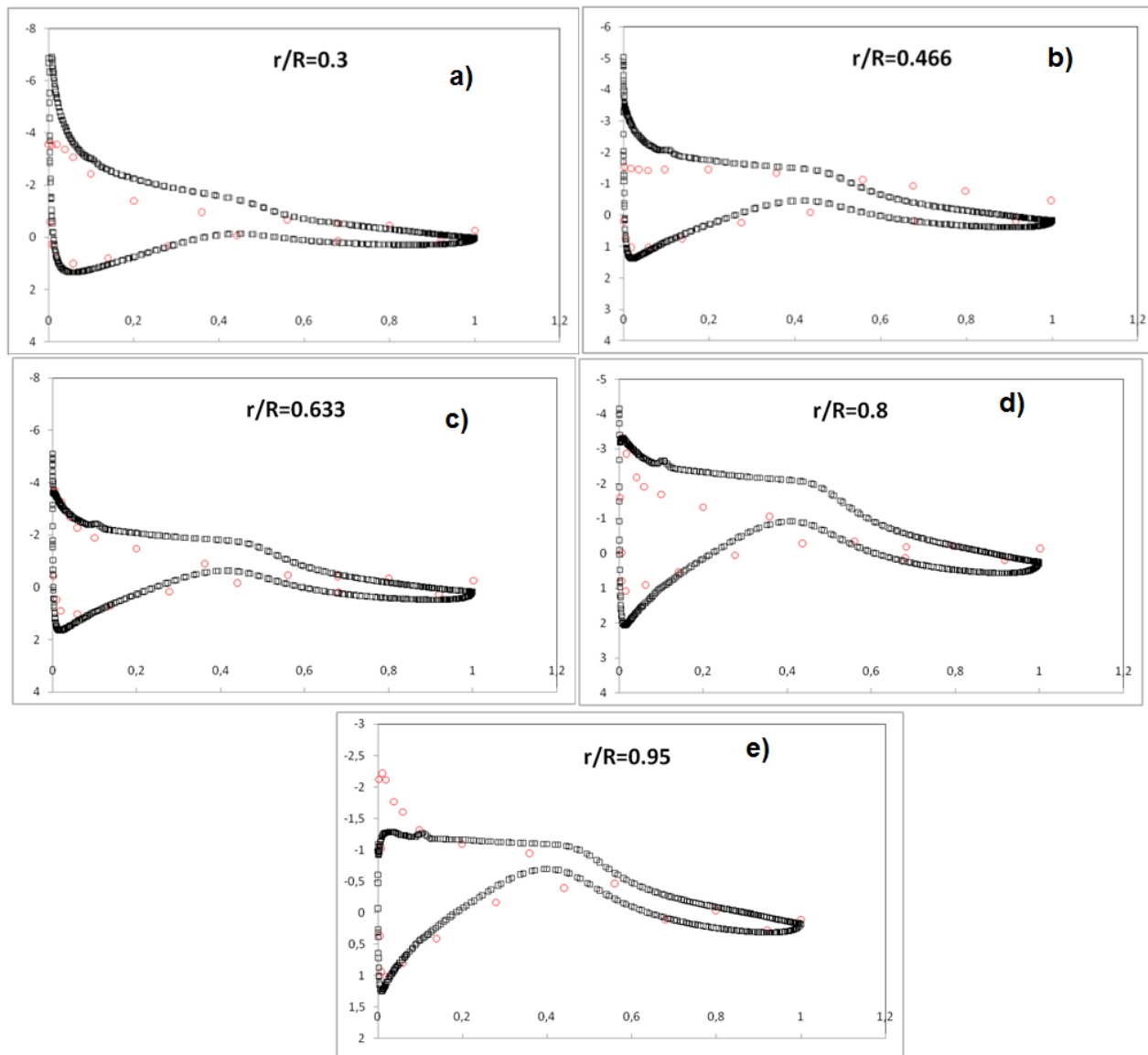
Figure 4-10 Pressure coefficient comparison at stall speed, 10m/s, for: (a) 0.3R, (b) 0.466R, (c) 0.633R, (d) 0.8R, and (e) 0.95R.

Table 4-1 NREL phase VI experimental wind turbine characteristics

Number of blades	2
Diameter	5.029 m
Airfoil	S809
Root chord	0.7366 m
Tip chord	0.3808 m
Root twist	21.8^o
Tip twist	-1.775^o
Rotational Speed	72 rpm

Chapter 5   ARTICLE 3: COMPARISON OF THE QUASI-3D AND FULLY 3D METHODS FOR MODELING WIND TURBINE ICING

Ece Sagol[1*], Marcelo Reggio[1], Adrian Ilinca[2]

1 Polytechnique Montréal, 2500 Chemin de Polytechnique, H3T 1J4, Montréal, Québec, Canada

2 Université du Québec à Rimouski (UQAR), 300, allée des Ursulines, G5L 3A1 Rimouski (Québec) Canada

5.1 Abstract

Wind turbine icing reduces power output and may even cause the machine to stop. Numerical models with various levels of accuracy and complexity are frequently used to assess icing effects and predict potential energy loss, as well as to assess risks to the equipment. These studies mainly address the accuracy of the computed ice shape using a 2D approach, or qualitatively evaluate 3D methods, as there are no experimental data available for proper validation. However, before choosing one of these methods, practitioners must gauge the accuracy of the prediction, as well as the computational cost of the method. The objective of this research is to compare two methods for the prediction of ice shape and the corresponding rotor performance. The first tool, a Quasi-3D method, computes the ice shape on 2D sections and integrates the forces involved to compute the power of the machine. The second tool, a Fully 3D method, treats the blade as a whole. To compute the flow field characteristics for both single and multiphase flows, a commercial Computational Fluid Dynamics (CFD) tool and in-house code are used. Comparison of the results shows that the two methods yield different ice shapes and different rotor performance. The computational cost of the Fully 3D method is, as expected, much higher than that of the Quasi-3D method. Nevertheless, the Fully 3D method is found to be more accurate when validating against experimental data for the power generated with blades under a no-icing condition.

5.2 Introduction

Ice accretion on wind turbine blades is an impediment to efficient operation in a number of ways, such as reduction in power output, risk of ice shedding during operation, and excessive loading of

the blades (Dalili, A., & Carriveau, 2009). The magnitude of these problems is proportional to the severity of the ice accretion. For instance, the lightest icing conditions result in a roughened surface, which is sufficient to bring about an early laminar-to-turbulent transition of the boundary layer (Schlichting, 1979) (Busch, 2009) (Turner, Hubbe-Walker, & Bayley, 2000) (Kerho & Bragg, 1997) (Bragg, Broeren, & Blumenthal, 2005). Moreover, for fully rough regime, the frictional drag is a function of the roughness, and pressure distribution over the airfoil is also affected by the boundary layer displacement effect developed by the surface roughness. These in turn diminish the aerodynamic performance of the blade, i.e. the lift coefficient decrease and the drag coefficient increases (Hochart, Fortin, Perron, & Ilinca, 2008) (Khalfallah & Kolub, 2007). Under heavy icing conditions, not only is the energy yield decreased as a consequence of a distorted aerodynamic profile, but mechanical problems, like overloading, unbalancing, and vibration, can occur (Illinca, 2011) (Parent & Ilinca, 2011). In cases of severe icing, the turbines stop completely most of the time. This is why yearly energy loss may be as high as 20% of the expected Annual Energy Production (AEP) in regions that experience harsh winter conditions (Botta, Cavaliere, & Holttinten, 1998). The effect on rotor mechanics of excessive ice build-up is also significant. Although it is not investigated thoroughly, it is assumed that this excessive and persistent ice build-up shortens the life of the blades due to metal fatigue and increases the vibration risk due to its asymmetric distribution. Finally, as ice chunks may be thrown from the blades during rotation, there is a risk to residential areas, public roads, power lines, and other installations located near wind turbines that must be addressed.

Ice is formed when supercooled water droplets hit a surface and freeze. The ice formations that occur most frequently on wind turbines are glaze ice and rime ice. Glaze ice has a horn-like shape and consists of a thick ice layer covered by a thinner water layer. This characteristic shape originates from the runback water that does not freeze on impact, but does so later on, as it moves towards the trailing edge of a blade. Rime ice, or streamwise ice, by contrast, consists of ice layers that have frozen on impact, where the trajectory of the water droplet meets the surface of a blade. Rime ice has a less negative effect on performance, whereas glaze ice, because of its shape, has a more pronounced negative effect. In this study, only rime ice accretion on a wind turbine blade is considered.

In an attempt to predict the risks associated with ice accretion and to mitigate them, numerical algorithms can be used to simulate energy losses and provide the necessary data for vibration and

aeroelastic analyses. In the literature, the power output of a wind turbine is computed using various numerical tools, such as Blade Element Momentum, Vortex Lattice, and Computational Fluid Dynamics (CFD) solvers. The most popular of these is the Blade Element Momentum (BEM) method, which determines the blade power by integrating the forces on 2D blade sections for which the aerodynamic characteristics are known. This method is extensively used in the literature thanks to its reasonable accuracy, low computational cost, and easy modeling characteristics (Sorensen, N. N.; Michelsen, J. A.; Schreck, S., 2002) (Johansen & Sorensen, 2004) (Hansen, Sorensen, Voutsinas, Sorensen, & Madsen, 2006). Although the BEM method provides a good base for the initial design, more sophisticated models are needed to improve accuracy and capture flow field information. The 3D CFD solver is more accurate, and is extensively used, as computational costs are steadily diminishing. CFD solvers have been used in numerous studies on wind turbine blades to address various issues, involving performance (power curve), aerodynamics, fluid-structure interaction, acoustics, and icing analysis, for example (Sagol, Reggio, & Ilinca, 2012) (Ramdenee, Minea, & Ilinca, 2011) . A comparison of these methods on various applications has shown that they all perform well for pre-stall regimes. In spite of a certain level of error, these solvers predict power yield more accurately for stall and post stall regimes than the others. (Duque, Johnson, van Dam, Cortes, & Yee, 2000) (Laursen, Enevoldsen, & Hijort, 2007) In fact, all these studies conclude that CFD provides realistic results, even though more computational resources are required, and is much cheaper than conducting full scale or scaled wind turbine experiments.

In this study, we compute the ice shape under given atmospheric conditions using a multiphase flow model, which simulates a flow field made up of air and super-cooled water droplets. Our objective is to determine the rate of accumulation of water droplets, or collection efficiency, on the blade surface. In the literature, two types of multiphase models are available: Lagrangian (Martini, Ramdenee, Ibrahim, & Ilinca, 2011) (2011) and Eulerian (Bourgault, Habashi, Dompierre, & Baruzzi, 1999) (Honsek, Habashi, & Aube, 2008) (Wirogo & Srirambhatla, 2002). The former computes the trajectory of the each water particle present in the airflow, whereas the latter treats the water phase as a continuum. Selection and justification of the model are discussed in the methodology section.

The main objective of this research is to establish a methodology that predicts annual energy losses due to wind turbine icing. We also study the generation and use of the numerical tools that

offer the best compromise between accuracy and computational cost. In other words, the methodology is developed in such a way that every parameter (mesh size, turbulence model, and multiphase analysis type) is optimized to maximize the former and minimize the latter. A previous work focused on the computation and validation of clean blade performance in a 3D domain, showing that, of the two-equation turbulence models studied, the k-ω SST model, generates the most accurate results. The same conclusion has been drawn in many other studies addressing similar rotating machines (Benjanirat, Sankar, & Xu, 2003) (Villalpando, Reggio, & Ilinca, 2011) . A more recent study, Chapter 3, devoted to roughness effects on wind turbines blades, concluded that any kind of precipitation affects performance, even in its early stages, by spoiling the aerodynamic field. Based on that result, we take into account roughness effects in our numerical simulations in our study here.

We use two computational approaches in this paper to calculate rime ice shape and the corresponding power loss suffered by a wind turbine. In the first method, Quasi-3D, the collection efficiency and ice accretion shape in a 2D domain are calculated, and the power curve is determined using the BEM method. A multiphase analysis is performed using the Eulerian approach, and the aerodynamic coefficients required for the BEM method are derived from single phase CFD simulations on the iced blade sections. In the second method, Fully 3D, all the calculations (multiphase flow, ice accretion shape, and power output) are performed in a 3D domain. The purpose of the comparison is to determine whether or not the additional computer resources required for the simulations in the Fully 3D method are justified by the improvement in the accuracy of the results. Details of these two methods are provided in the methodology section. In the results section, the two methods are compared in terms of computational cost, ice accretion shape, and wind turbine power output.

5.3 **Methodology**

The procedure followed for computing ice shape and the associated performance loss is illustrated in Figure 5-1. This scheme applies to both the Quasi-3D and Fully 3D methods, which are explained in detail below. Note that the shaded blocks only apply to the former method. The blade shape characteristics and the atmospheric conditions are provided to the system as inputs, and both methods yield ice shape and power reduction due to icing as outputs.

5.3.1 Quasi-3D (Q3D) Method

Q3D does not treat the blade as a whole, but as a number of independent 2D sections. Initially, the blade is divided into a number of sections on which the analyses are carried out. This number varies, and is chosen to minimize computational cost and maximize accuracy. This parameter and the resulting section size strongly depend on the geometric characteristics of the blade, such as twist, taper, and radius. As the complexity of the blade geometry increases, the number of blade sections increases as well. For the NREL VI blade, the optimum number of elements has, by trial and error, been computed as 8. These sections are illustrated in Figure 5-2.

The clean blade power (Stage 1) is computed using in-house code based on the BEM method. This method, proposed by Glauert (Leishman, 2002), formulates forces and moments on a blade section using lift and drag coefficients, and integrates those forces to compute the torque, thrust, and power of the machine. The precision of the BEM model strongly depends on the lift and drag coefficients of the airfoils used as inputs for each section. However, because of its the nature, this method fails to take into account the 3D characteristics of the flow field, since it treats each section independently. The formulation and details of this model are available in many studies (Leishman, 2002) (Buhl, 2005). Here, some empirical correlations, which account for tip and hub correction losses, are included to improve the accuracy of the model. Moreover, the lift and drag coefficients that are required for the BEM code are derived by performing CFD analyses for various angles of attack: from -25° to 25°. Angles beyond this range are extrapolated using the Viterna method (Hansen C.). The key factor that influences the ice shape on a surface is the collection efficiency, which is the ability of the surface to catch water droplets. To calculate this parameter, the equation of motion must be solved for air as well as water droplets, as the air affects the trajectory of water particles. This problem can be addressed by performing a multiphase analysis (Stage 2), where the air and water phases are simulated within the same flow. There are two types of multiphase modeling methods available in the literature: Eulerian and Lagrangian. Both these models have been proven to be efficient for certain types of problems. Comparison of these methods for an icing analysis shows that simple 2D geometries can be simulated precisely using both the Lagrangian and Eulerian methods; however, the Lagrangian method is more cost-effective in 2D cases (Silveria, Maliska, Estivam, & Mendes, 2003). Nevertheless, there are problems with this method for complex 3D cases, which are related to the releasing location of the water droplets and velocity interpolation. Moreover, it is

computationally more expensive to calculate the trajectories of each droplet in a 3D domain. The Eulerian method, by contrast, yields accurate computations for complex bodies in 3D domains. One drawback of the Eulerian method is that it can only perform multiphase simulations for one size of droplet, while the Lagrangian method can model various droplet sizes. Fortunately, this drawback does not affect our application, as droplet size is usually defined in terms of Median Volume Diameter (MVD), which is a representative value for a droplet of average size. The Eulerian method is used for this study, as the nature of the **F3D** method requires it. In the Eulerian model, the governing equations are solved for each phase. We have made some assumptions in this study; for example, splashing, bouncing, and collision mechanisms are ignored, and droplets are considered to be spherical, so that a proper drag function can be used.

Multiphase analysis is performed using a commercial CFD code, ANSYS FLUENT, for both the **Q3D** and **F3D** methods. Collection efficiency, β, is computed using the Equation 5-1 :

$$\beta = \alpha_{nw} \frac{(V_w n)}{V_r}$$

5-1

Here, α_{nw} is the normalized volume fraction of water, V_w is the local water droplet velocity, n is the normal vector of the surface cell, and V_r is the reference wind speed.

The ice shape is computed (Stage 3) using heat transfer equations adapted to icing on a surface, as proposed by Myers (2001). This model, called the "extended Messinger method", computes ice growth as a function of the temperatures and thermal conductivities of the ice and water phases, and of atmospheric conditions. In the case of rime ice, water droplets freeze as soon as they hit the surface. Consequently, neglecting water layer thickness, rime ice thickness is given by:

$$B = \beta V_r \frac{(LWC)\, t}{\rho_r}$$

5-2

Here, B is the ice thickness on a cell, β is the collection efficiency, LWC is the liquid water content of the air, ρ_r is the rime ice density, and t is the icing period.

The final ice shape on a blade is significantly dependent on the collection efficiency distribution on the surface. However, as the shape of the surface changes during ice accretion, the collection

efficiency distribution also changes. For this reason, instead of computing the ice growth at one time, the icing period is divided into time intervals, in which the multiphase analysis is repeated for better accuracy. This parameter is converged, by trial and error, to an optimal value to keep the computational cost to a minimum. After the final ice shape is obtained, the lift and drag coefficients of the iced sections are computed using CFD with the k-ω SST turbulence model. Since icing results in roughness variation, we smoothed the physical surface, as any irregularities would result in complications in terms of mesh generation and numerical convergence. Instead, the average height of roughness elements was computed and included in the numerical scheme, as these elements affect the nature of the flow field. Details of the capability of the numerical algorithm to simulate roughness are explained in Chapter 3. Finally, the power generated by the iced blade is obtained with the BEM code and compared to that generated by a clean blade.

5.3.2 Fully 3D (F3D) Method

In **F3D**, the scheme depicted in Figure 5-1, with the exception of the shaded blocks, is followed. For better accuracy, all the analyses (performance, multiphase, and ice accretion) are performed in a 3D domain. As the objective of the research is to propose a feasible 3D method, some assumptions and simplifying paths are suggested that decrease the complexity of the problem and the computational cost involved. Initially, the flow field is considered axisymmetric, so that only one blade is simulated, using a periodic boundary condition. We adopt a rotating reference frame approach, which is based on the rotation of the flow field in the opposite direction of the rotation of the blades. This approach simplifies the problem in terms of boundary conditions (no sliding mesh is required), computational cost, and post-processing of the results. For the ice shape computations, a multiphase simulation is initially performed in 3D, followed by computation of ice thickness on the surface at each node. As previously mentioned, the total icing time is divided into smaller time intervals for accurate prediction of collection efficiency. Moreover, a roughness level is assigned based on the average deviation in the ice thickness. Finally, the iced blade performance is analyzed with ANSYS FLUENT with the exactly same settings as for clean blade analysis. However, a higher mesh density is required, in order to capture the complexity of the iced blade surface.

5.3.3 Test Case

For this study, we selected the NREL (National Renewable Energy Laboratory) Phase VI wind turbine as a test case, because of the quality of the data, which is well recognized in the research community. Wind tunnel test conditions are better suited for a numerical validation, as they are steadier than those in real world wind farm settings. The wind tunnel experiments were performed by the NREL in the NASA-Ames wind tunnel at Moffett Field, California, in 2000 (Hand, Simms, & Fingersh, 2001) (Simms, Schreck, Hand, & Fingersh, NREL). The general characteristics of the NREL Phase VI wind turbine are given in Table 1. The S809 airfoil is used for the entire blade. Linear chord and nonlinear twist distributions are shown in Figure 5-3. The blade root is completely circular up to 0.883 m, and, from this point up to 1.2573 m, the shape smoothly transforms from a circle into an airfoil configuration.

5.3.4 Numerical Scheme and Mesh Characteristics

Incompressible Reynolds-Averaged Navier-Stokes (RANS) equations, along with the SIMPLE (Semi-Implicit Method for Pressure-Linked Equations) coupling, are used in ANSYS FLUENT. For the 2D simulations, an inflow angle and velocity are computed for each section. The 3D analysis does not require such inputs, as the rotation is applied to the system using the "rotating reference frame" model available in the algorithm. To further reduce the complexity of the problem, and consequently the time spent on computational analysis, the presence of the tower and the nacelle are ignored, as they are not the focus of this research and their physical impact is limited. Finally, only one blade is modeled, assuming that the flow field is 180∘ axisymmetric, and a 'rotational periodic' boundary condition is applied to the problem. The computational domains of 2D and 3D analyses that correspond to the **Q3D** and **F3D** methods are shown in Figure 5-4. An inner domain is generated to increase the mesh density around the blade in the 3D domain.

For both domains, hybrid meshing is preferred. The 2D domain includes rectangular and triangular elements, while the 3D space comprises triangular prism and tetrahedral elements. The rectangular elements and the triangular prism elements are used around the airfoil and the blade for better resolution of the boundary layer on the surface. Twenty prism layers, with an initial

height of 1e-5 m, are generated for both domains, and a mesh convergence study is performed for both domains. The 2D domain has a total 0.05 million (50,000) nodes, and the 3D domain has 5.5 million nodes.

5.4 Results

First, the results of the clean blade studies for **Q3D** and **F3D** are presented and compared. The icing analyses are performed for a wind speed of 7 m/s, 60 minutes of ice accretion, and an average particle size (MVD) of $20*10^{-6}$ m. A liquid water content of 1 g/m^3 and ambient temperature of -15° C are selected for rime icing conditions. The ice shapes on various sections, the machine power, and the sectional forces are compared. Finally, the computational costs of the two methods are discussed.

5.4.1 Clean Blade Analysis

For **Q3D**, the lift and the drag coefficients of the clean section are computed with CFD analysis prior to driving the BEM code. The resulting aerodynamic coefficients of the clean sections are shown in Figure 5-5: the lift coefficient increases from the root to the tip of the blade, whereas the drag coefficient does not change significantly. This implies that most of the performance of the blade is produced near the tip, as a result of local relative wind speed that increases owing to rotation.

The sectional torque of the clean blade is shown in Figure 5-6. The experimental data at 7 m/s indicate a torque of around 800 N.m. The 3D computation yields a total torque of 700 N.m, while the BEM method results in a 590 N.m torque. In spite of a 12% deviation from experimental data, the 3D computation still predicts more accurate results than the 2D computation with a 25% deviation. A close inspection of the results reveals that the BEM method can also predict the torque and the CFD at the root section of the blade. However, towards the tip, the BEM method computes less torque, which may be because the 3D characteristics of the flow were not taken into account.

5.4.2 Blade Icing Analysis

The ice shapes, computed with both methods during 60 minutes of ice accretion in three ice layers, are compared to a clean profile in Figure 5-7. Each profile is normalized and rotated to 0° of pitch for better comparison. Only the leading edge sections are presented, as there is no significant ice accretion on the other parts of the airfoil. Figure 5-7 reveals some of the characteristics of ice accretion on the blades accounted for by both **Q3D** and **F3D**. To begin with, the volume of ice accretion increases from the root to the tip of the blade (Sections 1 to 8). On Section 1, almost no ice has accreted on the airfoil. This is an obvious result of low local relative wind speed at the root section, which results in low water droplet velocity, which in turn has a direct effect on collection efficiency. The second characteristic is that relatively more ice is accreted on the pressure (lower) surface. **Q3D** predicts a larger quantity of ice on the pressure side, whereas almost no ice has accreted on the suction side. For the **F3D** alternative, ice has accreted more on the pressure side, closer to the hub, and becomes more balanced between the pressure side and the suction side moving towards the tip. This characteristic stems from the incoming angle of the water droplets, which dictates the direction of growth. Based on this characteristic, for **Q3D** analysis, the angle of attack increases continuously from the root to the tip of the blade.

The sectional torque for clean and iced blades for **Q3D** and **F3D** are compared in Figure 5-8 (a) and (b), respectively. The **Q3D** analysis predicts a power loss of 40%, whereas **F3D** predicts a 25% power loss. This result was expected, as the ice accretion on the blade is greater when computed with **Q3D**. Moreover, as most of the accreted ice is on the pressure side of the leading edge, a separation bubble, which causes an increase in power loss, is observed for some sections. Finally, it is worth noting that the power loss is greater at the tip of the blade, where more ice has accumulated.

We also measured the computational time for both methods. As explained before, the total ice accretion time, 60 minutes, is divided into three equal periods of 20 minutes, which are called layers, and ice shape is calculated within these periods. Figure 5-9 illustrates the time spent to compute each layer of ice for each section and for the entire blade. This computation time includes meshing, single phase and multiphase CFD analysis, BEM analysis for **Q3D**, smoothing of the iced profile and the blade, and ice shape computation. All these analyses, except the

smoothing process, are performed automatically with an in-house MATLAB code, which covers all the processes in Figure 5-1. Performance of the smoothing analysis within the algorithm is not a very complex task, however it must be done manually in some cases.

In **Q3D**, less time is required to compute the root section, as the profile is smoother there and the corresponding flow field is less complex. Towards the tip section, the time required increases after the first ice layer has been computed. This is because no intervention is needed during the process for the first layer of each of the sections. The task that increases the computational time is the intervention required for smoothing and controlling the multiphase analysis, the convergence of which is very sensitive. When the process is fully automated, the total computational time decreases significantly.

It is obvious that **F3D** takes substantially longer than **Q3D**, more than 10 times longer in fact. In return, we can expect the results to be more accurate than 2D calculations. We could not validate our results for the iced blade, as there are no experimental data available in the literature. However, based on the clean blade results in Figure 5-6, we can reasonably conclude that **F3D** yields more accurate results, and that **Q3D** can only approach these results at sections near the hub of the blade. As with **F3D**, as ice accretes, the computational time also increases slightly.

5.5 **Conclusion**

This paper presents a comparison of icing computations on a wind turbine using two different methods, Quasi-3D and Fully 3D, with similar physical modeling. The clean blade performance, ice shape, iced blade performance, flow fields, and computational costs are analyzed and compared. The results of the two methods are validated against experimental results for the power output of a clean blade. Based on these results, the Fully 3D method yields more accurate results for the clean blade. For the iced blade, validation was not possible owing to the lack of experimental results. However, the two methods yield quite different results for ice shape and performance. This difference occurs mainly because different flow patterns are produced by different ice shapes at different locations on the blade, especially in separation regions. We can conclude that, even though the computational cost of applying Fully 3D is much higher, icing analyses in 2D may lack accuracy, because the ice shapes and associated power losses are overestimated owing to absence of the 3D characteristics of rotational flow. A possible solution

to further decrease the computational cost of the Fully 3D method might be to compute the ice shapes on 2D sections once the collection efficiency and flow field features from a 3D multiphase analysis have been derived. This could be a topic for a future study.

5.6 **Acknowledgements**
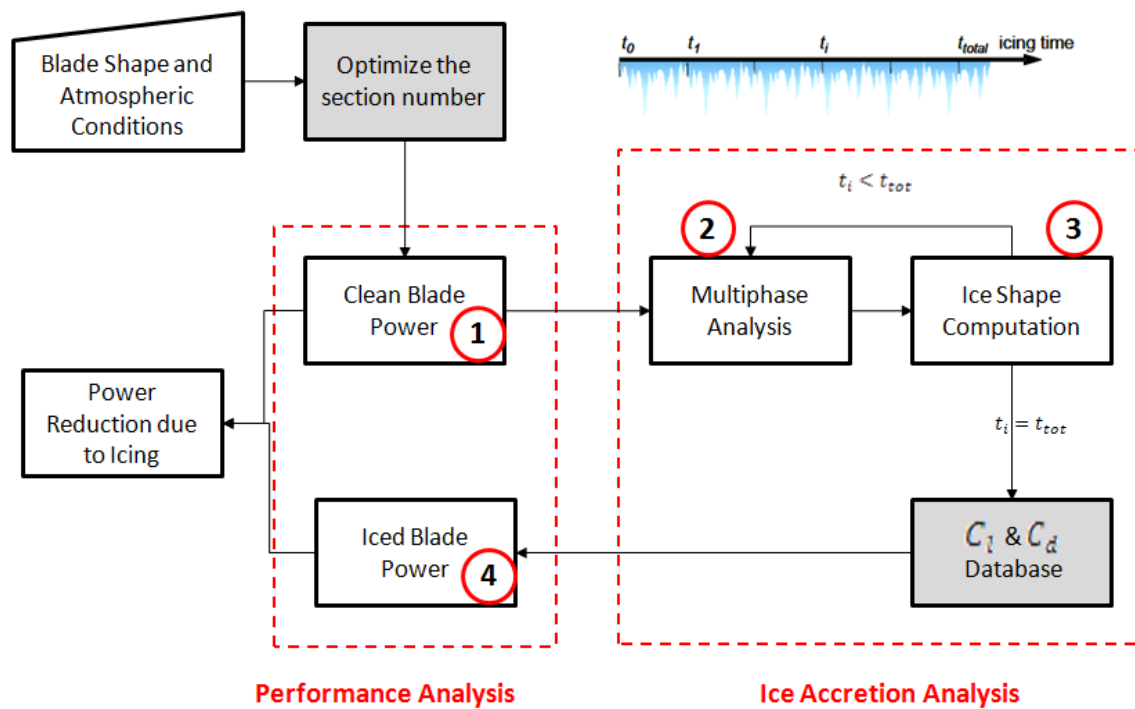
Figure 5-1 Flowchart of ice accretion and performance modeling.
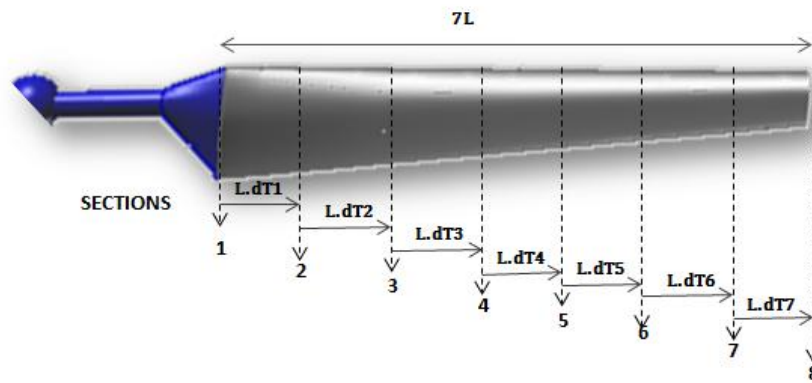
Figure 5-2 Blade sections for the Q3D method.
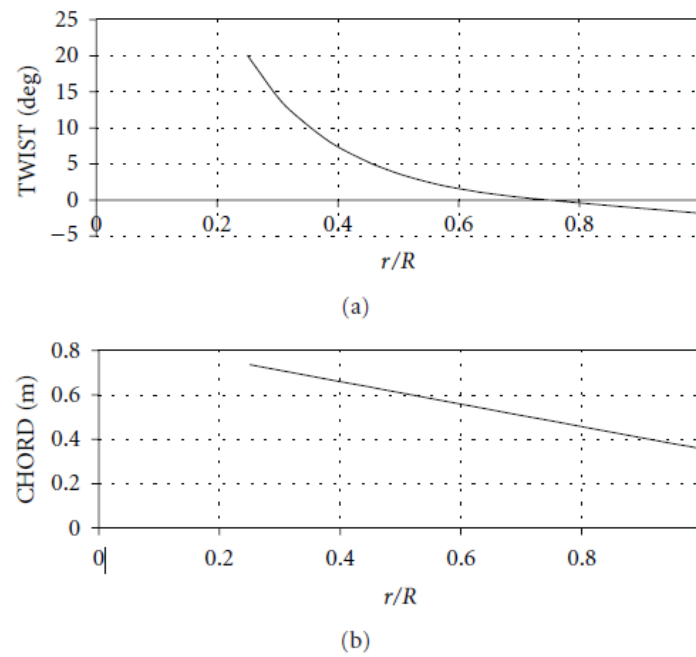
Figure 5-3 (a) Twist distribution; (b) chord distribution for the NREL VI blade.
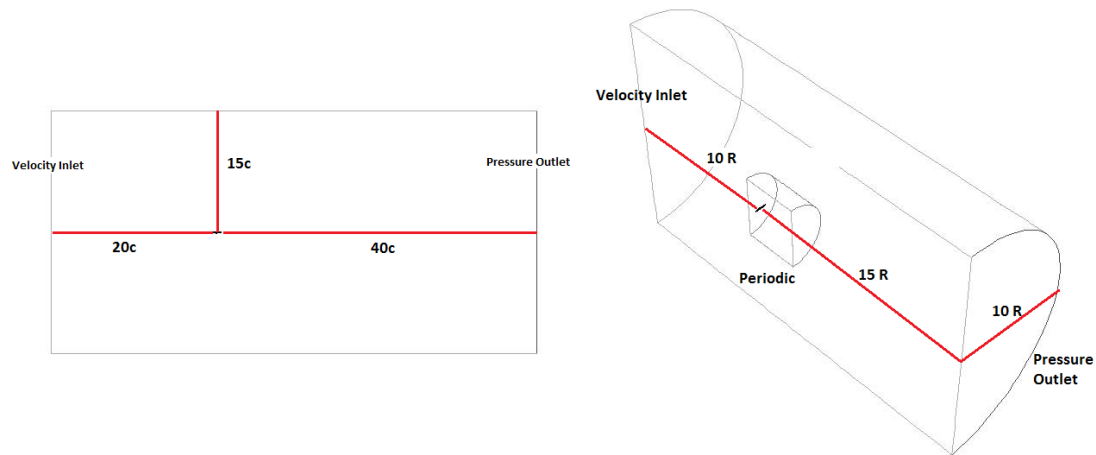
Figure 5-4 Computational domains for 2D and 3D analysis.
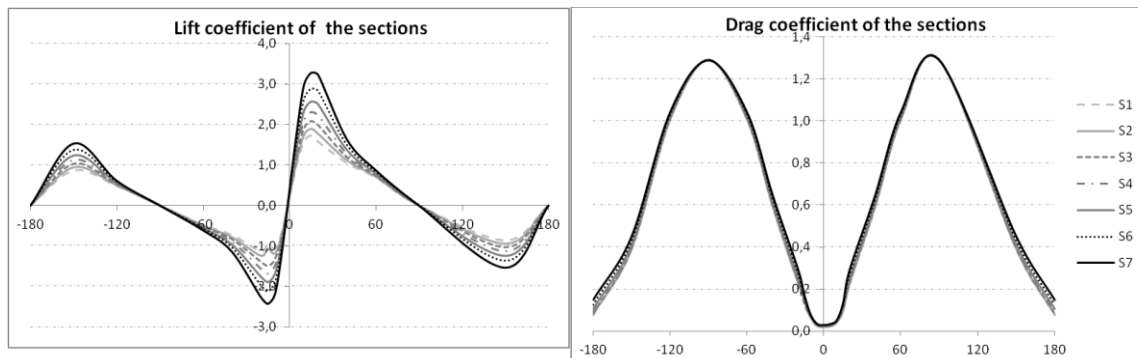
Figure 5-5 Lift and drag coefficients computed at each section.
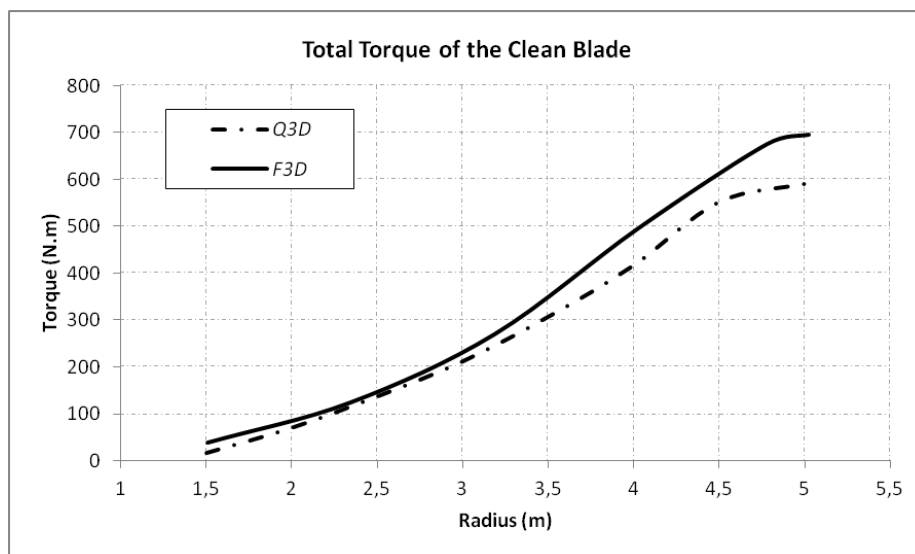
Figure 5-6 Total torque of a clean wind turbine from the root to the tip of the blades.
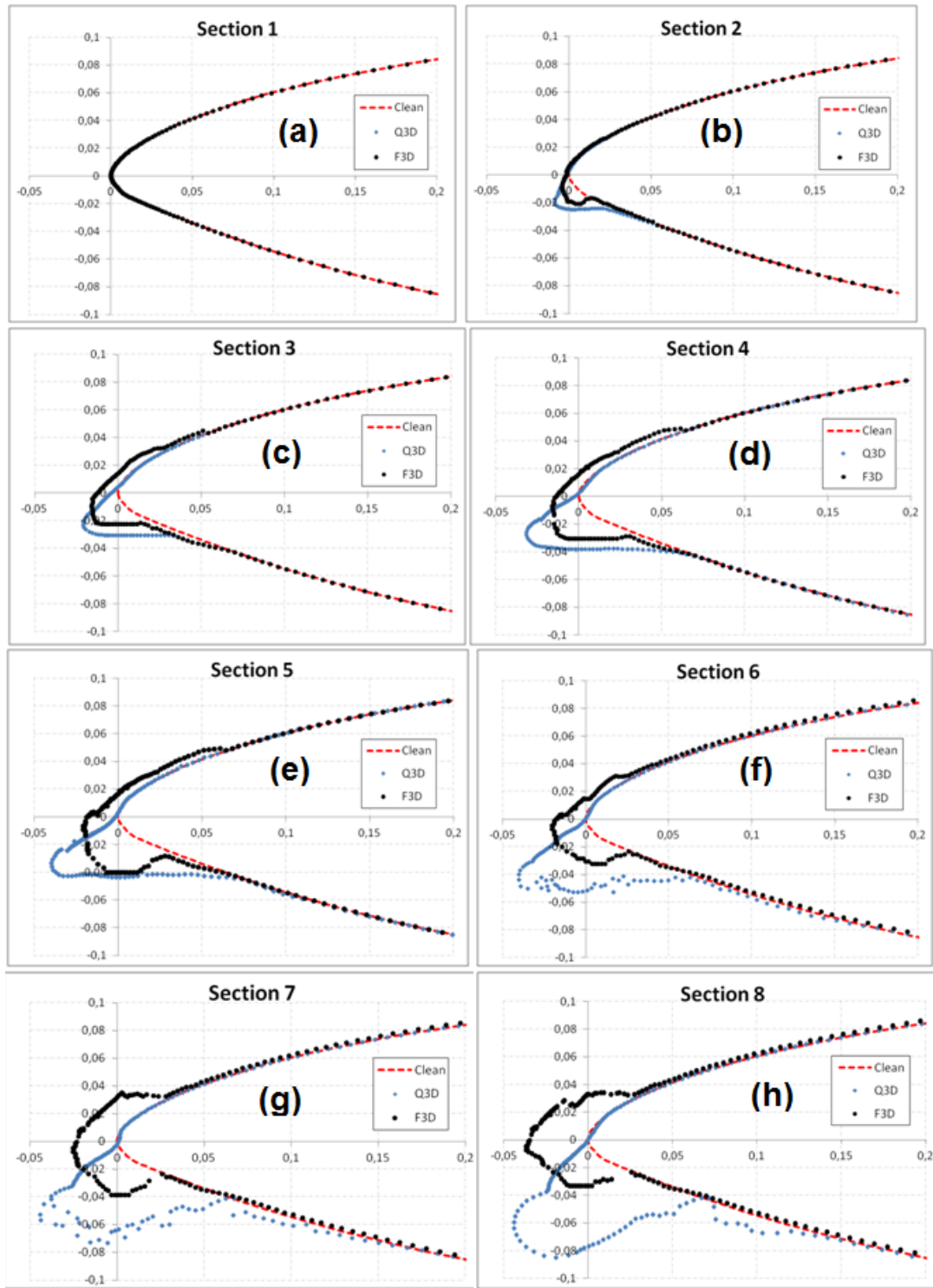
Figure 5-7(a)-(h) Ice shapes computed during 60 minutes of precipitation.
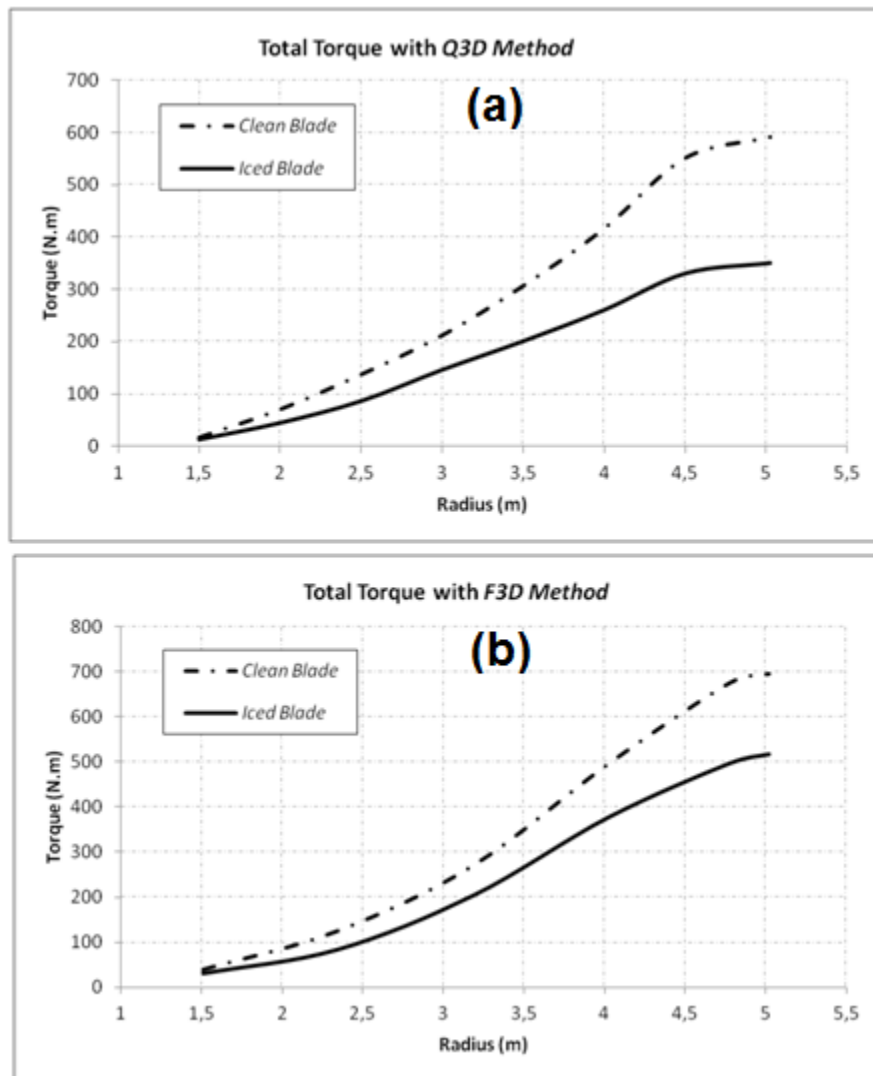
Figure 5-8 Comparison of total torque for clean and iced wind turbine blades for: (a) the Q3D method; and (b) the F3D method.
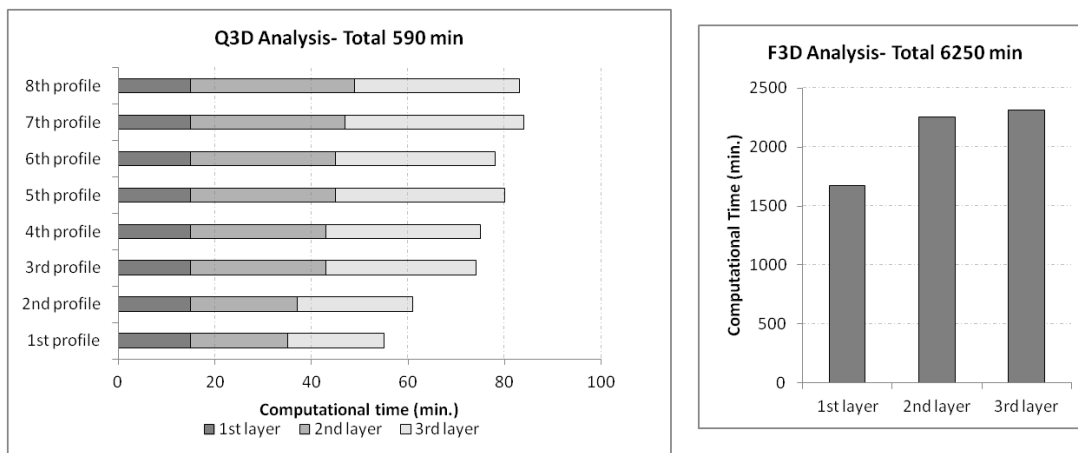
Figure 5-9 Computational time for ice accretion for the Q3D and F3D methods.

Table 5-1Characteristics of the NREL Phase VI experimental wind turbine.

Number of blades	2
Radius	5.029 m
Airfoil	S809
Root chord	0.7366 m
Tip chord	0.3808 m
Root twist	21.8^{o}
Tip twist	-1.775^{o}
Rotational speed	72 rpm

Chapter 6 ARTICLE 4: NUMERICAL EVALUATION OF THE ROUGHNESS EFFECT ON WIND TURBINE PERFORMANCE

Ece Sagol[1*], Marcelo Reggio[1], Adrian Ilinca[2]

1 Polytechnique Montréal, 2500 Chemin de Polytechnique, H3T 1J4, Montréal, Québec, Canada

2 Université du Québec à Rimouski (UQAR), 300, allée des Ursulines, G5L 3A1 Rimouski (Québec) Canada

6.1 Abstract

Various airborne contaminants like dust, ice, and insects may create irregularities on wind turbine blades. The presence of these elements on blade surface affects wind turbine performance depending on roughness size, location and density. Experimental and numerical studies that investigate the aerodynamic characteristics of aircraft airfoils and wings under various roughness configurations are available in literature. Yet, very few are addressing how roughness affects wind turbine performance. In this study, we model and quantify the sensitivity of the machine performance to increasing roughness height and find the roughness height above which performance is insensitive any changes. We also examine the roughness effect at different wind speeds, emphasizing on pre-stall, stall and post-stall conditions. The numerical analyses are performed with a commercial Computational Fluid Dynamics (CFD) tool, ANSYS FLUENT, with k-ω SST turbulence model. The simulations are performed for three different wind speeds, 7 m/s, 10 m/s and 15 m/s, and for six different roughness height ranging from 0.1 mm to 2 mm. The results showed that for pre-stall and stall wind speeds the performance decreases with increasing roughness height. The reduction in performance is more significant at lower wind speed. For post-stall wind speed, we observe an increase in performance proportional to roughness height. Moreover, a comparison against experimental data on dust contamination showed that mean power loss values are realistic. Finally, Annual Energy Production of the machine is computed for different scenarios that depend on roughness size, roughness duration and average wind speed of the sample wind farm. A comparison against clean energy production

shows that for low wind speed regions surface roughness may cause energy loss up to 25.9 %, whereas for the high speed regions maximum energy loss is 19.64 %.

6.2 **Introduction**

Fossil fuels are still the primary and the most widely used energy source, however, they are not renewable and are related to a number problems, first and foremost global warming. Therefore, countries are making efforts to seek for cleaner and more sustainable alternatives, i.e. renewable energy. Among those alternatives, wind energy has faced significant progression due mainly to its availability and competitive cost. One of the technical challenges in this rapidly growing industry is that wind turbines are unavoidably exposed to the environmental conditions that prevail in the location where they are erected, from icy, arctic-type environments to deserts with sand storms. There are contaminants in all of them, like dust, dirt, ice, and even insects (Weiss) (Khalfallah & Kolub, 2007) (Corten & Veldkamp, 2001) (Sagol, E.; Reggio, M.; Ilinca, A., 2013). These contaminants generate irregularities on this once smooth surface and consequently affect performance of wind turbines by decreasing lift and increasing drag.

Several researchers investigated this performance loss due to roughness, by performing wind tunnel experiments on airfoils, aircraft wings and occasionally on wind turbine blades. For wind tunnel experiments, surface soiling is simulated by applying tripping wire, zig-zag tape or contamination agents. This eliminates the need for 3D molds in wind tunnel experiments. Experimental results show that roughness on airfoil/blade may seriously decrease lift and increase drag depending on its size, location and density. The viscous drag increases with roughness, whereas the pressure drag is affected at higher angles of attack where separation takes place (Sagol, Reggio, & Ilinca) (Lachmann, 1960) (Pechlivanoglou, 2010) (Petrone, de Nicola, Quaglierella, Witteveen, & Iaccarino, 2011) (Bragg, Broeren, & Blumenthal, 2005) (Busch, 2009) (Turner, Hubbe-Walker, & Bayley, 2000) (Kerho & Bragg, 1997). Freudenreich et al. (2007) experimentally investigated clean and rough configurations of a thick, state-of-the-art wind turbine blade for two configurations; with a tripping wire at suction side of leading edge and 60 grain carborundum (Carborundum 60) applied to the leading edge of the model. The former slightly increases lift and drag coefficients while decreasing lift-to-drag ratio a little. Carborundum 60 configuration, however, has more impact on flow field. The boundary layer goes into early transition at the leading edge. Moreover, as the boundary layer thickens due to the

roughness elements, drag increases and early stall is induced. The maximum lift-to-drag ratio is yielded by Carborundum 60, which is around 40% of that of the clean configuration. Comparison of results for these configurations shows that for the roughness analysis a distributed roughness is necessary to represent a real case.

These studies also examine the effect of roughness size and density on wind turbine airfoils and blades (Ferrer & Munduate, 2009) (Li, Li, Yang, & Wang, 2010) (Gregory & O'Reilly, 1973) (Ren & Ou, 2009). As roughness size, which is usually proportional to the diameter of a spherical figure, increases, the degradation of performance also increases as a result of decreasing lift and increasing drag. However, there is a point where these coefficients become insensitive to roughness height, which is called the critical roughness size in the literature. Moreover, roughness location and density has great effect on performance as well. Leading edge roughness causes more performance loss than trailing edge roughness. Additionally, increasing density, up to a threshold, has more negative effect on performance as well.

As performing full-scale or scaled wind tunnel experiments is expensive, numerical tools, whose accuracy and speed increases day by day, are preferred for the design and analysis of wind turbines. Although numerical models are capable of predicting clean wind turbine performance, the accurate simulation of rough configurations is still under development. Concerning the roughness effects, several efforts have been made to model it by modifying wall function terms in turbulence models. A review of these studies is presented in a previous work, Chapter 4. Comparison against experimental data shows that k-ω SST turbulence model, with necessary modifications and fine grid resolution near the wall, can model the effect of roughness (Sagol, Reggio, & Ilinca, 2012), (Knopp, Eisfeld, & Calvo, 2009) (Vilalpando, Reggio, & Ilinca, 2012).

The current work focuses on quantifying the performance loss of a wind turbine for a range of roughness height by means of numerical algorithms. By doing so, we will answer the questions of how the performance is affected with increasing roughness height and what is the roughness height threshold above which performance is insensitive. We will also examine the roughness-performance relationship for different wind speeds; emphasizing on pre-stall, stall and post-stall conditions. The numerical analyses are performed using a commercial Computational Fluid Dynamics (CFD) tool ANSYS FLUENT with k-ω SST turbulence treatment. The surface roughness is activated using a modification available within the turbulence model. The

simulations are performed for three different wind speeds; 7 m/s, 10 m/s and 15 m/s, and for six different roughness height ranging from 0.1 mm to 2 mm. The results are compared in terms of machine torque and turbulence intensity near wall. Moreover, loss of Annual Energy Production, based on a typical wind farm data in Quebec, is computed and illustrated for various roughness size and duration.

6.3 **Methodology**

6.3.1 **Test Case**

NREL Phase VI wind turbine is chosen as a sample computational model since the quality of the experimental data of this case is confirmed by many researchers. The wind tunnel experiments have been conducted by the National Renewable Energy Laboratory (NREL) in the NASA-Ames wind tunnel at Moffett Field, California, in 2000 (Hand, Simms, & Fingersh, 2001) (Simms, Schreck, Hand, & Fingersh, NREL). The detailed information about rotor shape and size of the NREL Phase VI wind turbine are given in Table 6-1. For the entire blade, S809 airfoil is used. Linear chord and nonlinear twist distributions are shown in Figure 6-1. The blade root is completely circular up to 0.883 m, and, from this point up to 1.2573 m, the shape smoothly transforms from a circle into an airfoil configuration.

6.3.2 **Numerical Scheme and Mesh Characteristics**

For the current study, ANSYS FLUENT 12.0.16 is used among the commercial CFD tools available. The package is a finite volume-based solver, which allows both structured and unstructured grids to discretize the computational domain (ANSYS, 2010). The software allows transient calculations as well as steady-state computations to be performed. Parallel computation capabilities also ease large meshes handling by reaching solutions in a reasonable time scale. In order to reduce the time spent on the analyses, we made a number of assumptions prior to setting up the numerical scheme. Initially, physical presence of the tower and nacelle are ignored to reduce the mesh size and complexity of the problem. Many studies also concluded that their effects on rotor flow field are negligible. Moreover, the flow field is considered axisymmetric to be able to simulate one blade using rotational periodic boundary condition. Also, we use a rotating reference frame approach; the flow field rotates in the opposite direction of blades. All

these assumptions simplify the problem in terms of boundary conditions, computational cost, and results post-processing.

For the flow field, incompressible Reynolds-Averaged Navier-Stokes (RANS) equations, along with SIMPLE (Semi-Implicit Method for Pressure-Linked Equations] coupling, are used in ANSYS FLUENT. For turbulence treatment, the k-ω SST model, which has been found to be the most appropriate in a previous study, (Sagol, Reggio, & Ilinca, 2012) , was implemented. Moreover, modeling of the surface roughness is activated within the algorithm. There are two parameters to be modified in the code; roughness constant and roughness size. The roughness constant controls how roughness elements are distributed over the surface. For our case, we assumed a uniform roughness distribution over the blade. Modifications of wall boundary conditions for the roughness constant and roughness height are originated by Cebeci and Bradshaw (1977), and adapted by ANSYS FLUENT .

A hybrid volume mesh comprising triangular prism and tetrahedral elements is preferred for the domain discretization. The surface mesh was generated using GAMBIT, formerly the companion software of FLUENT. To resolve the boundary layer, 20 prism layers normal-to-surface elements on the blade were generated. The initial height selected was $2*10^{-4}$ m, which guarantees to maintain a reasonable value for y^+. Besides, physically meaningful computations are possible when the initial height is greater than the size of the roughness element. A basic mesh dependency study to find optimum resolution for the numerical analysis was performed.

The computational domain and the boundary conditions are illustrated in Figure 6-2. As seen, an inner domain is generated to increase the mesh density around the blade. For the inlet boundary condition, a velocity normal to the inlet boundary and the turbulence intensity, which are provided by experimental data, were imposed. The outer cylindrical domain is also treated as an inlet, and the same boundary conditions are applied. For the outflow boundary, the pressure outlet boundary condition is enforced by applying atmospheric pressure, as the flow is far from the wind turbine. For the inner surfaces, as explained above, rotational periodic boundary conditions are applied. Finally, the blade surface was treated as a non-slip wall boundary condition; that is, a zero velocity is imposed. For the rough cases, a roughness height is defined on the surface.

Parallel computations are performed using 8 cores of clusters of Mechanical Engineering department of Ecole Polytechnique de Montreal. Each processor is 2.00 GHz Intel Xeon machine with 4GB RAM. Each analysis took about 26.5 hours for 4000 iteration.

Annual Energy Production (AEP) is the total energy generated by a unit wind turbine in a particular location, within a year. The AEP computation requires the knowledge of wind speed frequency data of the location (in general a Weibull distribution), and power curve of the machine. Although AEP depends on many parameters as availability of the machine and array losses, only contamination losses are considered for our computation. The AEP is computed as in Equation 6-1;

$$AEP = T \int_{V_{cut-in}}^{V_{cut-off}} P(V) f(V) dV$$

6-1

Here, T is the operational time span which is 8760 hours for our case. V_{cut-in} and $V_{cut-off}$ are the cut-in and cut-off wind speed, between which the wind turbine can safely operate. The producer data defines cut-in and cut-off speed as 5 m/s and 25 m/s, correspondingly. $P(V)$ is the power curve of the machine and $f(V)$ is the Weibull wind frequency distribution of the wind at the site. This distribution is computed (in Equation 6-2) by a function that depends on a scale parameter, c, proportional to average wind speed and a shape parameter, k as;

$$f(V) = \left(\frac{k}{c}\right) \left(\frac{V}{c}\right)^{k-1} e^{[-\left(\frac{V}{c}\right)^k]}$$

6-2

The wind speed frequency data is derived from a study that evaluates wind potential analysis in Quebec (Helimax Energie). In this analysis, a shape parameter, k, of 2.1 was presented for Gaspésie and the south of Quebec and wind sites are categorized from very low wind speeds, 0-6 m/s, to very high wind speeds, 9 + m/s . For our computations, three different regions with low (c=6 m/s), medium (c=7 m/s) and high (c=8 m/s) wind speed, are evaluated.

6.4 **Results and Discussion**

In this section, results of the numerical analyses are presented. To simulate the effect of roughness height, eight different values ranging from 0 to 2mm: 0mm (clean case), 0.1mm, 0.3mm, 0.5mm, 0.8mm, 1mm, 1.5mm and 2mm. The simulations are performed at three different wind speed as well, namely at 7m/s, pre-stall wind speed, 10 m/s , stall wind speed, and 15m/s post-stall wind speed.

The computed torque is presented in Figure 6-3, for each wind speed. Each of these results indicates that the machine performance decreases with increasing roughness height for pre-stall and stall wind speeds. For the post-stall speed, however, roughness has less effect and eventually it plays a performance booster role. Table 6-2 tabulates the power loss compared to its clean state for each roughness height and a mean power loss value computed by averaging the losses at each wind speed. The predicted threshold values are shown in red.

The results show that at pre-stall speeds, the machine power, which experiences a maximum of 36.2 % loss, is more prone to decay with the increasing roughness height. The torque continues to decrease up to a roughness size of 0.5mm, after this value the rate of loss slows, yet still active. At the stall speed, 10 m/s, the torque still decreases with increasing roughness height. Yet, the threshold value decreases to 1-1.5 mm and the maximum power loss is 17.2 % compared to clean state. Finally at the post-stall speed of 15 m/s, the power production increases proportional to the roughness height. At this speed, the flow is fully separated at suction side of the blade. Therefore, roughness elements behave like a zig-zag tape mechanism that partly stabilizes the flow from separation. The threshold value in this speed is between 1 mm and 1.5 mm, and the torque increases up to 6.3 %.

The results are compared to the experimental findings on a 100 kW stall-regulated wind turbine exposed to controlled dust environment. Khafhallah and Koliub (2007) measured the mean power loss for various dust grain size and contamination rate without considering the effect wind speed and roughness size on the surface. Therefore this comparison cannot be accounted for an exact validation but examining if the findings make sense. The experimental results show that the dust contamination yielded a power loss of between 6.5 % and 38 %, from smaller size dust grains to bigger ones. If we relate that the smaller dust size is likely to create smaller roughness size, and the bigger ones create greater roughness size, our mean power loss is between 5.6 % and 15.7 %.

The near wall turbulent intensity values on the blade, for 10 m/s wind speed, are presented inFigure 6-4. The intensity values are normalized and a color scale from blue-to-red represents lower to higher turbulent intensity values. The upmost blade, representing the clean state (R=0), indicates that turbulent intensity is very low for whole blade. As the roughness height increases, a higher turbulent intensity values dominates a larger area on the blade, particularly at the tip and leading edge. It means that the rough surface triggers fluctuations of the turbulent velocity. And, as the height of the roughness increases, the flow becomes more turbulent, particularly at locations where local Reynolds number is higher. Because of this turbulent flow, less power is extracted from the rotation of wind turbine.

The turbulence intensity values shows similar trends, yet different characteristics for pre-stall speed, 7m/s. The rate of growth of turbulence intensity value with increasing roughness height is significantly higher at pre-stall speed, 7m/s compared to higher speeds. This indicates that roughness size effectively modifies the extent of turbulent boundary layer on the blade, particularly near the tip. For the post-stall speed, the turbulence intensity distribution shows a distinctive nature because of large separations taking place on the suction surface. Moreover, roughness does not seem to have a significant effect on turbulent intensity values.

Wind turbines are selected according to their power curve and of which depends the energy production in addition to the wind characteristics of the site. In the case of a contamination, expected power production will gradually decrease with increasing roughness height, as shown inFigure 6-5. This unpredicted performance loss, may have serious consequences on revenues due to inability to produce predicted energy. Therefore, it is important to take roughness into account when forecasting Annual Energy Production (AEP) of a wind turbine or wind farm. The torque as a function of wind speed for each roughness height is illustrated in Figure 6-4.To give an idea about the deviation from the experimental data, the actual torque of clean blade is included in the figure. The numerical results differs less from the experimental data for lower wind speeds compared to higher wind speeds. This is due to the inability of numerical algorithm to accurately simulate highly separated flow. The average deviation from experimental data is about 10 %. For AEP analysis, we extended the torque computations up to 20 m/s.

The AEP simulation scenarios are shown in Table 6-3. As seen a low, a medium, and a high wind speed site with scale factors, c, of 6, 7, and 8 are evaluated. The shape constant, k, is taken as 2.1

[30]. For roughness size, the clean wind turbine is compared against roughness size of 0.1 mm, 0.5 mm and 1 mm. Moreover, various duration of the contamination are also examined. 100 % CON, 50 %, and 10 % CON represent that the blade is contaminated during 100 %, 50 %, and 10 % of the total time. Resultant AEP for various roughness size and duration are illustrated inFigure 6-6, for the medium wind speed.

The results for medium wind speed region show that even the presence of the smallest size of roughness yields about 8 % loss of AEP if the contaminated blade is not cleaned all over the year. If the roughness size increases this loss may reach 23 % of the estimated energy production. When the operational time of the contaminated blade is decreased to 50 % of the total time, the loss decreases to 4-11 % of the estimated production, yet it is still unacceptable. Finally, for the Scenario 3 which assumes that the blade is contaminated during 10 % of the year, the AEP loss is much less important. For the maximum roughness size, the AEP loss is around 2.2 % of the estimated value. These results illustrate the need to clean the blades after contamination by dust and insect. In case of ice accretion such cleaning may not be needed unless the machine operates in steady winter conditions. The wind farm operators may perform similar computations to find the optimum time for blade cleaning. Needless to say, along with AEP computations, a cost analysis should be performed so that the cost of cleaning operations would not exceed the gain from the energy produced by clean blades.

Considering the roughness size and the contamination duration, low and high wind speed site AEP analyses produced similar trends for each scenario as medium wind speed site. The AEP losses for each scenario are tabulated inTable 6-4. However, the comparison of these three wind speed sites show that lower the average wind speed, the greater the AEP loss. This is obviously a result of the poor performance of the machine under rough conditions at low speeds, as illustrated inFigure 6-5. For the low speed wind site maximum loss reaches to 25.9% of the clean blade, whereas for the high wind speed site it is 19.6%.

6.5 Conclusion

In this study, we investigated the performance behavior of a wind turbine for various roughness height and wind speed conditions. For pre-stall and stall wind speeds, we observed an exponential power decrease with increasing roughness height, which indicates that the wind

turbine performance is inversely proportional to the roughness height. For post-stall speed, the power evolves differently and slightly increases with increasing roughness height. Moreover, each wind speed has a unique roughness height value above which the power remains unchanged. As the wind speed increases this threshold decreases, i.e. for lower wind speeds this threshold is higher.

The resultant power of clean blade is also compared against experimental data. Although the computational results deviate from experimental data, they can still provide a reasonable picture of the importance of the effect of the roughness. Moreover, a comparison of against an experimental data for dust accumulation showed similarity in terms of mean power loss of the machine.

In terms of annual energy production, we can assess that in lower speed regions, AEP loss may be as high as 26 % of its forecasted value. However, higher the wind speed, the less AEP is affected. Even for the post-stall wind speed, which is a unique value for each wind turbine, the power may increase temporarily up to 6 %. It is important to note that, for low wind speed regions, the wind turbine contamination leads to severe AEP loss. The washing of the blades after a certain running period is obviously an alternative that can be used to mitigate this problem. According to our numerical predictions, the cleaning of wind turbine is a procedure that needs to become part of a maintenance schedule for wind turbines, particularly for those exposed to dust, dirt and persistent icing.
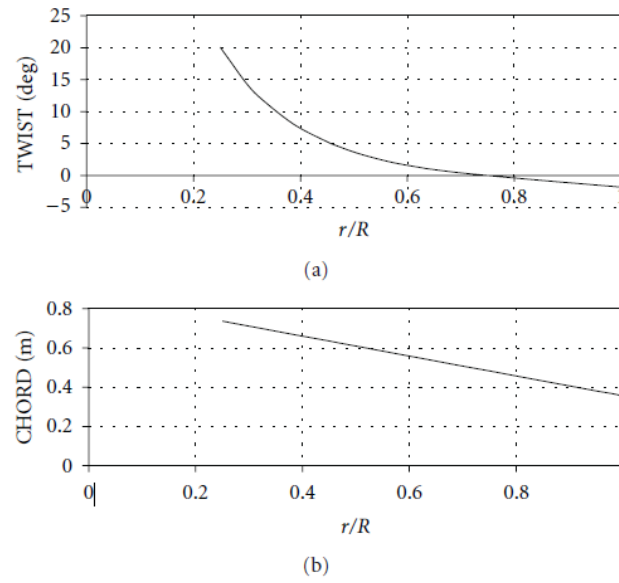
Figure 6-1(a) Twist distribution; (b) chord distribution for NREL VI blade
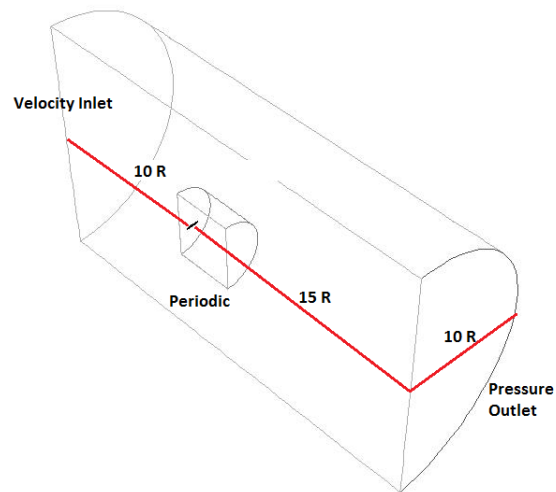
Figure 6-2 Computational domain with boundary conditions
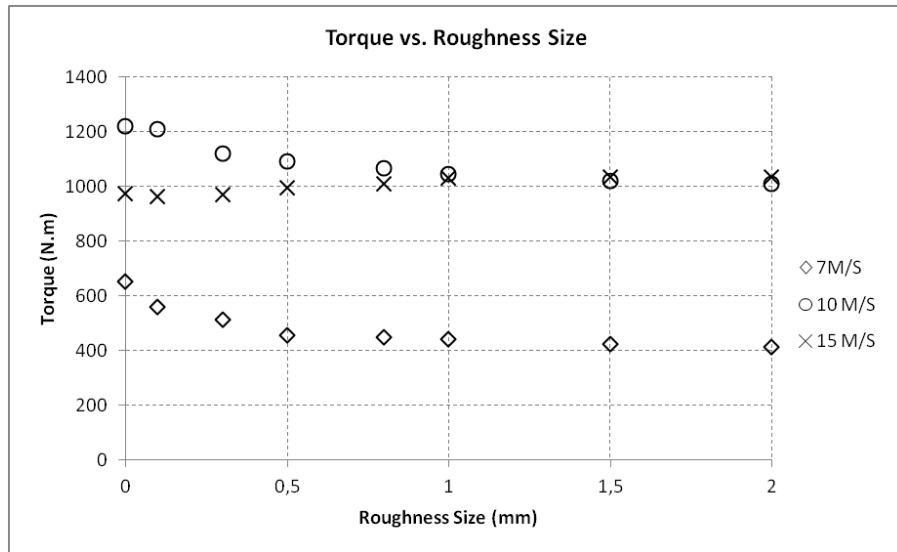
Figure 6-3 The computed torque for a range of roughness values for 7m/s, 10m/s, and 15m/s
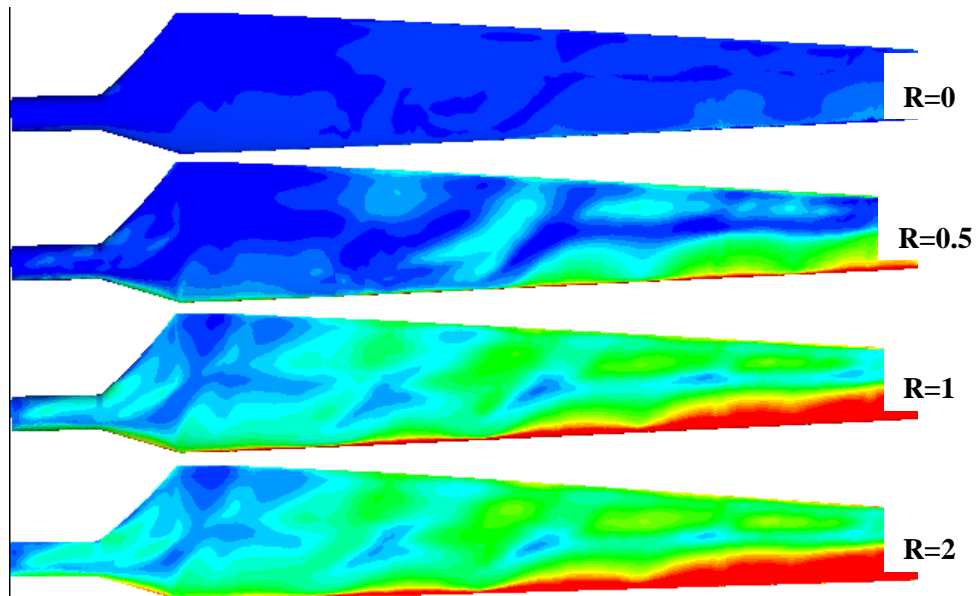
Figure 6-4 Turbulent intensity values on the blade at 10m/s wind speed
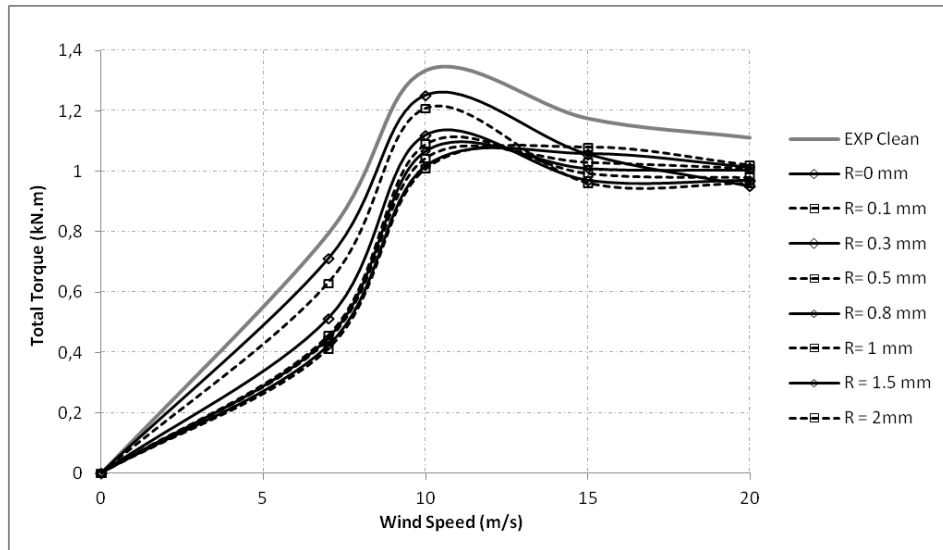
Figure 6-5 Total blade torque vs. wind speed for various roughness heights.
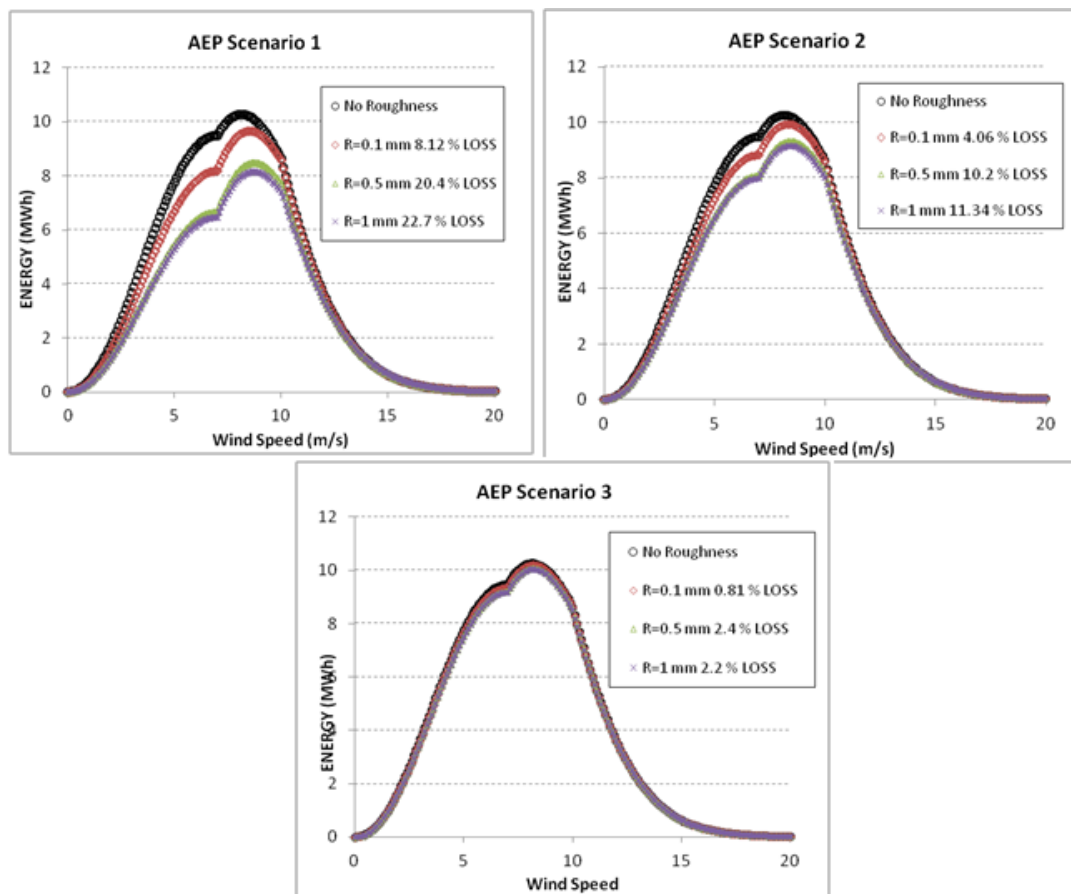
Figure 6-6 AEP for Scenarios 1-3 for the medium wind speed, 7m/s.

Table 6-1NREL phase VI experimental wind turbine characteristics.

Number of blades	2
Diameter	5.029 m
Airfoil	S809
Root chord	0.7366 m
Tip chord	0.3808 m
Root twist	21.8°
Tip twist	-1.775°
Rotational Speed	72 rpm

Table 6-2 The power loss of wind turbine compared to its clean state and estimated roughness threshold values

	7 m/s	10 m/s	15 m/s	Mean Power Loss
R=0.1 mm	13.8 %	2 %	1.1 %	**5.63 %**
R= 0.3 mm	21.1 %	8 %	0.2 %	**9.76 %**
R= 0.5 mm	29.8 %	10.5 %	- 2.2 %	**12.7 %**
R= 0.8 mm	31.1 %	12.3 %	-3.9 %	**13.2 %**
R = 1 mm	32 %	15.2 %	-5.9 %	**13.7 %**
R = 1.5 mm	34.1 %	16.4 %	-6.1 %	**14.8 %**
R = 2 mm	36.2 %	17.2 %	-6.3 %	**15.7 %**

Table 6-3 The scenarios of AEP analyses

	Scenario 1	Scenario 2	Scenario 3
LOW WIND	100 % CON	50 % CON	10 % CON
MEDIUM WIND	100 % CON	50 % CON	10 % CON
HIGH WIND	100 % CON	50 % CON	10 % CON

Table 6-4 The minimum and maximum AEP loss depending on roughness size

	Scenario 1	Scenario 2	Scenario 3
LOW WIND	9.9 % -25.9 %	4.9 % - 13 %	1 % - 2.6 %
MEDIUM WIND	8.1% – 22.7 %	4 % - 11.3 %	0.8 % - 2.2 %
HIGH WIND	6.7 % - 19.6 %	3.4 % - 9.8 %	0.7 % - 1.9 %

Chapter 7   **SAMPLE POWER AND AEP LOSS ANALYSES**

In this chapter, a sample icing analysis performed on a wind farm using the proposed methodology is presented. As no experimental data are available to validate specific results, like ice shape, blade performance, or wind turbine power curve, we performed a global comparison of the AEP with operational data from a wind farm. The selected wind site is located at Blaiken in northern Sweden. Icing events are recorded with a camera mounted on the wind turbine, and the atmospheric conditions are measured with heated instruments (Carlsson 2009). The power curve and AEP losses are computed for various wind speeds, the LWC of the air, and water droplet sizes. The aim of the calculations performed at this wind farm site is not a direct comparison, as the wind turbines analyzed are very different, but rather to evaluate the sample wind turbine in real icing conditions, and to determine whether or not the power and production losses can be correlated to recorded icing events. These events, along with related atmospheric conditions, and the wind turbine power losses are presented in Table A. 3 in Appendix. As we can see, an icing event for a wind turbine may last up to 360 hours, depending on the location of the wind turbine site. LWC and MVD are computed using humidity, temperature, and mean pressure measurements. The computation of MVD requires the droplet concentration, N. Since this number is not measured, we have taken it from another study (Drage and Molmann 2005), which investigates atmospheric icing on structures. According to this study, N is typically between $10^8/m^3$ and $10^{10}/m^3$. Therefore, for our analyses, we will perform a parametric analysis ($N_1 = 10^8$, $N_2 = 10^9$, and $N_3 = 10^{10}$) to determine the effect of droplet concentration on icing. For the remaining analyses, the average droplet concentration, $N_2 = 10^9$, will be used. The maximum, minimum, and average values of these quantities are computed as shown in Table 7-1.

Table 7-1 Liquid Water Content and Droplet concentration values for the selected wind site

LWC_{min}	$0.04\ g/m^3$
LWC_{ave}	$0.1\ g/m^3$
LWC_{max}	$0.22\ g/m^3$
N_{min}	$10^8/m^3$
N_{ave}	$10^9/m^3$
N_{max}	$10^{10}/m^3$

The simulation matrix is presented in Table 7-2. All the ice accretion simulations are performed at the mean wind speed of the selected wind site, which is 7 m/s. A mean or median wind speed is not provided for the icing events. For this reason, the mean wind speed of the wind farm is used for the icing analysis. The icing duration is derived from icing events. Note that icing duration does not refer to the duration of the accumulation, but to the total number of hours that ice remains on the structure. When the icing events are analyzed from the measurement of the ice loads on the blade, we see that the precipitation time covers about one-third of the icing duration indicated. The rest of the time is a measure of the period during which ice remains on the structure without melting or shedding. As it would be quite costly to analyze the power loss per hour, we selected time intervals of 9 hours for computing power production throughout the range of operating speeds of the wind turbine. The first five simulations are for the parametric analyses of the LWC and the droplet concentration computed for 3 hours of icing. The time interval for updating the ice shape during the computation process is 1 hour. For instance, during a 24-hour icing computation period, the ice shape will be updated 24 times to take into account the effect of the updated airfoil shape on the flow field.

After the ice accretion process is complete, the iced blade is analyzed for a range of wind speeds, from a cut-in wind speed of 5 m/s to a cut-out wind speed of 25 m\s. This analysis enables us to document the power curve of the iced wind turbine.

Table 7-2 Test matrix

SIM #	Icing Duration (h)	LWC (g/m^3)	N ($1/m^3$)	MVD (μm)	Wind Speed (m/s)
Sim1	3	0.04	10^9	7	7
Sim2	3	0.1	10^9	10	7
Sim3	3	0.22	10^9	12	7
Sim4	3	0.1	10^8	20	7
Sim5	3	0.1	10^{10}	5	7
Sim6	9	0.1	10^9	10	7
Sim7	18	0.1	10^9	10	7
Sim8	27	0.1	10^9	10	7
Sim9	36	0.1	10^9	10	7
Sim10	45	0.1	10^9	10	7
Sim11	54	0.1	10^9	10	7
Sim12	63	0.1	10^9	10	7
Sim13	72	0.1	10^9	10	7

7.1 **Parametric Analysis**

In this section, parametric analyses for LWC and droplet concentration are performed to study the effect of these parameters on ice accretion and machine performance. An ice accretion period of 3 hours is considered in each analysis, and the ice layer parameters are updated every hour.

Sim1, Sim2, and Sim3 correspond to the minimum, average, and maximum LWC of the air respectively. Droplet concentration is assumed to be constant at its average value at 10^9. Moreover, MVD, which is a function of LWC and droplet concentration, is computed and presented in Table 7-2. The ice shapes computed for the Liquid Water Content Variation are shown for certain profiles of the blade, as presented in Figure 7-1.
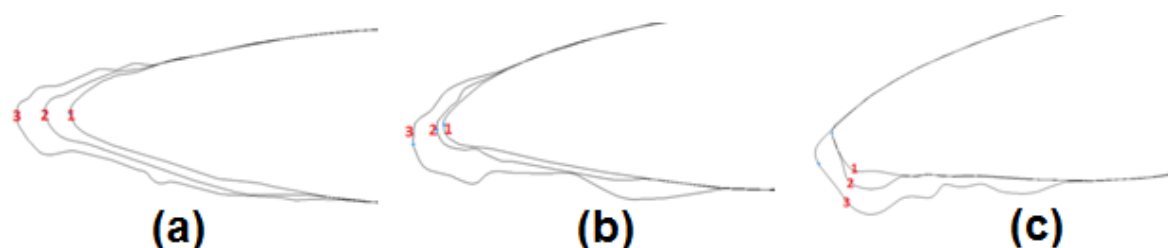
Figure 7-1 Ice shape variation for Sim1, Sim2 and Sim3

The resulting ice shapes show that the LWC of the air has a strong influence on the ice shape. As the LWC of the air increases, the ice thickness on the blade also increases, with the direction of the growth of the ice remaining the same for all the analyses. In general, the ice covers more space on the pressure side than on the suction side. The power curves computed for Sim1, Sim2, and Sim3 are shown in Figure 7-2. As we can see, power production is directly related to the degradation of the aerodynamic profile. The results show that the maximum LWC, which corresponds to Sim3, has the most contaminated profile, as well as the lowest power production. The average loss of power production from the clean blade power production for the minimum LWC simulation, Sim1, is 2.2%. This value is 7.4% for the average LWC – Sim2 – and 17.7% for the maximum LWC – Sim3.
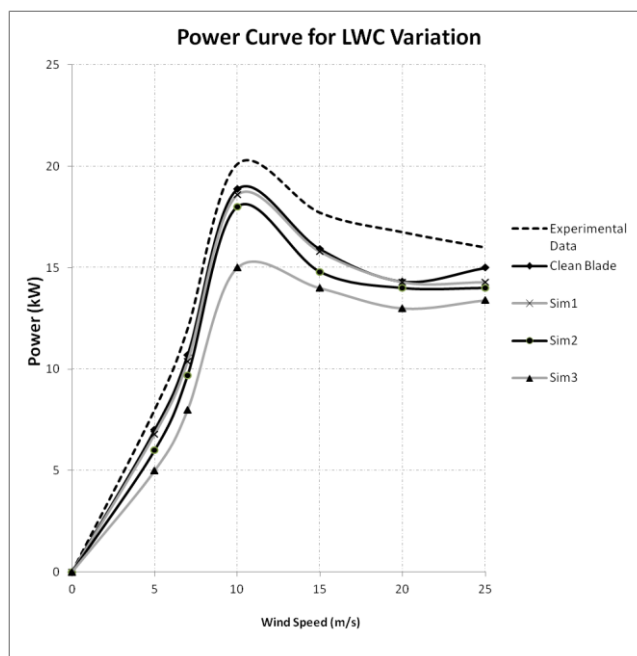
Figure 7-2 Power curve variation for clean blade and Sim1, Sim2, and Sim3

A minimum, an average, and a maximum droplet size are analyzed in simulations Sim5, Sim2, and Sim4 respectively. In this analysis, the LWC of the air is kept constant, and the size of the droplets (MVD) was altered by adjusting the droplet concentration. The computed ice shapes are illustrated in Figure 7-3. As seen from the figures, droplet concentration has less effect on the ice shape profile than LWC.
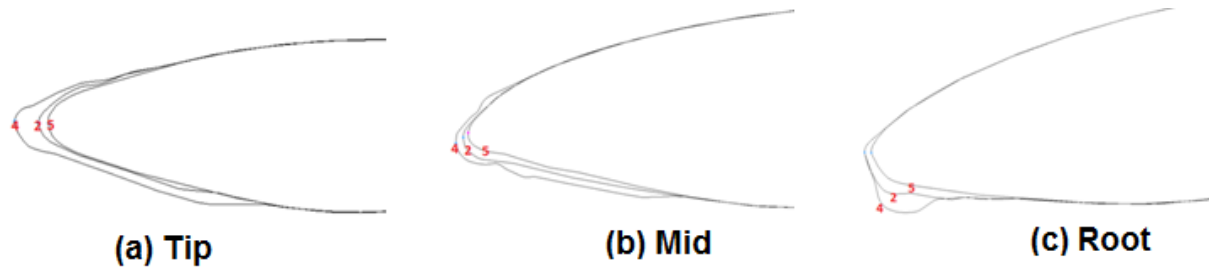
Figure 7-3 Ice shape variation for Sim2, Sim4, and Sim5

The corresponding power production losses are presented in Figure 7-4. They are 4.5%, 7.4%, and 13.4%, corresponding to the maximum, average, and minimum droplet size respectively. As the droplet concentration increases, the droplet size decreases, as the LWC of the air is constant. Since the smaller droplets have less inertia, they are easily carried along by the air flow. Consequently, although there are more droplets in the air, they deviate from the surface of the blade. In contrast, when the droplet concentration is minimal, the droplets are larger, in which case, the supercooled water droplets target the blade and the air flow is not strong enough to drag them away from the surface. As a result, a thicker ice shape forms, as illustrated in Figure 7-3.
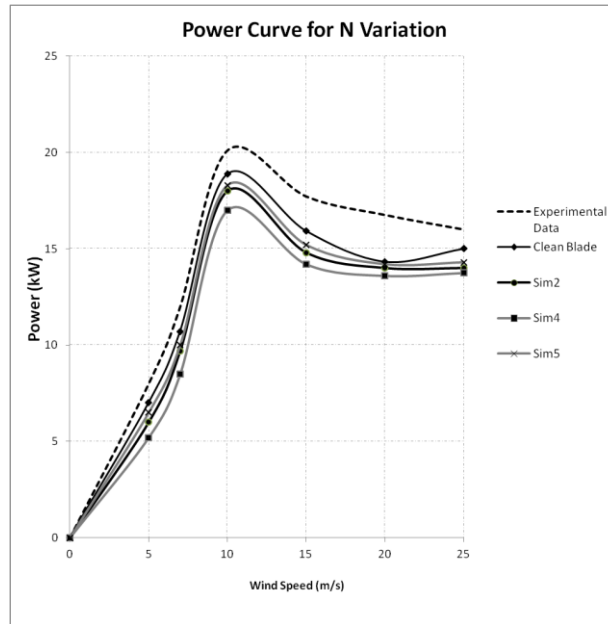
Figure 7-4 Power curve variation for clean blade and Sim2, Sim4, and Sim5

7.2 **Annual Energy Production (AEP) Loss**

The icing analyses performed for the computation of AEP loss are presented in the test matrix in Table 7-2. For these analyses, the LWC is kept constant at 0.1 g/m^3 and the droplet concentration is $10^9/m^3$. The ice accretion analyses are performed at the average wind speed of the wind farm site, which is 7 m/s. The ice shape was updated every hour. The power curve was computed every 9 hours.

The locations of the resulting 3D ice shapes are illustrated in Figure 7-5. To provide a picture of the ice growth on the blade during the three time intervals, we show the actual growth profiles at the tip, mid-span, and the root of the blade in Figure 7-6.
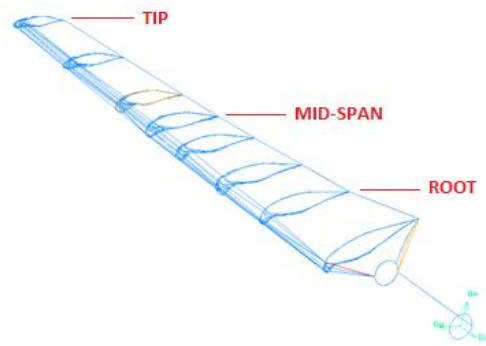
Figure 7-5 3D ice shapes computed up to 72 hours of icing
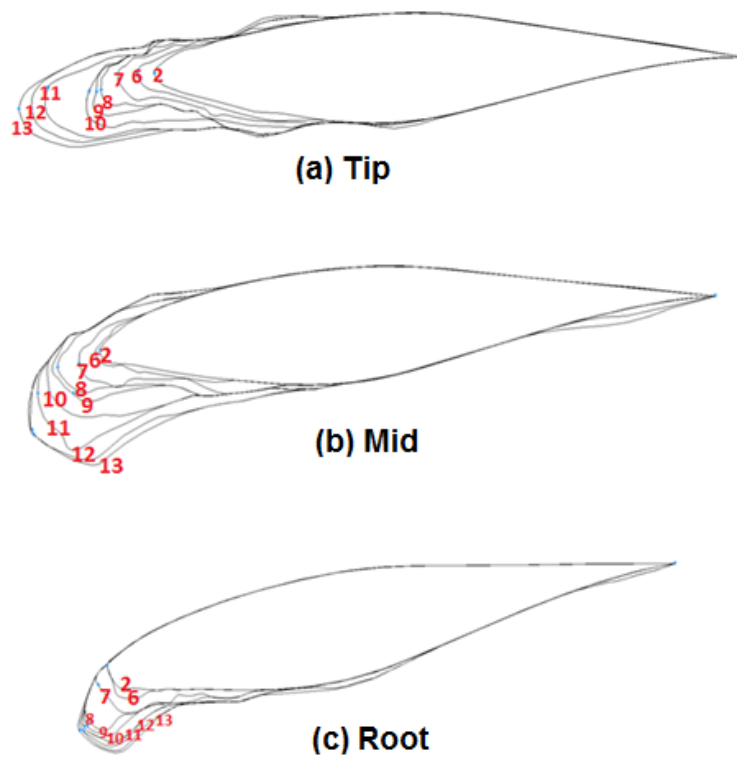
Figure 7-6 Ice growth with time for a) tip, b)mid-span, and c) root of the blade

It is interesting to note that the ice growth extends to the trailing edge of the blade, from mid-span to the root. However, this growth is only observed for Sim12 and Sim13 for the mid-span

portion, and for Sim 10 and Sim 11 for the root of the blade. The reason for ice accretion at the trailing edge is a small separation, which can be seen on the pressure side. The source of this separation is a nose-like structure which formed at the leading edge in Sim 11 for the mid-span portion. The power curves for these simulations are presented in Figure 7-7. As we can see, the power production of the machine seems to gradually decrease with time or increase with ice thickness. We see that the greatest power loss occurs at lower wind speeds. The power production losses at each wind speed and in each ice accretion simulation are presented in   Table 7-3. Here, the power production loss can be as high as 67% of the nominal production computed.
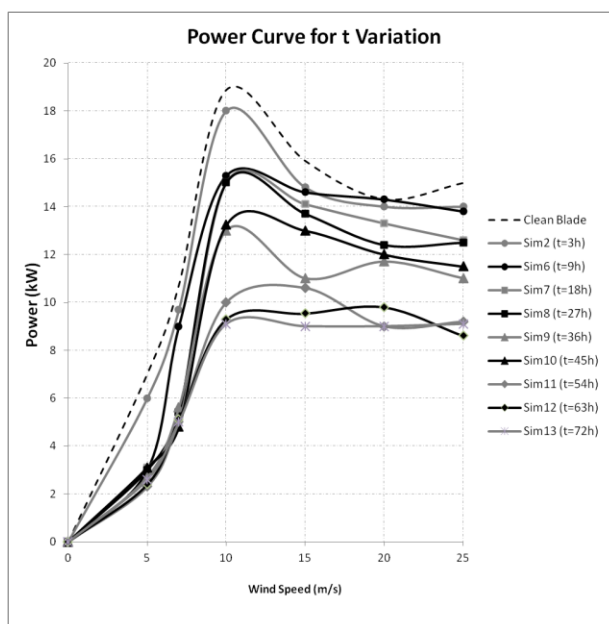
Figure 7-7 Power curve variation for ice accretion simulation through the time.

Table 7-3 The power production losses due to icing of 3 to 72 hours

Wind Speed	Sim2	Sim6	Sim7	Sim8	Sim9	Sim10	Sim11	Sim12	Sim13
5 m/s	14.29%	57.14%	55.71%	57.14%	61.43%	55.71%	67.14%	65.71%	62.86%
7 m/s	9.40%	15.94%	53.30%	49.56%	47.70%	55.17%	53.30%	52.37%	53.30%
10 m/s	4.66%	18.96%	20.55%	20.55%	31.14%	29.90%	47.03%	50.74%	51.80%
15 m/s	7.06%	8.32%	11.46%	13.97%	30.92%	18.36%	33.44%	40.08%	43.48%
20 m/s	2.28%	0.18%	7.16%	13.44%	18.33%	16.24%	37.18%	31.59%	37.18%
25 m/s	6.67%	7.86%	16.00%	16.67%	26.67%	23.33%	38.67%	42.67%	39.33%

The power loss owing to ice accretion is computed for different wind speeds and compared with wind farm data, as shown in Figure 7-8. It is important to note that it is not our objective to compare these power loss figures with wind farm data, as the ice shape is computed for a single wind speed and the power loss is computed with respect to this ice shape for the operational wind speed range. Also, wind speeds are not provided for icing events. What this visual comparison of the power loss figures shows is that the computed power loss lies in the same range as that of the wind farm. It should also be noted that not all the icing events in Table A. 3 are included in the figure. Those that occurred in an ambient temperature higher than -2°C are considered to involve glaze icing, and are not taken into account in the comparison.
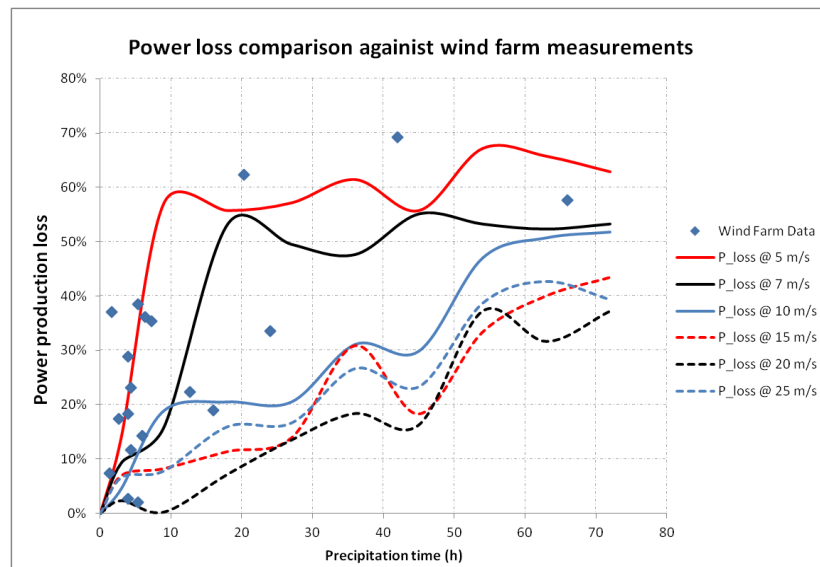
Figure 7-8 Comparison of power loss due to icing for various wind speeds

For the computation of the AEP loss, the Weibull distribution of the wind farm is used, as shown in Figure 7-9. The wind farm site has a shape parameter of 1.95 and a scale parameter of 7.2 m/s. The AEP is computed for a nominal, clean configuration and for the iced configuration using the formulas 6-1 6-2. In a nominal configuration, the AEP is 859 MWh, whereas for the iced configuration it is 802.1 MWh. Therefore, an AEP loss of 6.62% is observed for the sample wind turbine and the sample icing conditions.

For a more accurate analysis, icing conditions such as wind speed, wind direction, ambient temperature, and LWC should be measured and recorded over a specified period of time.
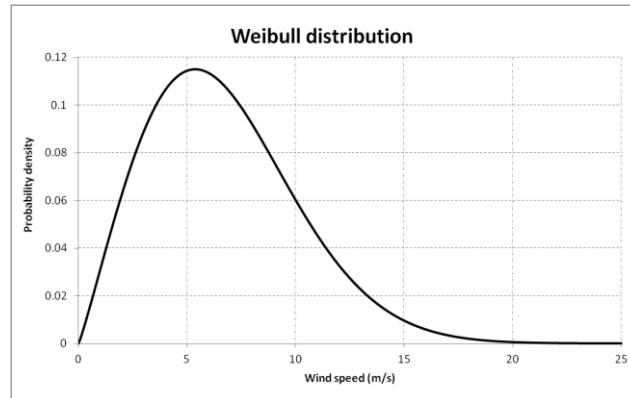
Figure 7-9 Weibull distribution of the sample wind farm in Blaiken, Sweden

Chapter 8   **GENERAL DISCUSSION AND CONCLUSION**

Canada experiences long, cold winters, which means that wind turbines installed in its arctic and sub arctic regions are exposed to icing. This has adverse effects on both the performance and the life expectancy of the machines. Predicting the performance reduction due to icing is therefore an important concern for the wind energy industry. In fact, the aircraft industry has put a great deal of effort into modeling ice accretion, and into the removal of accumulated ice from aerodynamic surfaces and engines, because of the danger it poses for the integrity of aircraft. Of course, research budgets in the aviation industry are significantly larger than they are in the wind energy industry. Luckily, wind energy researchers have also benefited from these findings to some extent. However, although the airfoils of wind turbines and aircraft are similar, the conditions in which they operate are significantly different. For instance, wind turbine blades are subjected to lower wind speeds and higher angles of attack than aircraft. More importantly, they are exposed to longer icing periods, and so they may operate continuously for several days in icing conditions, whereas aircraft operation in these conditions is measured in hours.

A few icing codes have been developed for wind turbines. However, these are either in 2D, in which case the 3D characteristics of the flow field are not considered, or they focus on simulating each rotation in a time-dependent manner, which is not practical for computing long hours of ice accretion. A previous study, performed by Villalpando, has investigated both rime icing and glaze icing on wind turbine airfoils with heat applied to their surface. In his conclusion, Villalpando stresses the need to develop an improved thermodynamic model, in addition to conducting 3D simulations. We have focused on the latter concern in this study, the former being outside the scope of our investigation.

8.1 **Summary of the Work**

The methodology and the sub results of this study have been submitted as articles to international scientific journals. Two of these articles have already been published. The first paper (Sagol, E.; Reggio, M.; Ilinca, A. 2013), reviews the effects of surface roughness, which is the result of contamination, on the flow field and on power generation. It concludes that surface roughness must be taken into account in power loss computation. Consequently, we have applied a

roughness level, computed during ice accretion analysis, in all the simulations. The second paper (Sagol, Reggio and Ilinca 2012), referred to in Chapter 4, presents the methodology of the CFD simulations and validates the power performance of the clean machine. In it, an appropriate turbulence model is selected by comparing the results obtained using various models with the experimental data. The third paper, referred to in Chapter 5, presents a comparison of icing computations on a wind turbine using two different methods, *Quasi-3D* and *Fully 3D*, with similar physical modeling. The purpose of this comparison is to determine whether or not the additional computer resources required for the simulations in the *Fully 3D* method are justified by the improvement in the accuracy of the results. The results reveal the differences in the ice shapes and performance losses with the same inputs to both these models. Even though the computational cost of applying the *Fully 3D* method is much higher, icing analyses in 2D may lack accuracy, because the ice shapes and associated power losses are overestimated if the 3D characteristics of rotational flow are not taken into account. The final paper, referred to in Chapter 6, covers the application of a roughness model to prove the findings in the review article in Chapter 3. In this study, turbine performance is computed taking into account roughness. Various parameters, like wind speed, roughness size, and roughness duration, are evaluated. Moreover, a pre assessment of the Annual Energy Loss study reveals how the persistent contamination may decrease the energy yield. In this final section, the methodology in its entirety is applied to a specific wind farm icing case.

8.2 Limitations of the proposed method

Prior to the ice accretion analysis, the accuracy of the CFD method for single-phase and multiphase analysis was tested by comparing the results with experimental data. Comparing the blade torque of the wind turbine with the experimental data revealed that the forces cannot be predicted accurately, particularly for stall and post stall speeds, even though the most appropriate two-equation turbulence model was used. Time-dependent simulations might provide an answer to this problem. However, the computational cost would increase exponentially, considering the large number of simulations required for icing analysis. Moreover, multiphase analysis in 3D cannot be validated owing to a lack of experimental data. Consequently, we only validated a 2D case against the experimental data.

One of the objectives of this study was to automate all the simulations (single-phase CFD, multiphase CFD, meshing, and ice accretion analysis) using a MATLAB code. Although this code has been written and executed, we encountered some problems related to surface generation (ice shape) in 3D and to the convergence of the multiphase simulations. To solve the 3D surface generation problem, we divided the blade into sections following the multiphase analysis. We then computed the collection efficiency using the results of the 3D multiphase analysis. The ice shapes on these sections were computed, and then merged to form a blade with an updated ice shape. To remedy the instability of the solution in the convergence problem, we used a very low relaxation factor for the variables, which increases the computational time even more.

8.3 **Future study**

The most promising step to further improve the proposed model would be to validate it for 3D collection efficiency and ice shape. Comparing the results with experimental data would help reveal unknown deficiencies in the code, and problems with it. Measuring collection efficiency for 3D structures is difficult, But ice shape can be easily measured in a refrigerated wind tunnel. In fact, these kinds of experiments have already been performed by researchers. However, since the objective of the measurements was only to observe the performance loss of the wind turbine, the corresponding ice shapes were not measured.

Moreover, an appropriate surface generation algorithm could reproduce the iced blade surface, and in fact such an algorithm is available in MATLAB. However, some numerical errors prevented this process from being automated, and manual intervention was needed to eliminate the deviations.

In this study, we only computed rime ice accretion. However, glaze icing is also very common in Canada. For this reason, a thermodynamic model, based on the Messinger equations, should be developed to apply the model to this form of ice accretion. The computational models for glaze icing are much more complicated than those for rime icing. First, significant effort and computational resources are required for 3D simulation. Also, it is important to validate the glaze icing results against experimental data, as water flows over the blade before freezing. Consequently, predicting the freezing point will be a challenge.

Besides improving the ice accretion code, a methodology could be developed for finding the mean icing conditions at a wind turbine site. Such a study would increase the evaluation accuracy of the Annual Energy Production losses. With more accurate meteorological input data, the results will obviously become more reliable.

The author had intended to contribute to solving some of the issues surrounding the effects of icing on wind turbines as part of this research. This is only one of the many issues that need to be addressed by the wind energy sector.

BIBLIOGRAPHY

Aliaga, C., Aube, M. S., Baruzzi, G., & Habashi, W. (2010). FENSAP-ICE Unsteady: Unified in-flight icing simualtion methodology for aircraft, rotorcraft and jet engines. *Journal of Aircraft , 48* (1), 119-126.

ANSYS. (2010). *ANSYS FLUENT 12.0 Theory Guide.*

Bak, C. (2008). Design and verification of airfoils resistant to surface contaminaiton and turbulence intensity. *26th AIAA Applied Aerodynamics Conference.*

Benjanirat, S., Sankar, L., & Xu, G. (2003). Evaluation of Turbulence Models for the Prediction of Wind Turbine Aerodynamics. *22nd ASME wind energy symposium*, (pp. 73-83).

Blade access cleaning system for wind turbines. (n.d.). Retrieved 2013 йил August from http://www.ismhelp.com/products/bladeaccess.php

Blade Cleaning Limpieza de Palas. (n.d.). Retrieved 2012 йил April from www.bladecleaning.com/

BladeSkyn. (n.d.). Retrieved 2012 йил April from /www.bladedynamics.com

BladeSmart. (n.d.). General description of Gurney flaps. Retrieved 2012 йил November from /http://smart-blade.com/products-services/gurney-flaps.html

Botta, G., Cavaliere, M., & Holttinten, H. (1998). Ice Accretion at Acqua Spruzza and Effects on Wind Turbine Operation and Loss of Energy Production. *Boreas IV.* Hetta, Finland.

Bourgault, Y., Habashi, W. G., Dompierre, J., & Baruzzi, G. S. (1999). A finite element method study of eulerian droplet imoingement models. *International Journal for Numerical Methods in Fluids* (29), 429-449.

Bragg, M. B., Broeren, A. P., & Blumenthal, L. A. (2005). Iced Airfoil Aerodynamics. *Progress in Aerospace Sciences , 41*, 323-362.

Buhl, M. (2005). *A new empirical relationship between thrust coefficient and induction factor for the turbulent windmill state.* Colorado: Natinal Renewable Energy Laboratory.

Busch, G. (2009). *Experimental study of full scale iced-airfoil aerodynamics performance using sub-scale simulations.* University of Illinois at Urbana-Champaign.

Canada Wind Energy Association Reports. (n.d.). Retrieved 2011 from www.canwea.ca

Carlsson, V. (2009). *Measuring routines of ice accretion for wind turbine applications.* MSc Thesis submitted to UMEA University.

Cebeci, T., & Bradshaw, P. (1977). *Momentum Transfer in Boundary Layers.* New York: Hemisphere Publishing Corporation.

Corten, G. P., & Veldkamp, H. (2001). Insects can halve wind-turbine power. *Nature* (412), p. 41.

Corten, G., & Veldkamp, H. (2001). Insects cause double stall. *European Wind Energy Conference.* Copenhagen.

Dalili, A., A., E., & Carriveau, R. (2009). A review of surface engineering issues critical to wind turbine performance. *Renewable and Sustainable Energy Reviews* , 428-438.

Dimitrova, M., Ibrahim, H., Fortin, G., Ilinca, A., & Perron, J. (2011). Software tool to predict the wind energy production losses due to icing. *IEEE Electrical Power and Energy*, (pp. 462-467).

Drage, M., & Hauge, G. (2008). Atmospheric Icing in a coastal mountains terrain. Measurement and numericla simulations, a case study. *Cold Regions Science and Technology* , 150-161.

Drage, M., & Molmann, T. (2005). *Atmospheric Icing and meteorological variables- Full scale experiment and testing of models.* The University Centre in Svalbard Longyerbyen, Norway.

Duque, E., Johnson, W., van Dam, J. P., Cortes, R., & Yee, K. (2000). Numerical Predictions of Wind Turbine Power and Aerosynamic Loads for the NREL Phase II Combined Experimental Rotor. *AIAA/ASME Wind Energy Symposium, AIAA 38th Aerospace Sciences Meeting.*

Durbin, P., Medic, G., Seo, J., Eaton, J., & Song, S. (2001). Rough wall modification of two layer k-epsilon. *ASME Journal of Fluids Engineering* .

Ferrer, E., & Munduate, X. (2009). CFD Predicitons of transition and distributed roughness over a wind turbine airfoil. *47th AIAA Aerospace Sciences Meeting.*

Fikke, S., Ronsten, G., Heimo, A., Kunz, S., Ostrozlik, M., Persson, P., et al. (2007). *COST 727: Atmospheric Icing on structures measurements and data collection on icing: State of the art.* Publication of MeteoSwiss.

Finstad, K. J., Lozowski, E. P., & Makkonen, L. (1988). On the median volume diameter approximation for droplet collision efficiency. *Journal of Atmospheric Sciences , 45* (24).

Fortin, G., Ilinca, A., Laforte, J., & Brandi, V. New roughness computation method and geometric accretion model for aircraft icing. *Journal of Aircraft , 41* (1), 119-127.

Fortin, G., Laforte, J., & Ilinca, A. Heat and mass transfer during ice accretion on aircraft wings with an improves roughness model. *International Journal of Thermal Sciences , 45* (6), 595-606.

Freudenreich, K., Kalser, K., Schaffarczyk, A. P., Winkler, H., & Stalh, B. (2007). Reynolds number abd roughness effect on thick airfoils for wind turbines. *Wind Engineering* , 529-546.

Fu, P., & Farzaneh, M. (2010). A CFD approach for modeling rime-ice accretion process on a horizontal axis wind turbine. *Journal of wind Engineering and Industrial Aerodynamics* , 181-188.

Fuglsang, B., Bak, C., Gaunaa, M., & Antoniou, M. (2004). Design and verification of the RISO-B1 airfoil family for wind turbines. *Journal of Solar Energy Engineering* , 1002-1010.

G., L. J. (2002). *Principles of Helicopter Aerodynamics (2rd ed.).* Cambridge University Press.

Gregory, N., & O'Reilly, L. (1973). *Low speed aerodynamics characteristics of NACA 0012 aerofoil section, including the effect of upper-surface roughness simulating hoar frost.* London, UK: Aeronautical Research Council.

Han, Y., Palacios, J., & Schmitz, S. (2012). Scaled ice accretion experiments on a rotating wind turbine blade. *Journal of Wind Engineering and Industrial Aerodynamics* , 55-67.

Hand, M. M., Simms, D., & Fingersh, L. (2001). *Unsteady aerodynamics experiment phase VI: wind tunnel test configurations and available data campaigns.* NREL.

Hansen, C. (n.d.). NWTC Computer aided engineering tools- AirfoilPREP . Retrieved 2013 йил January from http://wind.nrel.gov/designcodes/preprocessors/airfoilprep/

Hansen, M. O., Sorensen, J. N., Voutsinas, S., Sorensen, N., & Madsen, H. (2006). State of the art in wind turbine aerodynamics and aeroelasticity. *Progess in Aerospace Sciences* , 285-330.

Helimax Energie, I. *Étude sur l'évaluation du potentiel éolien, de son prix de revient et des retombées économiques pouvant en découler au Québec.*

Hochart, C., Fortin, G., Perron, J., & Ilinca, A. (2008). Wind turbine performance under icing condition. *Wind Energy* , 319-333.

Homola, M. C., Virk, M., Wallenius, P. J., Nicklassin, P., & Sundabo, P. A. (2010). Effect of atmospheric temperature and droplet size variation on ice accretion of wind turbine blades. *Journal of Wind Engineering and Industrial Aerodynamics* , 724-729.

Honsek, R., Habashi, G., & Aube, M. (2008). Eulerian Modeling of In-Flight icing due to supercooled large droplets. *Journal of aircraft* .

Illinca, A. (2011). Analysis and mitigation of icing effects on wind turbines. In I. Al-Bahadly, *Wind Turbines.* InTech.

Jasinski, W. J., Noe, S. C., Selig, M. S., & Bragg, M. B. (1997). Wind turbine performance under icing condition. *AIAA 35th Aerospace Sciences Meeting & Exhibit.* Reno, NV.

Johansen, J., & Sorensen, N. (2004). Aerofoil characteristics from 3D CFD rotor computations. *Wind Energy* , 283-294.

KellyAerospace. (n.d.). Wind turbine ice protection system. From /http://www.kellyaero

Kerho, M., & Bragg, M. (1997). Airfoil boundary-layer development and transition with large leading edge roughness. *AIAA Journal , 35* (1).

Khalfallah, M. G., & Kolub, A. (2007). Effect of dust on the performance of wind turbines. *Desalination* .

Knopp, T., Eisfeld, B., & Calvo, J. (2009). A new extension for k-w turbilence model to account for wall roughness. *International Journal of Heat and Fluid Flow* , 54-65.

Kraj, A. G., & Bibeau, E. L. (2009). Phases of icing on wind turbine blades characterized by ice accumulation. *Renewable Energy* , 966-972.

Lachmann, G. (1960). *Aspects of insect contamination in relation to laminar flow aircraft.* Aeronautical Research Center Technical Report.

Launder, B. E., & Spalding, D. B. (1972). *Lectures in Mathematical Models of Turbulence.* London, UK: Academic Press, London.

Laursen, J., Enevoldsen, P., & Hijort, S. (2007). 3D CFD Quantification of the Performance of a Multi-Megawatt Wind Turbine. *The Science of Making Torque from Wind, Journal of Physics Conference Series 75 .*

Lee, S., Kom, H., & Bragg, M. B. (2000). Investigation of factors that influence iced-airfoil aerodynamics. *38th Aerospace Sciences Meeting & Exhibition.* Reno, NV.

Leishman, J. G. (2002). *Principles of Helicopter Aerodynamics. (2nd ed.).* Cambridge University Press.

Li, D., Li, R., Yang, C., & Wang, X. (2010). Effects of roughness on aerodynamics performance of a wind turbine airfoil. *Power and Energy Engineering Conference (APPEEC).*

Makkonen, L., Laakso, T., Marjaniemi, M., & Finstad, K. J. (2001). Modeling ice accretion on wind turbines. *Wind Engineering* , 3-21.

Martini, F., Ramdenee, D., Ibrahim, H., & Ilinca, A. (2011). A Lagrangean interactive interface to evaluate ice accretion modeling on a cylinder- Test case for icing modeling on wind turbine airfoils. *IEEE Electrrical Powe and Energy*, (pp. 456-461).

Martini, F., Ramdenee, D., Ibrahim, H., & Ilinca, A. (2011). A Multiphase CFD Based Approach to Ice Accretion Modeling on a Cylinder. *IEEE Electrical Power and Energy*, (pp. 450-455).

Menter, R. F. (1994). Two-equation eddy-viscosity turbulence models for engineering applications. *AIAA Journal* , *32* (8), 1598-1605.

Myers, G. T. (2001). Extension the the Merssinger model for aircraft icing. *AIAA Journal , 39* (2).

N., S. J. (2011). Aerodynamics aspects of wind energy conversion. *Annual Review of Fluid Mechanics* , 427-448.

Ozgen, S., & Canibek, M. (2008). Ice accretion simulation on finite wings using extended Messinger model. *7th International Conference on Advances in Fluid Mechanics.*

Ozgen, S., & Canibek, M. (2009). Ice accretion simulation on multi-element airfoils using extended Messinger model. *Heat Mass Transfer* , 305-322.

Parent, O., & Ilinca, A. (2011). Anti-icing and de-icing techniques for wind turbines: critical review. *Cold REgions Science and Technology* , 88-96.

Patel, V., & Yoon, J. (1995). Application oof turbulence models to separated flow over rough surfaces. *Journal of Fluids Engineering , 117* (2), 234.

Pechlivanoglou, G. (2010). The effect of distributed roughness on the power performance of wind turbines. *ASME Turbi Expo*, (pp. 845-855).

Petrone, G., de Nicola, G., Quaglierella, D., Witteveen, J., & Iaccarino, G. (2011). Wind turbine performance analysis under uncertainity. *49th Aerospace Sciences Meeting including the New Horizons Forum and Aerospace Exposition.* Florida.

Ramdenee, D., Minea, S., & Ilinca, A. (2011). Simulation of Aerodynamic Divergence and Flutter on Wind Turbine usinf ANSYS-CFX. *CFD Society of Canada.*

Ramdenee, D., Minea, S., & Ilinca, A. (2011). Simulation of aerodynamic divergence and flutter on wind turbines using ANSYS-CFX. *IMAACA 2011.* Rome.

Ren, N., & Ou, J. (2009). Dust effect on the performance of wind turbine airfoils. *Jounal of Electromagnetic Analysis and Applications* , 102-107.

Ren, N., & Ou, J. (2009). Numerical simulation of surface roughness effect on wind turbine thick airfoils. *Asia-Pacific Power and Energy Engineering Conference (APPEEC).*

Rene, C., Markus, R., & Gabriela, R. (2009). Four years of monitoring a wind turbine under icing conditions. *IWAIS XIII.* Andermatt.

Rhinoceros. *Rhineceros NURBS modelling for Windows, version 4.0 User's Guide.*

Sagol, E., Reggio, M., & Ilinca, A. (2012). Assessment of two-equation turbulence models and validation of the performance characteristics of an experimental wind turbine by CFD. *ISRN Mechanical Engineering* .

Sagol, E., Reggio, M., & Ilinca, M. (n.d.). Comparison of Quasi-3D and Fully-3D methods for modeling wind turbine icing. *Renewable Energy* .

Sagol, E.; Reggio, M.; Ilinca, A. (2013). Issues concerning roughness on wind turbine blades. *Renewable and Sustainable Energy Reviews , 23*, 514-525.

Schlichting, H. (1979). *Boundary layer theory. 7th ed.* McGraw Hill Book Company.

Sezer Uzol, N., & Long, L. N. (2006). 3-D Time-Accurate CFD Simulations of Wind Turbine Rotor Flow Fields. *44th AIAA Aerospace Sciences Meeting and Exhibit.* Reno, Nevada.

Shen, W. Z., Mikkelsen, R., Sorensen, J. N., & Bak, C. (2005). Tip loss corrections for wind turbine computations. *Wind Energy* , 457-475.

Shih, T. H., Liou, W. W., Shabbir, A., Yang, Z., & Zhu, J. (1995). A new k-epsilon eddy viscosity model for high reynolds number turbulent flows. *Computer and fluids* , 227-238.

Silveria, R. A., Maliska, C. R., Estivam, D. A., & Mendes, R. (2003). Evaluation of Collection Efficiency Methods for Icing Analysis. *17th International Congress of Mechanical Engineering.* San Paolo, Brazil.

Simms, D., Schreck, S., Hand, M. M., & Fingersh, L. J. (NREL). *NREL Unsteady aerodynamcis experiment in the NASA Ames wind tunnel: a comparison of predictions to measurements.* 2001.

Smaili, A., & Masson, C. (2004). On the rotor effects upon nacelle anenometry for wind turbines. *Wind Engineering* , 695-714.

Sorensen, N. N.; Michelsen, J. A.; Schreck, S. (2002). Navier- Stokes Prediciton of the NREL Phase VI Rotor in the NASA AMES 90 ft x 120 ft Wind Tunnel ". *Wind Energy* , 5: 151-169.

Tangler, J., Smith, B., & Jager, D. (1992). *SERI advanced wind turbine blades.* National Renewable Energy Laboratory.

Timmer, W. (2009). An overview of NACA 6-digit airfoil series characteristics with reference to airfoils for large wind turbine baldes. *47th AIAA Aerospace Science meeting.* Orlando, FL.

Turner, A., Hubbe-Walker, S., & Bayley, F. (2000). Fluid flow and heat transfer over straight and curved rough surfaces. *International Journal of Heat and Mass Transfer* (43), 251-262.

van Rooij, R., & Timmer, W. (2003). Roughness sensitivity considerations for thick rotor blade airfoils. *ASME , 125*.

Vilalpando, F., Reggio, M., & Ilinca, A. (2012). Numerical Study of flow around iced wind turbine airfoil. *Engineering Applications of Computational Fluid MEchanics , 6* (1), 39-45.

Villalpando, F., Reggio, M., & Ilinca, A. (2011). Assessment of turbulence models for flow simulation around a wind turbine airfoil. *Modeling and Simulation in Engineering* .

Wabashi, W. G., Beaugendre, H., & Morency, F. (2003). Development of a second generation in-flight simulation code. *Proceedings of the ASME/JSME Joint Fluids Engineering Conference.*

Wang, X., Bibeau, E., & Naterer, F. (2007). Experimental investigation of energy losses due to icing of a wind turbine. *Challanges of Power Engineering and Environment* , 14:1143-1147.

Weiss, P. (n.d.). Insects in the wind lead to less power. Retrieved 2012 йил November from /http://www.sciencenews.org/view/generic/id/1854/description/Insects_in_the_wind_lead_to_less _power

Wilcox, D. (1994). *Turbulence Modeling for CFD.* California: DCW Industries, Le Canada.

Wirogo, S., & Srirambhatla, S. (2002). An Eulerian method to calculate the collection efficiency on two and three dimensional bodies. *41st Aerospace Sciences Meeting and Exhibit.* Reno, NV.

World Wind Energy Report. (n.d.). Retrieved 2010 from www.wwindea.org

Yakhot, V., & Orszag, A. (1986). Renormalization group analysis of turbulence. I-Basic theory. *Journal of Scientific Computing* , 3-51.

Zahle, F., & Sorensen, N. (2010). Characterization of the Unsteady FLow in the Nacelle Region of a Modern Wind Turbine. *Wind Energy* .

Zahle, F., Sorensen, N., & Johansen, J. (2009). Wind turbine rotor-tower interaction using an incompressible overset grid method. *Wind Energy* , 594-619.

APPENDICES

APPENDIX A –WIND FARM DATA

The wind farm we selected for our study is located in Blaiken, in northern Sweden. The icing events, the related atmospheric conditions, and the wind turbine power losses are presented in Table A. 3. As we have seen, an icing event for a wind turbine may last as long as 360 hours, depending on the location of the wind turbine site. Icing events are recorded with a camera mounted on the turbine, and the weather properties are measured with heated instruments.

The COST 727 project (Fikke, et al. 2007), which investigates atmospheric icing on structures, categorizes the severity of icing at a site as presented in Table A. 3.2 According to this classification, the Swedish wind site experiences heavy icing conditions, with 64 days of icing.

Table A. 3 Icing events of the sample wind farm in Blaiken, Sweden. (Carlsson, 2009)

Event #	Duration (hours)	Temperature (C°)	Relative Humidity (%)	Mean Pressure (Pa)	Power Loss (%)
1	25	-2,07	-	940,79	0,725051
3	3	1,13	80,25	957,13	0,666667
4	20	-1,82	100,8	958,9	0,113281
5	22	-2,88	-	960,28	0,353333
6	130	-1,88	85,17	951,73	0,826303
8	12	-3,03	100,66	961,77	0,287879
9	45	-1,84	-	950,82	0,231981
10	8	-3,74	-	949,11	0,173653
11	80	-2,65	91,06	949,97	0,204892
12	126	-6,15	111,69	949,15	0,691702
13	97	-1,21	-	937,36	0,793523
14	16	-1,36	-	919,84	0,747692
15	12	-0,79	-	917,6	0,51133
16	22	-1,57	101,94	917,88	0,477469
17	4	-2,87	-	933,1	0,073211
18	18	-5,59	91,04	928,51	0,142751
19	198	-2,6	101,26	954,76	0,575956
23	12	-13,77	106,14	941,41	0,025892
24	16	-11,04	111,17	944,5	0,020504
26	48	-13,16	107,47	938,23	0,18877
27	38	-17,78	102,74	938,17	0,223659
28	5	-16,08	103,71	929,39	0,37037
29	19	-13,83	102,7	938,79	0,36049
30	12	-14,31	102,47	953,26	0,183206
32	61	-11,02	101,59	959,33	0,622222
33	366	-12,43	101,65	951,4	0,533805
34	13	-14,89	102,47	936,21	0,115756
35	72	-11,12	101,59	953,29	0,334481
36	13	-11,42	101,92	944,36	0,231465
37	16	-11,91	101,47	950,52	0,384615

Table A. 4 Icing severity classification (Fikke, et al. 2007)

Site icing index	Days with meteorological icing /year	Typical intensity of icing (g/100 cm^{2}h)	Icing severity
S5	>60	>50	Heavy
S4	31-60	25	Strong
S3	11-30	10	Moderate
S2	3-10	5	Light
S1	0-2	0-5	Occasional

APPENDIX B –ICE GROWTH MATLAB CODE

```
clc; clear all;close all;


tic


%%%%%%%%%%%%%%%%%%%%%%%%%%%%%%%%%%%%%%%%%%%
%%%%%%%%%%%%%%%%%%%%%%%%%%%%%%%%%%%

%%%%%%2D/3D RIME ICE ACCRETION CODE%%%%%%%%%%%%%


%% MAIN MOD


M=6; % number of ice layers


TIME=300; % in seconds


TEXP=TIME/M;


for J=1:M;


%   [J]= SUB_VOF(J); % Automatic Gambit/Fluent iteration for 2D geos.


  [J]= SUB_ICE(J,TEXP);
```

```
end


function [I]=SUB_VOF(I)


%% GAMBIT AND FLUENT SEQUENCE


% Read initial geometry



%! C:\Fluent.Inc\ntbin\ntx86\gambit.exe -r2.4.6 -inp gambit_initial.txt


%Start FLUENT


! "C:\Program Files\ANSYS Inc\v130\fluent\ntbin\ntx86\fluent.exe" -r13.0.0  2ddp -wait -t4 -g -i
"C:\PHD\20JULY\fluent_initial.txt"


! "C:\Program Files\ANSYS Inc\v130\fluent\ntbin\ntx86\fluent.exe" -r13.0.0  2ddp -wait -t4 -g -i
"C:\PHD\20JULY\fluent_initial2.txt"


end


function [J]=SUB_ICE(J,TEXP)


%%%%%%%VARIABLES%%%%%%%%%%%%%%%
```

RHO_W=1000; %WATER DENSITY (KG/M3)

RHO_R=880; %RIME ICE DENSITY (KG/M3)

MVD=20e-6; % DROPLET MVD 20 micron

VINF=10; %FREESTREAM AIRSPEED (M/S)

VOF=1e-6; %VOF OF WATER

LWC=1; %LIQUID WATER CONTENT (G/M3)

%%%%%%%%READING 2D MESH %%%%%%%%%%%%%%%%%

%%%Reading 2D cell centered imported variables

% DC2= importdata('cent_2D);

%%% Reading 2D node centered imported variables

% DN2= importdata('node_up_1');

%%%

%Assigning 2D coordinates

%X2=DN2(:,4); %nodal x coordinate

%Y2=DN2(:,5); % nodal y coordinate

%XX2=DC2(:,2); % central x coordinate

%YY2=DC2(:,3); % central y coordinate

%%%Assigning other inputs;

%FTOT=DC2(:,4); % Total face area

%FX=DC2(:,5); % X Face Area

%FY=DC2(:,6); % Y Face Area

%V2X=DC2(:,7); % Vx speed for water phase

%V2Y=DC2(:,8); % Vy speed for water phase

%VOF2=DC2(:,9); % Volume Fraction of 2nd phase

%%%2-COMPUTING NORMALS OF THE MESH %%%%%%%%%%%%%%

%M=length(X); % number of points

%SLOPE=sparse(M,1);

%PSI=sparse(M,1);

%FTOT2=sparse(M,1);

%FXX=sparse(M,1);

%FX2=sparse(M,1);

%FY2=sparse(M,1);

% for I=2:M-1;

% SLOPE(I)=(Y(I)-Y(I-1))/(X(I)-X(I-1)) ;

%PSI(I)= atan((Y(I)-Y(I-1))/(X(I)-X(I-1)))+pi/2;

```
%end


%SLOPE(1)= (Y(1)-YY(1))/(X(1)-XX(1)) ;

%PSI(1)= atan((Y(1)-YY(1))/(X(I)-XX(1)))+pi/2;


%SLOPE(M)=(YY(M)-Y(M))/(XX(M)-X(M)) ;

%PSI(M)= atan((YY(M)-Y(M-1))/(XX(I)-X(M-1)))+pi/2;


%Validating the face area %VALIDATED

%for I=1:M-1;

   %FX2(I)=X(I)-X(I+1);

   %FY2(I)=Y(I)-Y(I+1);

   %FTOT2(I)=sqrt((X(I)-X(I+1))^2+(Y(I)-Y(I+1))^2);

%end


%for I=1:M;

  %  FXX(I)=FY(I)/FTOT(I);

%end


%FTOT2(M)=sqrt((X(M)-X(1))^2+(Y(M)-Y(I))^2);

%FX2(M)=X(M)-X(1);

%FY2(M)=Y(M)-Y(I);


%%%%%%%%READING 3D INPUTS %%%%%%%%%%%%%%%%
```

%%%%%%%%%%%%%%%%%%%%%%%%%%%%%%%%%%%%

%% Reading 3D cell centered imported variables

DC3= importdata('cent _3D');

%%% Reading 3D node centered imported variables

DN3= importdata('node_3');

%%%%Reading the connectivity of nodes and elements for blade surface

DCON3= importdata('conn_3');

%Assigning 3D coordinates

X3=DN3(:,4); %nodal x coordinate

Y3=DN3(:,5); % nodal y coordinate

Z3=DN3(:,6); % nodal y coordinate

XX3=DC3(:,2); % cell center x coordinate

YY3=DC3(:,3); % cell center y coordinate

ZZ3=DC3(:,4); % cell center z coordinate

%%%Assigning other inputs;

FTOT3=DC3(:,5); % Total face area

FX3=DC3(:,6); % X Face Area

FY3=DC3(:,7); % Y Face Area

FYZ=DC3(:,8); % Y Face Area

V2X3=DC3(:,9); % Vx speed for water phase

V2Y3=DC3(:,10); % Vy speed for water phase

V2Z3=DC3(:,11); % Vz speed for water phase

VOF3=DC3(:,12); % Volume Fraction of waterphase

%CON=DCON3(:,1); %Connectivity information

%%%3D-COMPUTING NORMALS OF THE MESH %%%%%%%%%%%%%%%

N=length(X); % number of cells

N2= length(X); % number of nodes

NORM=sparse(N,1);

NX3=sparse(N,1);

NY3=sparse(N,1);

NZ3=sparse(N,1);

 for I=1:N; %Compute surface normals

NX3(I)=FX3(I)/FTOT3;

NY3(I)=FY3(I)/FTOT3;

NZ3(I)=FZ3(I)/FTOT3;

%NORM(I)=NX3(I)+NY3(I)+NZ3(I) % Validate if unit normal vector is OK

end

%%%%%%%%COLLECTION EFFICINECY%%%%%%%%%%%%%

```
V_N=sparse(N,1);

BETA3=sparse(N,1);


for I=1:N;

BETA3(I)=  (NX3(I)*V2X3(I)+NY3(I)*V2Y3(I)+NZ3(I)*V2Z3(I))*VOF3(I)/VOF/VINF

if BETA3(I)<0;

   BETA3(I)=0;

end

end

%Plot Collection Eff for 2D.


% figure;

%plot(YY,BETA,'*');grid on

%title('Normalized normal velocity');

%xlabel('m');

%ylabel('m/s');

%fname=['BETA',num2str(J),'.fig'];

%hgsave(fname)

%%


%%%%%%%%%%%%%%ICE THICKNESS&VOLUME %%%%%%%%%


BICE_C=sparse(N,1);
```

```
BICE_N=sparse(N2,1);

NNX3=sparse(N2,1);

NNY3=sparse(N2,1);

NNZ3=sparse(N2,1);


M_W=sparse(N,1); %water flux on the cell

V_ICE=sparse(N,1); %volume of ice on the cell


%Ice growth on the cells

for I=1:N;

M_W(I)=BETA3(I)*VINF*LWC*FTOT3(I);

V_ICE(I)=M_W(I)*TEXP/RHO_R;

BICE_C(I)=M_W(I) *TEXP/RHO_R/FTOT3(I);

end


%Area weighted average ice growth on the nodes

%Nodal ice thickness

for I=1:N2;

function [I,CON_MAT,I2,CON_NUM]=SUB_CON(I,CON_MAT,I2,CON_NUM);

BICE_N(I)=0;

ATEMP=0;

for J=1:CON_NUM;

BICE_NTMP=BICE_C(I2)*FTOT2(I2);

ATEMP=ATEMP+FTOT2(I2);
```

```
BICE_N(I)=BICE_N+BICE_NTMP;

end

BICE_N(I)=BICE_N(I)/ATEMP;

end


% Compute normal direction of the nodes for growth direction

for I=1:N2;

function [I,CON_MAT,I2,CON_NUM]=SUB_CON(I,CON_MAT,I2,CON_NUM);

NNX3_T=0;

NNY3_T=0;

NNZ3_T=0;

ATEMP=0;

for J=1:CON_NUM;

NNX3_T=NX3(I2)*FTOT2(I2)+ NNX3_T;

NNY3_T=NY3(I2)*FTOT2(I2) + NNY3_T;

NNZ3_T=NZ3(I2)*FTOT2(I2) + NNZ3_T;

ATEMP=ATEMP+FTOT2(I2);

end

NNX3(I)=NNX3_T/ATEMP;

NNY3(I)=NNY3_T/ATEMP;

NNZ3(I)=NNZ3_T/ATEMP;

end


%%Compute new node coordinates
```

```
X3_N=sparse(N2,1);

Y3_N=sparse(N2,1);

Z3_N=sparse(N2,1);

for I=1:N2;

X3_N(I)=X3(I)+BICE_N(I)*NNX3(I);

Y3_N(I)=Y3(I)+BICE_N(I)*NNY3(I);

Z3_N(I)=Z3(I)+BICE_N(I)*NNZ3(I);

end

%%%%%%% WRITING NEW COORDINATES (RHINO)%%%%%%%%

 for I=1:N2;

   COOR_N(I,1)=X3_N(I);

   COOR_N(I,2)=Y3_N(I);

   COOR_N(I,3)= Z3_N(I);


end


dlmwrite('newcoord.dat', COOR_N,'delimiter','\t','precision',6);

end
```